University of Alberta

Towards a portable and inexpensive lab-on-a-chip device for point of care applications

by

Ayokunle Oluwafemi Olanrewaju

A thesis submitted to the Faculty of Graduate Studies and Research
in partial fulfillment of the requirements for the degree of

Master of Science

in

Biomedical Engineering

Department of Electrical and Computer Engineering

Fall 2011
Edmonton, Alberta

Examining Committee

Chris Backhouse, Professor, Electrical and Computer Engineering

Stacey (Bleoo) Hume, Assistant Professor, Medical Genetics

James McMullin, Professor, Electrical and Computer Engineering

To my parents

I owe more than I would try to express in words

Abstract

Ongoing work in the laboratory of Professor Chris Backhouse is aimed at developing a portable and inexpensive lab on a chip instrument. A system capable of molecular biology protocols including sample preparation (SP), polymerase chain reaction (PCR), and melting curve analysis (MCA) would meet the requirements for point of care genetic analysis. The SP, PCR, and MCA modules were designed and tested on a standalone basis and then integrated for analysis of raw clinical samples. An automated XY stage was developed for magnetic bead-based DNA purification. In addition, a LED/CCD-based optical detection module was employed for real time PCR and MCA. Data analysis algorithms and protocols were implemented to remove noise and interpret data. This work culminated in proof of principle on-chip SP-PCR-MCA to detect ß2m DNA from human buccal cells in a modular and inexpensive system.

Acknowledgements

First, I would like to thank my supervisor Professor Chris Backhouse for his patience and guidance throughout my time at the Applied Miniaturisation Lab. I have grown as a scientist and a thinker because you constantly challenged me to be rigorous in my work. I would also like to thank Professor James McMullin and Dr Stacey Hume for serving on my Master's committee. Your insights and questions pushed me to improve my work and contributed significantly to my growth as a researcher. I would also like to express my sincere gratitude to Alberta Ingenuity and the National Sciences and Engineering Research Council of Canada (NSERC) for their generous funding of my work.

Dr. Govind Kaigala, your guidance set me on the right path and your continued insight and advice helped keep me on that path. Dr. Moh Behnam, thank you for working with me, and sharing your knowledge and expertise. Allison Bidulock, your encouragement and attentive ear were essential to my success. Shane, thank you for not sending me packing when I destroyed the optocoupler for the umpteenth time. I will always be grateful for your patience and sublime electronics skills. Sheng, your Magic Johnson poster inspired me to be my best every day. Thank you for challenging me to show up to work early and to enjoy my time in grad school. To all of my colleagues at the AML – Eva, Jose, Karl, Matt, Samira, Saul, Sunny – your brains and smiles made life in the lab more enjoyable. I would also like to thank all of my professors and classmates in my courses and laboratory sessions at the University of Alberta. You've helped to make my academic experience more enjoyable and fruitful.

My friends and family have provided the love, support, and distractions that got me through grad school. Prem, thank you for not enabling my procrastination and for saving me from starvation. Steven, your brainstorming skills are unmatched even when you're illustrating on sandwich wrappers. Thank you for all the long conversations, the care you took to understand my questions, and for all your great suggestions. Iwasam, thank you for the long conversations and the video game marathons. To my brothers Michael, Ayobami, and Timilehin - even though you're far away, your unwavering encouragement and support reminded me to be my best. To my mom and dad, words cannot express all that you have done for me. This thesis is just one of the ways I can say thank you.

Table of Contents

List of Tables

List of Figures

List of Symbols

Abbreviation	**Definition**
ADC	Analog-to-Digital Converter
AML	Applied Miniaturization Laboratory
Angelina	Name given to the system I worked with at the AML
ß2m	ßeta-2-microglobulin
CCD	Charge-Coupled Device
DAC	Digital-to-Analog Converter
DSI	Deep Sky Smager
GUI	Graphical User Interface
LOD	Limit Of Detection
MCA	Melting Curve Analysis
PCR	Polymerase Chain Reaction
PWM	Pulse-Width Modulation
qPCR	real time quantitative PCR
SNR	Signal to Noise Ratio
SP	Sample Preparation
SPI	Serial Peripheral Interface
RIE	Reactive Ion Etch
Tm	Melting temperature
TTK	Tricorder Tool Kit
T_{chamber}	PCR chamber temperature
T_{heater}	Thin-film heater temperature
$T_{\text{heat sink}}$	Heat sink temperature
μTK	Microfluidic Tool Kit

CHAPTER 1

Introduction

Today, most medical diagnostic tests are performed by highly trained personnel in large centralized labs. Much of the equipment for these crucial endeavours is expensive and inaccessible in point of care settings. As a result, novel and important genetic testing is unavailable in point of care and low-resource settings, where the need for such technologies is greatest (Yager *et al.*, 2006). Lab-on-a-chip (LOC) technology employs some of the micro- and nano-fabrication processes that transformed modern electronics and computing from large, restricted rooms to portable, ubiquitous devices. LOC has the potential to provide such a dramatic shift in availability and applicability of medical devices for point-of-care testing (Whitesides, 2006).

Ongoing work in the laboratory of Professor Chris Backhouse, the Applied Miniaturisation Laboratory (AML), aims to bring this goal closer to fruition. Our laboratory already developed a portable instrument (Tricorder Toolkit, TTK) for the identification of the BK virus in human urine at a total cost of less than $1000 (Kaigala *et al.*, 2008). Our recent work is aimed at medical diagnosis with a low cost & inexpensive system starting with challenging biological samples such as saliva and blood.

1.1 Thesis outline

This thesis provides a chronological description of my contributions to ongoing research at the AML. The remainder of this chapter provides an introduction to core molecular biology processes such as the polymerase chain reaction (PCR), capillary electrophoresis (CE), and melting curve analysis (MCA). The goal of this chapter is to introduce the organization and main ideas in my thesis and to provide background information on theories discussed in future chapters.

In chapter 2, I describe the status of the lab-on-a-chip system (TTK) at the time I joined the AML as an undergraduate student. That design of the TTK represented the state of the art in portable and inexpensive LOC diagnostics (Kaigala *et al.*, 2008). I will provide a brief overview of its modular design and discuss past results to provide background information for my research.

Chapter 3 addresses the design and development of an automated X-Y stage for magnetic bead based DNA purification. This sample preparation (SP) stage was designed and built while I was an undergrad, but was tested during my MSc studies at the AML. I present initial results from standalone testing of the on-chip SP module with conventional PCR and CE instruments. We successfully purified beta-2-microglobulin (ß2m) DNA from human buccal cells. Furthermore, I highlight my training in the transfer of molecular biology protocols to microfluidic systems and the troubleshooting of experimental problems such as degraded SP reagents and contamination of negative controls.

In addition, chapter 4 discusses the reconfiguration of the TTK for real-time PCR. With real-time PCR, the TTK can amplify DNA while simultaneously monitoring reaction progress. In order to perform real-time PCR, we needed to modify both our thermal regulation and optical detection subsystems. In collaboration with M.Behnam, I engineered hardware, firmware, and software solutions to ensure sufficient optical sensitivity for real-time PCR on the TTK. Also, I contributed to initial testing of our thermal regulation subunit; however, that module was set aside for a thorough evaluation and re-design by other members of the AML[1]. I show the results of on-chip real-time PCR with ß2m genomic DNA and the application of our system to the detection of clinically relevant strains of malaria.

Chapter 5 focuses on post-PCR analysis with melting curve analysis (MCA). MCA allows us to identify PCR products based on their length and composition – this facilitates clinical applications such as distinguishing *P.falciparum*, the most fatal form of malaria, from less harmful strains such as *P.malariae*. MCA requires the same optical and thermal infrastructure as real-time PCR. However, we developed new temperature control and data analysis algorithms to generate melt curves and determine the melting temperature (T_m) of DNA samples. I also discuss the examination and resolution of problems we encountered while implementing MCA on-chip including: the presence of noise bumps in fluorescence data, and a temperature offset between T_m values obtained from the TTK and conventional MCA instruments.

After describing the SP, real-time PCR, and MCA subsystems individually, I address their integration in chapter 6. We purify, amplify, and analyze ß2m DNA from human buccal cells using the SP, real-time PCR, and MCA modules of the TTK. I analyze the results of this proof of principle demonstration and provide reasoned arguments for variations in PCR production strength and T_m value.

Finally, in chapter 7, I summarize the work detailed in this thesis. I briefly review the status of the system before I joined the AML, highlight my contributions to SP/real-time PCR/MCA design, and re-iterate initial results and problems encountered. This thesis

---

[1] This exercise was fondly dubbed the 'festival of calibrations' and I will summarize the findings in this thesis.

closes with a look at ideas for improving the system. Most of these proposed changes focus on optimizing the TTK's optical detection for real-time PCR and MCA to boost sensitivity. In addition, I suggest improvements to molecular biology protocols and propose additional experiments to reproduce and quantify proof of principle results obtained in this thesis.

1.2 Conventional genetic analysis

I will now introduce the core molecular biology processes required for point of care medical diagnosis. I will describe their mechanisms of operation and highlight existing commercial instruments that apply these technologies. Also, I will identify the main limitations of conventional diagnostic systems and introduce the need for lab on a chip solutions.

One of the dominant approaches to genetic analysis is nucleic acid testing (NAT). Nucleic acid testing permits identification of identify biomarkers or pathogens associated with point of care applications. For example, nucleic acid assays have been developed to detect and quantify the presence of the malaria parasite and the HIV virus – 2 endemic diseases in the developing world. Nucleic acid amplification is a crucial step required for such assays. Amplification ensures that there is a sufficient amount of analyte available for detection and analysis.

The Polymerase Chain Reaction (PCR) is the most commonly used method for DNA amplification both in conventional and microfluidic systems (Auroux *et al.*, 2004, Chen *et al.*, 2007a, Zhang *et al.*, 2006). The discovery and development of PCR as a viable molecular biology tool has greatly facilitated rapid nucleic acid assays for point of care applications.

1.2.1 PCR

During PCR, DNA samples of interest are amplified to increase the number of copies available for detection. PCR takes advantage of the complementary nature of double-stranded DNA molecules to amplify samples millions of times. PCR is a multistep process with 3 main processes: denaturation, annealing, and extension. During denaturation, a double-stranded DNA (ds-DNA) molecule is heated to high temperatures (up to ~95°C) to separate its 2 constituent strands. At this point, the reaction mixture is cooled to ~60°C for the annealing step. During annealing, artificially synthesized short (~20 bp) single-stranded DNA sequences (called primers) bind to the single-stranded DNA molecules. The primers are designed such that they mark the endpoints of the region of the DNA strand that will be amplified during the reaction. The final step in PCR is extension. Here, the temperature is raised to ~70°C to provide optimum conditions for the action of *Taq polymerase* enzyme to form new complementary strands for each of the single strands starting from the boundaries set by the primers.

At the end of this 3-step process, ideally 2 new double-stranded DNA molecules would have been generated from a single molecule. This process is usually repeated 20-45 times to synthesize sufficient genetic material for downstream analysis/detection (Auroux *et al.*, 2004, Kricka and Wilding, 2003, Kubista *et al.*, 2006). However, PCR amplification does not continue to double indefinitely. The number of molecules generated by an n-cycle PCR reaction is given by $(1+\epsilon)^{n}$, where ϵ is the PCR efficiency (i.e. the likelihood that 2 molecules will result from a single one) (Auroux *et al.*, 2004).

However, as primers and enzymes become used up, and competing PCR amplicons are formed – PCR reaction efficiency decreases – resulting in the plateau phase of PCR. Also, reaction efficiency (ϵ) is influenced by the quality of primer design. Prior to performing a PCR reaction, specific primers must be designed to bind to regions of interest within the target DNA sequence. If primer design is carried out properly, then only one region within the target genome is amplified; however, poor primer design can lead to a high likelihood for the formation of multiple PCR products, reducing overall reaction efficiency (Kubista *et al.*, 2006).

Other DNA amplification techniques

While PCR is the most popular DNA amplification technique, it is not the only nucleic acid based amplification technique available. Isothermal methods like Loop-mediated isothermal AMPlification (LAMP) (Auroux *et al.*, 2004) and Nucleic Acid Sequence-Based Amplification (NASBA) (Gulliksen *et al.*, 2004) are two techniques that are advantageous because they do not require thermal cycling. This simplifies the engineering requirements for conventional and microfluidic DNA amplification. Nevertheless, these methods often involve complex biological processes that necessitate the use of multiple primer sets and reaction reagents. These increased biological requirements often increase reaction complexity and limit the applicability of isothermal methods to a wide variety of point of care applications (Kubista *et al.*, 2006). Consequently, PCR is still the gold standard in use in conventional and microfluidic applications (Mackay, 2004, Zhang *et al.*, 2006).

1.2.2 Post-PCR analysis

Improper primer design or contamination can lead to the formation of unwanted PCR products. Consequently, Post-PCR analysis is required to verify the identity of amplicons generated.

Gel electrophoresis

Traditionally, PCR product analysis is carried out by size-based discrimination of PCR products. Gel electrophoresis is a traditional conventional method for DNA analysis. It involves loading a DNA sample into agarose gel in the presence of electrolytic buffers (which provide ions that facilitate migrate of negatively charged DNA molecules). Agarose (or another gel matrix) is used to provide a sponge-like environment that impedes DNA motion. Consequently, short and small DNA strands migrate through the gel matrix faster than long and large strands – this is the central mechanism behind gel electrophoresis. DNA molecules are compelled to move by the application of an electric field to attract the weak negative charge inherent in DNA molecules. Usually, hundreds of volts are applied across a short separation area (~10cm) to generate strong enough electric fields to move the DNA molecules through the gel.

To visualize DNA separation, the agarose gel is usually mixed with an intercalating dye (such as Ethidium bromide) which binds to double-stranded DNA molecules. When bound to DNA, fluorescence from the intercalator increases by orders of magnitude ranging from 2 to 1000 times depending on the choice of intercalator (Benesova-Minarikova *et al.*, 2005). Size standards ("DNA ladders") are run in adjacent gel lanes near the test sample. After each gel electrophoresis separation, images of the DNA molecules in the gel captured with a camera fitted with optical filters that capture only emission light from the intercalator. The resulting image usually shows DNA bands for the sample of interest, as well as bands for the DNA ladder. When the position of the sample DNA band is compared with that of the DNA ladder, the size of the DNA molecule can be identified – providing a useful metric to distinguish DNA molecules with known size differences and can have applications such as in the detection of single nucleotide polymorphisms (SNPs) which may be an important marker of genetic disorders (Sundberg *et al.*, 2007).

Capillary electrophoresis

Capillary electrophoresis (CE) is another size-based DNA separation mechanism. Just like gel electrophoresis, CE employs a gel sieving matrix and electrolytic buffers; however, a CE separation takes place in a narrow capillary (μm to mm scale) which produces the advantageous effect of improved sensitivity, resolution, and speed (Benesova-Minarikova *et al.*, 2005). During CE, narrow (μm-scale) capillaries are used – which offer size and sensitivity advantages – however, larger voltages need to be applied to generate sufficient electric field strength to move DNA through the capillaries.

Furthermore, CE also makes use of optical detection methods with intercalating dyes or end-labelled primers providing DNA fluorescence. During a typical CE run, the PCR product of interest is injected into a separation channel filled with sieving matrix. An electric field is applied across the separation channel – leading to migration of DNA samples through the gel sieving matrix. Small DNA molecules migrate faster than their large counterparts resulting in a size–based separation. This process is often visualized using optical detection (usually laser induced fluorescence). This involves positioning a laser light source near the end of the channel and tagging the DNA molecules with fluorophores from end–labelled primers or intercalators. DNA ladders are usually co-injected with the sample of interest for accurate determination of PCR product lengths.

1.2.3 Real time PCR

Why is real time PCR important?

Real time PCR involves monitoring the amount of DNA produced during the polymerase chain reaction. It is a variation on conventional PCR that can provide quantitative information about the starting amount of DNA in a reaction and permit the determination of reaction efficiency (Kubista *et al.*, 2006, Mackay, 2004). The starting concentration of DNA in a reaction is an important metric in many diagnostic tests. For example, real time PCR can be used to estimate the number of malaria parasites in a blood sample (Mangold *et al.*, 2005) – a crucial marker about the severity of the disease in a patient. Also, real time PCR has been employed in the identification and quantification of nucleic acids in food (Sandberg *et al.*, 2003).

General approaches to real time PCR

Real time monitoring of amplicon production is usually accomplished by fluorescence detection. There are 2 main paradigms for real time PCR detection: sequence specific probes or non-specific labels (Kubista *et al.*, 2006). Both approaches involve molecules that bind directly to the amplicon or its bounding regions, and result in fluorescence increases that are proportional to the amount of PCR products generated (Mackay, 2004).

Non-specific labels are based on traditional intercalating dyes used for DNA analysis (Mackay, 2004). Traditional nucleic acid stains like Ethidium Bromide influence the action of DNA polymerase during PCR; hence, they have been replaced with asymmetric cyanine dyes like SYBR green. Modern dyes like SYBR green show very little fluorescence when they are not bound to double-stranded DNA (dsDNA); however, as more dsDNA is produced the fluorescence from asymmetric cyanine dyes increases (Kubista *et al.*, 2006). This makes them very useful for quantification of on-chip real time PCR reactions. However, non-specific labels like SYBR green will fluorescence in the presence of any dsDNA including primer-dimers (Kubista *et al.*, 2006). As such, further analysis is required to check for the presence of unwanted amplicons like primer-dimers. This is usually accomplished by performing post-PCR melting curve analysis (described in section 1.2.4). Primer-dimers are usually distinguishable from target PCR products because primer-dimers often have smaller sizes and corresponding smaller melting temperatures.

On the other hand, specific probes bind to dsDNA based on their sequence information. Hydrolysis (commonly called Taqman) probes are designed to fluoresce strongly only when the target DNA molecule is bound. These molecules are designed so that the fluorophores are released during the DNA extension step when a complementary DNA strand binds (Kubista *et al.*, 2006, Mackay, 2004). Similarly, molecular beacons are labeled with fluorophores that increase their fluorescence when the target DNA molecule hybridizes. Also, care is taken to label the beacons with molecules (such as phosphates on the 3′ end) to prevent them from acting as primers (and competing with the target PCR product) (Mackay, 2004).

In their review, Kubista *et al.* (2006) state that for single DNA targets, dyes and probes are equally recommended since the performance of the assay still depends largely on primer design. Poor primer design can lead to primer-dimers which will adversely affect real time PCR reactions whether they are detected by specific probes or non-specific dyes. Primer-dimers will lead to higher than expected fluorescence when non-specific dyes are used, and to smaller than expected fluorescence with non-specific probes. In both cases, proper primer design is necessary to ensure optimal PCR efficiency.

Specific probes are advantageous because they can be used to distinguish one PCR product from the other. This is especially advantageous in multiplex PCR reactions (in which several amplicons are generated and detected simultaneously in the same reaction chamber) (Mackay, 2004). Meanwhile, dyes are beneficial despite their lack of specificity because they are cheaper than probes and can be used in almost all applications involving dsDNA (Kubista *et al.*, 2006).

The work described in this thesis makes use of a nonspecific dye (LCgreen plus) for real time PCR detection because of its low cost and applicability in generic applications – making it a good fit for use in the development of a lab on a chip platform for point of care applications.

Cycle threshold, Ct

The "cycle threshold", Ct, of a real-time PCR reaction is defined as the PCR cycle at which fluorescence rises above background levels. The Ct value is directly proportional to the starting DNA concentration – an important parameter in diagnostic tests (Wilhelm and Pingoud, 2003). A low numerical value for Ct indicates early onset of amplification above background levels. For two PCR reactions with the same efficiency, a lower Ct value corresponds with a larger starting amount of DNA and vice-versa. Calculation of Ct values depends on the signal to noise ratio of the platform as well as experimental settings (like brightness levels and choice of optical filters) that affect how much background light appears in each experiment. The Ct value is calculated by defining a noise threshold consisting of cycles where there is no clear fluorescence increase and consist mostly of background light levels (Mackay, 2004). There are several different mathematical algorithms for calculating Ct values (many of them proprietary), and these differences can also lead to variations in Ct values between instruments (Atrazhev *et al.*, 2010, Kubista *et al.*, 2006). As such comparing individual Ct values between instruments can be misleading. However, comparing Ct values obtained with the same instrument can provide a measure of the strength of PCR reactions and calibrating systems against well-characterized DNA standards allows accurate determination of starting DNA copy numbers and PCR efficiency (Gudnason *et al.*, 2007).

Absolute and relative quantification

After determining the Ct value of a real time PCR experiment, the starting concentration of DNA can be estimated. There are 2 main approaches to real time PCR quantification in the literature: absolute quantification using the standard curve method and relative quantification using the comparative Ct method (Schefe *et al.*, 2006). Absolute quantification involves measuring the Ct value from a serial dilution of template with known DNA concentration. This usually involves preparing one well-characterized standard and performing careful serial dilutions of the standard. Then real time PCR is performed on the various dilutions to generate a standard curve of Ct versus DNA concentration. Subsequent real-time PCR experiments with unknown DNA concentrations (but the same sample i.e. reaction efficiency) can then be compared with the calibration curve to determine the starting DNA copy number (Rutledge, 2004, Schefe *et al.*, 2006).

On the other hand, relative quantification does not require a calibration curve. Instead, PCR reactions are compared to a single standard or reference gene (Mackay, 2004). Relative quantification requires assumptions of ideal PCR efficiency (i.e. doubling of PCR product every cycle in the exponential growth phase). In addition, relative quantification also assumes that the PCR efficiency for the standard and the test sample are the same. With these assumptions, the starting concentration of the test sample can be calculated using the $2^{\Delta\Delta C_T}$ (comparative Ct) method (Kubista *et al.*, 2006, Schefe *et al.*, 2006). This algorithm calculates the difference in Ct values between the experiment and the standard, and uses that to estimate the starting DNA concentration. For example, a Ct difference of 1 unit implies that one sample has twice the starting DNA concentration of the other.

Although relative quantification is easier to perform, it is not as accurate as absolute quantification because it relies on the assumption that there is ideal efficiency which is often not the case (Schefe *et al.*, 2006). However, absolute quantification can also be error prone if the synthesis of the DNA standards is not accurate as any errors in the standards will skew the calibration curve and lead to quantification errors (Mackay, 2004).

1.2.4 Melting curve analysis

Although real-time PCR already provides quantitative analysis of DNA amplification, intercalating dyes cannot distinguish between different double stranded DNA molecules (Wilhelm and Pingoud, 2003). Consequently, we need additional techniques to differentiate between desired PCR products, primer-dimers, and other unwanted amplicons (e.g. contaminants). To address this concern, a variety of post-PCR DNA amplification techniques may be employed such as: gel electrophoresis, capillary electrophoresis, DNA microarrays, electrochemical detection, and melting curve analysis (Chen *et al.*, 2007a).

We chose melting curve analysis (MCA) as our post-PCR analysis technique because it offers unique advantages for integration within a microfluidic real-time PCR system. During MCA, a PCR product is slowly heated through its melting temperature (Tm) while the fluorescence from intercalating/fluorescent dyes is measured. The resulting fluorescence profile depends on its physical and chemical properties (Sundberg *et al.*, 2007) of the DNA molecule of interest. MCA is an indirect assay that can be used to distinguish between closely related species of DNA. It is an indirect assay because it needs to be compared with a direct assay (such as DNA sequencing or electrophoretic separation with size standards) in order to make an absolute determination of the identity of DNA molecules.

During melting curve analysis, a PCR product is slowly heated through its melting point while fluorescence is monitored. As the PCR product is heated through its melting point, the intercalators fall off because there are only single-stranded DNA molecules in solution

(Kubista *et al.*, 2006). At this point, there is a sharp drop in fluorescence at the melting temperature of the DNA strand (Herrmann *et al.*, 2006). The melting temperature (Tm) of the sample is defined as the temperature at which the negative first derivative of fluorescence against temperature (-dF/dT) is at its maximum (Cho *et al.*, 2006, Wilhelm and Pingoud, 2003). Because the melting temperature of DNA depends on its physical and chemical properties (e.g. length and base sequence) (Herrmann *et al.*, 2006), MCA can be used for a variety of clinical applications such as the detection of Hepatitis B & C viruses (Wang *et al.*, 2009) or the identification of gluten contamination in cereal (Sandberg *et al.*, 2003). By comparing the melting temperatures of DNA samples, it is possible to make inferences about the identity of PCR products (de Monbrison *et al.*, 2003, Herrmann *et al.*, 2006). In addition, MCA can be combined with other techniques (such as DNA sequencing or capillary electrophoresis in the presence of size-standards) to establish metrics for absolute identification of samples.

Furthermore, MCA is seamlessly and inexpensively integrated with real-time PCR (Lee *et al.*, 2010). Because melting curve analysis makes use of the same infrastructure (heater, optical detection) and reagents (DNA sample, intercalator) as real-time PCR, amplification and analysis can be completed sequentially in the same closed chamber with minimal human intervention. It is much more challenging and expensive to integrate and automate other post-PCR analysis techniques (e.g. capillary electrophoresis or gel electrophoresis) with real-time PCR without increasing the complexity, human intervention, and the risk of contamination (Espy *et al.*, 2006).

1.2.5 Commercial genetic analysis systems

The are several commercially available machines that combine real-time PCR and MCA. These automated machines are closed systems that combine thermal cycling and real-time detection. Table 1.1 summarizes state of the art conventional real-time PCR machines.

For PCR, conventional machines traditionally employ Peltier heating. This involves placing plastic (polypropylene) tubes filled with PCR cocktail in contact with a large metal heating plate. Large sample and reagent volumes (>25 μL) are usually required. Because of the large thermal mass of the heating plate, conventional PCR systems usually demand high power consumption and have slow heating and cooling rates. More recently, alternate heating architectures have been developed for conventional systems. For example, the Lightcycler® makes use of hot air heating. Glass capillaries are filled with PCR mix and placed in carousels inside the heating chamber. Subsequently hot air is circulated in the PCR chamber to provide rapid and uniform heating for the reaction. This approach provides speed and efficiency improvements but still relies heavily on manual handling and human intervention.

Most conventional real-time PCR machines employ optical detection systems. As summarized in 1.1, LED illumination and photodiode/CCD camera detection represent state of the art sensing systems in use today. This results in signal to noise ratio (SNR) of magnitude 10-100 – this represents sufficient sensitivity for many clinical applications (Espy *et al.*, 2006). In addition, conventional real-time PCR machines often have multiplexing capabilities that permit simultaneous amplification and analysis of as many as 384 samples at once on the ABI Prism 7900ht system. However, while multiplexing increases device throughput, it also raises system size and cost per test and limits the use of such systems to large centralized labs (instead of point of care and low-resource settings where the need for genetic analysis toolkits is also high).

Table 1.1: Examples of commercially available automated real-time PCR-MCA machines (Espy *et al.*, 2006, Lee *et al.*, 2010)

Instrument	Detection	SNR	Volume (μL)
LightCycler 2.0[a]	LED & photodiode	50	10-100
iCycler iQ[b]	LED & photodiode	32	50
Rotor-Gene 3000[c]	LED & PMT	60	10-150
Prism 7900ht[d]	Laser & CCD	53	5-50

---

[a] Roche Applied Science, www.roche-applied-science.com/lightcycler-online.

[b] Bio Rad, www3.bio-rad.com.

[c] Qiagen, www.qiagen.com.

[d] Applied Biosystems, www.appliedbiosystems.com.

1.3 Lab on a chip solutions

Miniaturized real-time PCR systems based on lab-on-a-chip (LOC) technology have the potential to eliminate many of the obstacles that prevent the use of genetic analysis systems in point of care settings. First, miniaturization involves working with PCR reaction chambers with small sample volumes (< 1 μL) and in many cases microfabricated heating systems. These scaling factors drastically reduce the thermal mass and involve the use of materials with high thermal conductivity such as silicon and glass. The net effect of PCR miniaturization is an improvement in heating and cooling rates and a significant reduction in PCR reaction time from hours to minutes (Cho *et al.*, 2006). Shorter reaction times are advantages because they reduce the time between sample collection and analysis – and create the potential for rapid diagnostic tests in the doctor's office or a patient's home. In addition, shorter PCR reactions leave less room for the formation of unwanted amplicons.

Another benefit offered by LOC devices is reduced sample and reagent volumes. Successful on-chip PCR has been demonstrated with sample volumes as small as 86 pL (Sundberg *et al.*, 2007) – with nL sample volumes being most common in the literature. The use of small volumes reduces the reaction cost per test and also contributes to fast reaction times. In addition, LOC systems have the capability for integrated functionality. Because of their small size multiple reaction and sample handling steps, such as: sample preparation, fluid manipulation, PCR, optical detection, and analysis, can be integrated onto the same device without significant cost or size restrictions. This automation and integration reduces the need for a trained operator and improves quality control by lowering the risk of cross contamination.

1.4 Closing remarks

The advantages of LOC systems are compelling and have propelled efforts to develop portable and inexpensive genetic analysis toolkits for point of care applications (Whitesides, 2006, Yager *et al.*, 2006). Brennan *et al.* (2009) state that the requirements for a true point of care LOC system would include: low capital cost (<\$2000), small cost per test (<\$10), fast completion time (< 1hour), and minimal need for a trained operator. While there have been demonstrations of LOC systems, with comparable sensitivity to commercial real time PCR machines (Lien *et al.*, 2009, Novak *et al.*, 2007), many of these publications still rely heavily on expensive infrastructure such as mercury lamps and fluorescence microscopes for optical detection (Chen *et al.*, 2007a). More work is required for an inexpensive "sample-to-answer" system (Chen *et al.*, 2007a, Kim *et al.*, 2009).

Two of the main challenges that need to be addressed in this endeavour are the development of an automated and efficient sample preparation system as well as the integration of sample preparation, amplification, and analysis in a portable and inexpensive platform (Brennan *et al.*, 2009, Chen *et al.*, 2007a, Kim *et al.*, 2009). On-chip sample preparation will be discussed in detail in chapter 3, while the integration of SP, PCR, and MCA modules will be covered in chapter 6.

The goal of ongoing work at the AML is to develop a portable and inexpensive lab on a chip toolkit for point of care applications. This thesis discusses the development of an automated sample preparation module and its integration with downstream DNA amplification and analysis. In the following chapter, I describe the status of the lab-on-a-chip system in development at the AML when I joined the team as an undergraduate student. I will provide an overview of its design and features for portable and inexpensive medical diagnosis.

CHAPTER 2

Initial system design

Ongoing work in the laboratory of Prof. Chris Backhouse (ECE, U of A) is aimed at building portable and inexpensive medical diagnostic devices using lab-on-a-chip (LOC) technologies. Our laboratory earlier developed a shoebox-sized system (tricorder toolkit, TTK) capable of amplifying and analyzing purified clinical samples using a custom-built instrument with a total component cost under $1000. This system represented the state of the art in low-cost LOC diagnostics and was published in leading journals in the field, and was featured as the cover article in the *Analyst* (Kaigala *et al.*, 2008).

In this chapter, I will describe the design of the TTK at the time I joined the AML. I will provide an overview of the TTK's modular architecture, microchip design, and initial results. The objective of this chapter is to provide background information to explain design decisions and trade-offs made during my MSc research.

2.1 TTK subsystems

The TTK platform was designed to be a modular and inexpensive system for portable point of care testing. This modular architecture is advantageous because it allows operation with a platform-independent graphical user interface (GUI) on an external laptop computer. In addition, modularity sandboxes the system's hardware, firmware, and software resulting in stable performance and easy upgrades of individual modules.

All the required electronics are implemented on printed circuit boards (PCBs) and perform one specific function each. The PCB for each module is connected to the system's microcontroller via a SPI interface. The system's subunits are described in detail in our past work (Kaigala *et al.*, 2008), but I will provide a brief overview here for completeness.

1. **Micro-controller (MCU)**: the brains of the operation. With its embedded firmware (written in the C++), the MCU automates all the processes carried out by the TTK.
2. **Firmware**: a program in C++ that directs protocols on the MCU. It coordinates data collection from the GUI (written in Python), performs the required physical processes (e.g. temperature control, optical detection, and valve actuation) in an automated and time-sensitive manner.
3. **Software**: the front end that allows user interaction with TTK. It is a graphical user interface (GUI), written in Python, and is run on an external laptop computer. The software analyzes data generated by the firmware and automatically creates run reports for each experiment.
4. **System Measurement Unit (SMU)**: this consists of electronic components used to measure and regulate the TTK's heater infrastructure. This module is essential for regulating the current supplied to the Pt thin film heating element in the microchip – and is crucial for accurate temperature sensing and control during on-chip PCR.
5. **Temperature measurement**: thermocouples and electronic components required for accurate and automated room temperature determination. Data from the temperature module is passed to the MCU firmware and is used to correct for room temperature fluctuations during PCR reactions.
6. **Valves/pumps**: this module is made up of an electronics board and mini-pumps that are used to actuate microfabricated 'Mathies style' valves for fluid flow through the TTK (e.g. pumping samples in and out of the PCR reaction chamber)
7. **Optics**: 5 mW red laser and CCD camera for optical illumination and detection. Optical filters and lenses are employed to monitor emission light from samples of interest and to boost device sensitivity.
8. **Power**: required infrastructure for power supply to the TTK. This subsystem consists of relays and optical switches, and takes power from a wall adapter unit down to 5V for the microcontroller and 12V for the valve and SMU boards.
9. **High voltage**: this module is made up of DC-DC adapters and high voltage relays connected to metal electrodes. These are used to provide the strong electric fields needed for on-chip capillary electrophoresis. During CE, the current is measured with a trans-impedance amplifier.

2.2 Microfluidic chip

This section provides a brief description of the tri-layer microfluidic chip used in our TTK devices. The chip (shown in figure 2.1) consists of two layers (top and bottom) of 1.1 mm Borofloat glass (Schott AG, Germany) and a 254 μm thick Polydimethylsiloxane (PDMS) membrane between them. This arrangement permits actuation of on-chip peristaltic "Mathies style" microvalves using mini-pumps integrated with the TTK. The 90μm deep PCR reaction chamber is located on the top glass layer and has a total volume of 600 nL. The design incorporates a valveless sample preparation channel for DNA purification, and capillary electrophoresis channels and wells for post-PCR analysis.

2.2.1 Microfabrication protocol

Microchip fabrication is the same as in our past work (Kaigala *et al.*, 2008) but is summarized here for completeness. Chip designs were completed in L-Edit v3.0 (MEMS Pro 8, MEMS CAP,CA, USA) and transferred to a photolithography mask using a pattern generator (DWL 200, Heidelberg Instruments, CA, USA). The 4" x 4" glass substrate was first cleaned in hot Piranha (3:1 of H_2SO_4:H_2O_2) cleaning and then coated with 30nm of Cr and 180nm of Au by sputtering. Next, HPR 504 photoresist (Fujifilm USA Inc., NY, USA) was spun onto the glass substrate at a spin speed of 500 rpm for 10 s and a spread speed of 4000 rpm for 40 s. The photoresist-coated substrate was then baked in an oven at 115°C for 30 min. The next lithography steps were followed by UV exposure (4 s, 356 nm and with an intensity of 19.2 mW/cm) of the spin- coated substrate through the chrome mask using a mask aligner (ABM Inc., San Jose, CA, USA) and chemical developing of the photoresist using Microposit 354 developer (Shipley Company Inc. ,Marlborough, MA, USA) for $\sim$ 25 s. The glass substrate was etched using hydrofluoric acid [20:14:66 HF(49%): HNO_3(70%): H_2O], this etch process has the etch rate of $\sim$1.1 μm/min. The bottom glass layer (control layer) was etched to a 70 μm depth, and the top glass layer (fluidic layer which includes SP channel, and PCR chamber) was etched to 90 μm. Finally to glass etching, the masking metals, Cr and Au, were stripped using Au etch (0.0985M I_2+0.6024 M KI) and Cr etch (Arch Chemicals Inc., Norwalk, CT, USA).

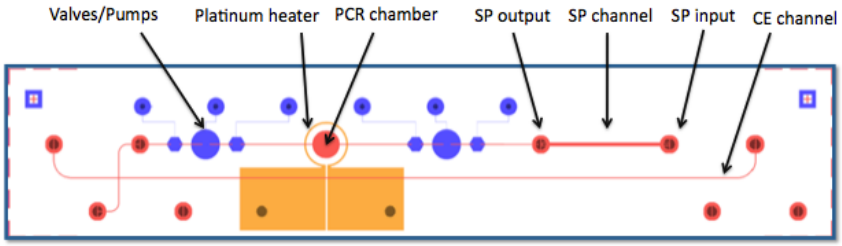

Figure 2.1: Tri-layer microfluidic chip for SP, PCR, and MCA. The chip is made up of 2 Borofloat glass layers and an intermediate PDMS layer for micro-valve actuation. Features in red are on the bottom face of top glass layer ("fluidic layer") where fluid and magnetic bead movement is performed while features in blue are on the upper face of the bottom glass layer ("control layer") where valve actuation is controlled. The platinum heating/sensing element is etched onto the control layer of the microchip

To access both fluidic and control channels, portholes were drilled using a Water-jet system (Bengal, Flow International Corp., Kent, WA, USA). To fabricate the micro-heater/sensor, a Pt film was patterned on the bottom glass layer using "lift-off" technique. After cleaning the bottom glass layer with hot piranha, 20 nm of Cr was sputter-deposited. Subsequently, AZ 4620 photoresist (AZ Electronic Materials Corp, Branchburg, NJ, USA) was spin coated for 10 s at a spread speed of 500 rpm and spin speed of 2000 rpm for 25 s, the substrate was then soft-baked on a hot-plate for 90 s, and then hydrated for 2 h. The photoresist was then UV exposed for 30 s using a mask aligner through a mask and developed using AZ 400 K (AZ Electronic Materials USA Corp., Branchburg, NJ, USA) developer for ~120 s, after which the Cr was etched. A 20 nm thick layer of Ti and a 220 nm thick layer of Pt were sputter deposited. The micro heater element was then defined using lift-off step. The glass was annealed at 200°C for 2 hours to ensure an even surface and repeatable micro-heater element structure. To ensure better biocompatibility (for on-chip experiments such as PCR and MCA) custom PDMS membranes were fabricated in-house. The PDMS monomer (Sylgard 184, Dow Corning) was mixed with curing agent in a 10:1 weight ratio. The resulting mixture was then poured on top of the Cr/Au substrate, and spread at 100 rpm for 15 seconds followed by a spin at 140 rpm for 300 seconds – these settings were chosen to obtain a final (after baking) PDMS membrane thickness of 254 μm (with an estimated ~10% variation). Afterwards, the substrate was baked at 80°C for 2 hours. Finally, the PDMS membrane was irreversibly bonded to the top and bottom glass layers using an oxygen plasma activated process that was performed in a reactive ion etching chamber (MicroEtch RIE). The bottom glass layer and the PDMS membrane were first exposed to oxygen plasma for 30 s (25% O_2 flow, 500 mTorr, 40 W (13.3%) RF power). The PDMS membrane was then laid on the bottom glass layer with extra care was taken to avoid the formation of air pockets that result in ripples and poor bonding between the glass and PDMS layers. The PDMS-glass structure was then left untouched for 8 hours to increase bonding strength. Subsequently, the top glass layer was bonded to PDMS-glass structure following the same protocol.

2.2.2 Microchip calibration

As described in section 2.2, we designed a microchip with a sputter-deposited Pt heating/sensing element. As a result, it is necessary to thermally calibrate the heating element within each chip to determine its resistive properties (e.g. thermal coefficient of resistance, TCR) (Cho *et al.*, 2006). These values are then used to determine optimal conditions for electric heating of each individual chip. The procedures and rationale behind our thermal calibration techniques are described in our past work (Hoang, 2008, Kaigala, 2009); however, I will summarize the general approach here and the changes made to ensure accurate and repeatable temperature control.

To determine the resistive properties of each microchip, we apply electrical heating to its resistive elements by supplying current to the heating elements with a source measurement unit (Keithley model 236, Cleveland, OH, USA) and vary the temperatures by immersing the microchip in a commercial water bath (HAAKE Phoenix II PI circulator, Thermo Electron Corp., Waltham, MA, USA). This provides sufficient data for a temperature vs resistance plot from which we obtain TCR and R_0 values. The relationship between resistivity, TCR, and temperature of a metal heating element is given by:

$$\rho = \rho_0(1 + \alpha(T - T_0)) \tag{2.1}$$

where ρ is the resistivity, ρ_0 is the resistivity at a reference temperature T_0, and α is the TCR. The TTK firmware accepts TCR and ρ_0 values and uses these to calculate the resistance (and by extension) temperature of the Pt heating elements as different electrical currents are supplied to the microchip. We make use of a PI controller for rapid and accurate temperature regulation in order to reach the temperature set points for real time PCR and MCA. The design, modelling, and testing of the PI controller is beyond the scope of this thesis and is discussed in detail by Kaigala (2009) and Hoang (2008).

2.3 Initial results from TTK

Using this initial design of the TTK, we were able to perform clinically relevant on-chip PCR-CE tests with purified DNA samples. We performed successful on-chip amplification and detection of the ß2-microglobulin (ß2m) gene – a housekeeping gene in human cells. Our portable and inexpensive instrument gave comparable performance to a commercial microchip system for CE analysis (μTk, Micralyne Inc., Edmonton, AB) (Kaigala *et al.*, 2008). We also applied our shoebox-sized PCR-CE instrument to the detection of BK virus in unprocessed urine samples.

2.4 Closing remarks

Although the system described in this chapter represented the state of the art in portable and inexpensive medical diagnostics at the time it was made, it was not yet ready for true clinical use. Sample preparation remains one of the bottlenecks prevent widespread adoption of lab on a chip systems for medical diagnosis (Whitesides, 2006). To tackle this fundamental problem, we developed an automated sample preparation (SP) module to purify nucleic acids from untreated clinical samples (such as blood or saliva). The next chapter discusses the design and development of this SP module.

CHAPTER 3

Sample preparation

As discussed in chapter 2, the TTK is a state of the art portable and inexpensive instrument for medical diagnosis. However, at the time I joined the AML it did not yet include a sample pre-treatment module. As such, the TTK could not be used with raw clinical samples – limiting its use in point of care settings.

Sample preparation is a major bottleneck in the adoption of LOC systems in point-of-care applications (Whitesides, 2006, Yager *et al.*, 2006). Most lab on a chip systems still rely on trained operators and conventional laboratory equipment in order to purify raw clinical samples. This makes for more of a "chip-in-a-lab" technology rather than a true lab-on-a-chip solution.

In this chapter, I will briefly review approaches to conventional and on-chip DNA purification in the literature. Then I will describe the design and development of a magnetic bead-based SP module in the AML[1]. I will discuss design requirements, provide detailed information on system and protocol development, and show results from standalone testing of the SP subsystem.

3.1 Conventional DNA purification

Today, when a clinical sample is sent to a medical laboratory for nucleic acid testing, a healthcare professional first purifies DNA from the raw sample. This step is necessary to remove inhibitors such as heparin, heme, and lipids from raw clinical samples and to facilitate downstream amplification by PCR (Espy *et al.*, 2006, Kubista *et al.*, 2006).

---

[1] I designed the SP subsystem during my undergraduate final year project and then integrated it with the TTK during my MSc studies.

3.1.1 Traditional liquid phase extraction

There a variety of well characterized techniques for nucleic acid extraction in conventional laboratories. Liquid phase methods were very common shortly after the discovery of the structure of DNA. The central principle behind these methods was to separate clinical samples into ionic and non-ionic layers by mixing them with appropriate reagents and centrifuging. State of the art methods for liquid phase DNA extraction include: phenol-chloroform extraction, caesium chloride gradient extraction, and chelex assays (Chomczynski and Sacchi, 2006, Ivanova *et al.*, 2006).

Caesium Chloride gradient extraction

Caesium chloride gradient extraction is a well-established technique that involves centrifuging raw samples in a caesium chloride – ethidium bromide (CsCl/EtBr) gradient. Ultra-high centrifuging creates a density difference between CsCl and water. This allows segregation of nucleic acids according to their molecular weight. This method is inexpensive and purifies large amounts of high quality DNA for a wide range of applications. However, problems with problems with CsCl gradient extraction include: need for an ultracentrifuge, long spin required (up to 48 hours), and EtBr (a required reagent) is mutagenic (Price *et al.*, 2009).

Phenol-chloroform extraction

Phenol-chloroform extraction is a dominant method of traditional DNA extraction (Ivanova *et al.*, 2006). It involves mixing phenol and chloroform in the presence of chaotropic salts (Chomczynski and Sacchi, 2006). The procedure for phenol-chloroform extraction involves mixing a 50:50 solution of phenol-chloroform with an aqueous sample containing nucleic acids. Then the mixture is centrifuged. Phenol-chloroform denatures proteins and leaves DNA in the upper aqueous solution while denatured proteins settle to the heavier organic layer. This is a very simple & high yield nucleic acid extraction method. However, it requires complex fluid handling and large and expensive equipment (centrifuge). Also, phenol is highly corrosive, as such it is dangerous to work with (Ivanova *et al.*, 2006). Also, contaminating organics left behind in the aqueous solution may inhibit many downstream processes such as PCR.

Chelex assays

Chelex assays are another dominant nucleic acid extraction method in conventional laboratories (Walsh *et al.*, 1991). Chelex involves mixing samples with a chelating agent and heating the resulting suspension to boiling. This results in cellular breakdown and protein denaturation leading to the release of DNA into the suspension. Chelex binds to multivalent ions and allows the extraction of free-floating DNA in the solution. Centrifuging the mixture leaves the DNA in the supernatant, allowing convenient separation of DNA from unwanted cellular components. This is an inexpensive method for DNA extraction; however, samples obtained with Chelex are of poor quality (Ivanova *et al.*, 2006). In addition, it is a process that requires a centrifuge and multiple fluid-handling steps, consequently, it is not easily ported onto a microfluidic platform. Furthermore, Chelex only extracts single-stranded DNA molecules limiting its usefulness for downstream reactions such as PCR.

3.1.2 Solid phase extraction

To overcome the problems of contamination, handling, speed, & cost often associated with liquid phase extraction techniques, researchers moved towards solid-phase extraction (SPE) methods that do not require centrifuging and toxic reagents. The "Boom method" was a major advance that used diatomaceous earth (mostly silica) to purify DNA from clinically relevant samples quickly (in less than 1 hour) and with high yield (Boom *et al.*, 1999). Today, SPE is often used in conventional laboratories with materials such as silica, glass fibre, & diatomaceous earth that preferentially bind to DNA when mixed with chaotropic salt solutions. SPE is efficient and usually does not require centrifuging to separate DNA from a solution – this reduces the instrumentation required to implement sample preparation (Price *et al.*, 2009).

There are commercial SPE kits available in different configurations such as filters, columns, & beads. More recently, innovations in automation have triggered the development of magnetic particles/beads with DNA affinity to eliminate the need for simplify the process of separation solid phase elements from the reaction mixture. Such beads bind to DNA because of specific labels that provide DNA affinity such as chemical coatings, antibody treatments, or electrostatic interactions (Chen *et al.*, 2007a, deMello and Beard, 2003, Price *et al.*, 2009). The magnetic nature of these beads allows sample manipulation by the application of an external magnetic field rather than pumping fluid solutions. As a result, bead-based SPE methods can be automated with motion control systems attached to permanent magnets (or with the use of electromagnets that can be turned on or off). Another benefit of bead-based SPE is the potential for sample pre-concentration. Analytes can be extracted from large, dilute sample volumes using beads which are later transferred into smaller volumes to generate concentrated stock solutions. Pre-concentration can greatly boost the sensitivity of genetic analysis systems (deMello and Beard, 2003, Lichtenberg *et al.*, 2002)

SPE requires less complex instrumentation and offers higher yield and pre-concentration capabilities when compared with liquid phase techniques. However, many silica-based SPE methods still require the use of chaotropic salt solutions that are incompatible with downstream PCR amplification (Price *et al.*, 2009). In addition, SPE methods still require considerable automation and numerous wash steps that increase the difficulty of implementation on LOC devices.

3.2 State of the art on-chip SP

In this section, I will provide a summary of state of the art approaches to on-chip SP. As described in the earlier sections, the extraction of DNA from raw clinical samples requires lysing the cells or tissues to gain access to nucleic acids followed by either traditional liquid phase or newer (and more efficient) solid phase methods to selectively bind to DNA and leave behind unwanted cellular material that may hinder analysis and amplification reactions (Kim *et al.*, 2009). However, most conventional DNA extraction methods still require trained operators and multiple handling steps that are difficult to transfer onto lab on a chip systems. In fact, the complexity of integrating sample preparation processes with microfluidic systems remains one the major obstacles to the widespread adoption and use of microfluidic instruments in point of care settings (Chen *et al.*, 2007a, Kim *et al.*, 2009, Price *et al.*, 2009, Whitesides, 2006). As a result, considerable effort has been invested by many research groups to uncover optimal on-chip sample preparation solutions. This is evident in the volume of SP-related publications in the literature.

Chen *et al.* (2007a) summarized progress towards the development of a fully integrated lab on a chip system for nucleic acid analysis. The authors noted that while there have been several demonstrations of integrated nucleic acid amplification and analysis, sample preparation remains a limiting process in the development of point of care systems. Also, Dineva *et al.* (2007) reviewed commercial and prototype systems for point of care sample preparation for nucleic acid testing and concluded that state of the art on-chip SP technologies are complex and expensive. Meanwhile, Brennan *et al.* (2009) state in their review that an ideal point of care LOC system would have a capital cost less than $2000 and a cost per test less than $10. These reviews suggest that the key challenges that remain in the development of SP technologies for fully integrated LOC systems for point of care applications are **complexity** and **cost**.

I will begin with a short summary of the main approaches to on-chip cell lysis. Cell lysis is the first step in on-chip SP and it involves the breakdown of cells or tissues in the raw sample so that nucleic acids can be analyzed in downstream reactions. Kim *et al.* (2009) and Bao and Lu (2008) provide detailed reviews of state of the art cell lysis techniques. Four main cell lysis paradigms emerge from these reviews: chemical, electrical, mechanical, and thermal methods. Thermal lysis involves boiling cells for a short time so that their membranes are damaged but the DNA contained within is intact. Mechanical lysis makes use of microfabricated structures that pierce cells and free their contents. Electrical lysis employs strong (and often pulsed) electric fields to damage cell membranes. Finally, chemical lysis uses reagents to break down cell membranes.

While there has been considerable research into each of these methods, chemical lysis is the most common technique in the literature because it is a more direct adaptation of conventional cell lysis methods (Kim *et al.*, 2009). However, each of these cell lysis methods is closely linked to the chosen approach to downstream nucleic acid extraction. Optimal cell lysis methods must minimize the complexity of integrating cell lysis with DNA separation, amplification, and analysis (Bahi *et al.*, 2011, Bao and Lu, 2008).

I will now provide a detailed evaluation of DNA extraction methods and discuss the key challenges that remain in the development of integrated on-chip SP solutions. I will provide an overview of on-chip SP methods by referring to reviews that provide comprehensive summaries and classifications of the field. Thereafter, I will provide a detailed survey of DNA purification with functionalized magnetic beads – the AML's chosen method for on-chip SP.

On-chip SP reviews by Chen *et al.* (2007a), Kim *et al.* (2009), Price *et al.* (2009) can be broadly classified into four main groups, namely:

1. silica-based SPE
2. electrostatic attraction
3. nanomembrane filtration
4. functionalized magnetic beads

These groups encompass the main state of the art approaches to DNA purification on microfluidic platforms.

3.2.1 Silica-based SPE on-chip

As discussed in section 3.1.2, solid phase extraction (SPE) techniques are the gold standard method for conventional automated DNA extraction. Consequently, microfluidic approaches to DNA purification often adopt SPE as a starting point (Price *et al.*, 2009). There are numerous demonstrations of silica SPE on-chip. Price *et al.* (2009) provide a detailed survey of state of the art SPE on microfluidic platforms.

One of the dominant approaches to on-chip SPE with silica is the fabrication of high surface area silica structures (Cady *et al.*, 2005, Christel *et al.*, 1999). This involves passing DNA through silica microstructures in the presence of chaotropic salts, followed by wash steps to remove unwanted cellular material and elute DNA. Chen *et al.* (2007b) used silica microcolumns to perform solid phase extraction of DNA from whole blood with 70% extraction efficiency. Hwang *et al.* (2008) extracted bacterial DNA from whole blood with silica micropillars and performed on-chip real time PCR to analyze the presence of bacterial pathogens in the sample. Their automated approach for flowing samples through the silica structures resulted in an extraction efficiency of 75%. Baier *et al.* (2009) presented a state of the art demonstration of complete SP (i.e cell lysis and DNA extraction) coupled with on-chip amplification and detection. The authors devised a disposable polymer microchip with a credit card form factor. This system employed a silica membrane to bind DNA in the presence chaotropic salt solutions. This device was applied to the detection of human papillomavirus (HPV) from cervical fluid. Implementation of complete purification, amplification, and analysis on the same microchip represented a significant step toward the development of a true point of care system. Shaw *et al.* (2011) moved even closer to a point of care system based on silica microstructures by pre-loading DNA extraction and amplification reagents onto a microchip using an agarose gel resevoir. DNA was extracted from human buccal cells using a microfabricated silica block and chaotropic salts, amplified using a Peltier element, and analyzed by conventional CE.

While silica microstructures achieved comparable DNA purification efficiency as conventional silica kits, complex fabrication processes (such as deep reactive ion etching) were required to create the high surface area DNA-binding structures (Price *et al.*, 2009). Consequently, attempts have been made to reduce the difficulty of fabrication by using materials that are easier to shape than silica & glass. This has the added benefit of facilitating low-cost and disposable sample preparation units for lab on a chip systems (Mahalanabis *et al.*, 2009). For example, Witek *et al.* (2006) used photoactive polycarbonate to create posts with large surface area to bind to DNA. Mahalanabis *et al.* (2010) performed solid phase extraction using disposable plastic columns and applied their device to the detection of bacterial DNA. Similarly, the Landers group developed microfabricated DNA-binding posts out of poly methyl methcrylate (PMMA) because the material allows for reproducible manufacturing of high surface area posts by X-ray lithography (Reedy *et al.*, 2011). However, the use of materials other than silica for SPE columnar structures is still very new and many of the materials are fragile, hinder fluid flow, or have limited compatibility with reagents required for downstream applications such as PCR (Price *et al.*, 2009, Reedy *et al.*, 2011).

While silica-based SPE with chaotropic salts has the highest extraction efficiency when compared to other on-chip sample preparation methods (Kim *et al.*, 2009), it requires multiple wash steps to remove chaotropic salt solutions that could inhibit downstream reactions (e.g. PCR). This increases the complexity of silica-based SPE and limits its adoption in point of care systems.

3.2.2 Electrostatic attraction

DNA extraction by electrostatic interactions involves nucleic acid extraction by manipulating the surface charge of the binding molecule (Nakagawa *et al.*, 2005). This approach to DNA separation is advantageous because it eliminates the need for multiple wash steps to remove chaotropic salts that may inhibit downstream reactions in traditional silica SPE (Kim *et al.*, 2009). In addition, DNA extraction with electrostatic methods usually does not require complex microfabrication processes for high surface area that increase the difficulty and cost of chip-based systems.

There have been several demonstrations of DNA extraction using electrostatic methods using materials such as amine coatings (Nakagawa *et al.*, 2005), naturally occurring sugars (Cao *et al.*, 2006), and polycarbonate (Witek *et al.*, 2006). The distinguishing feature of these materials is that their surface charge can be regulated so that they bind or release DNA depending on the properties of the surrounding solution (Kim *et al.*, 2009). For example, (Nakagawa *et al.*, 2005) coated a silicon microchip with amino groups to induce DNA-binding at different pH levels. Amino groups are positively charged at low pH levels so they bind to negatively charged DNA, and at high pH levels the now-negatively charged amino groups elute DNA. This method resulted in up to 40% DNA purification efficiency while leaving behind cellular proteins. Similarly, Cao *et al.* (2006) addressed used chitosan (a naturally occurring sugar) to bind DNA. The surface charge of chitosan depends on the pH of the surrounding solution, and permits DNA extraction by surface charge switching. At low pH conditions (pH < 5) chitosan binds to DNA, and at high pH conditions (pH > 9) it releases the DNA. Chitosan coated beads were used to extract DNA from whole blood at up to 90% extraction efficiency while retaining compatibility with downstream PCR reagents. In addition, the Sp step was performed in an open silica channel that did not require complex microfabrication.

However, in their review, Kim *et al.* (2009) found that electrostatic SP methods have the lowest extraction efficiency when compared to other state of the art on-chip DNA extraction methods (e.g. silica SPE). In addition, the speed of the separation reaction is slow since time is required to chemically modify the surface charge of the DNA-binding materials (Nakagawa *et al.*, 2005). Also, electrostatic methods require mechanisms for fluid flow to move purified DNA away from unwanted cellular debris. Such fluid control systems are often difficult to integrate and automate on chip-based systems and often lead to the use of macroscale infrastructure such as syringe pumps (Easley *et al.*, 2006, Kim *et al.*, 2009).

3.2.3 Nanomembrane filtration

Membrane filtration is another approach to DNA extraction on microfluidic platforms. It consists mostly of the use of membranes (often with attached microstructures) that are used to act as filters for cells and nucleic acids (Kim *et al.*, 2009). Crowley and Pizziconi (2005) developed microfilters for the separation of cells from plasma in parallel microarray applications. Similarly, Irimia and Toner (2006) demonstrated cell extraction and pre-concentration from whole blood using nanostructures fabrication on membranes. Nguyen *et al.* (2009) developed a chip-based biosensor device by physically implanting antibody probes onto the walls of nanomembranes. The antibody probes were used to perform immunoassay-based detection of viral particles in blood with a 7% detection rate. Kim and Gale (2008) found that aluminum oxide membranes with 100 nm pores provided optimal DNA extraction efficiency out of membranes with pore sizes ranging from 10 – 250 nm. The aluminum oxide membrane takes advantage of both physical filtration and chemical attraction of DNA to the surface. The authors presented an improved membrane design with a lower membrane volume to reduce PCR inhibition effects (Kim *et al.*, 2010) and to incorporate integrated downstream amplification on the same plastic microchip.

While membrane filtration SP methods are quicker than silica-based and electrostatic methods and provide excellent extraction efficiency (Kim *et al.*, 2009), their integration with on-chip systems is complicated by the need for specialized fabrication methods to generate optimal pore sizes for DNA extraction (Kim and Gale, 2008). In addition, materials that provide excellent physical filtration and chemical attraction of DNA can also inhibit PCR at high volumes (Kim *et al.*, 2010).

3.2.4 Functionalized magnetic beads

Functionalized magnetic beads are another major approach to DNA purification on microfluidic platforms. This technique involves extracting DNA from raw samples using specially labeled magnetic particles that bind preferentially to DNA. The magnetic nature of the particles (or beads as they are commonly known) allows their separation from the raw clinical sample by the application of an external magnetic field (Gijs *et al.*, 2010, Kim *et al.*, 2009). Although the review by Kim *et al.* (2009) describe magnetic bead-based SP methods as difficult to implement on-chip, there has been considerable interest in the automation and application of bead-based DNA purification assays on lab on a chip systems. DNA purification with functionalized magnetic beads is desirable because magnetic particles can be coated with sequence-specific antibodies or probes that improve SP yield (Karle *et al.*, 2010, Lee *et al.*, 2009, Liu *et al.*, 2011). Also, the use of micro-scale magnetic beads provides plenty of surface area to bind to DNA (Gijs *et al.*, 2010), and facilitates concentration of trace amounts of analytes into small volumes suitable for on-chip work (Lichtenberg *et al.*, 2002, Lin *et al.*, 2011, Ramadan and Gijs, 2011). In addition, many functionalized magnetic bead kits have been demonstrated in conventional settings and are available commercially (Gijs *et al.*, 2010, Liu *et al.*, 2011).

For example, paramagnetic silica beads have been used to bind DNA in the presence of chaotropic salts and separate the purified DNA from raw clinical samples with magnetic fields rather than complex fluid flow systems (Duarte *et al.*, 2010, Lehmann *et al.*, 2006, Zhang *et al.*, 2010). These demonstrations use magnetic silica beads to extract DNA from clinical samples in the presence of chaotropic salt solutions, followed by on-chip amplification and analysis. The magnetic nature of the beads is primarily to facilitate separation of the DNA from the raw sample without the need for multiple wash steps (Lehmann *et al.*, 2006).

In order to achieve true point of care applications, magnetic bead-based DNA purification systems need to be automated to minimize human intervention and maximize yield (Liu *et al.*, 2011, Ramadan and Gijs, 2011). In order to achieve these goals on microfluidic platforms, two main design considerations appear in state of the art demonstrations of magnetic bead-based DNA purification, namely:

- **choice of magnet**: permanent magnet versus electromagnet
- **bead capture paradigm**: trapping versus transport.

Electromagnet or permanent magnet

In order to manipulate functionalized magnetic beads, external magnetic fields need to be applied to the sample. There are two main approaches to supplying the external magnetic field: permanent magnets and electromagnets. Electromagnets for bead actuation can be readily turned on and off by the application of an electric current (Gijs *et al.*, 2010) – making them conducive to trapping applications that require the magnetic beads and attached DNA to be held stationary while the raw sample is washed away (Lien *et al.*, 2009).

There have been multiple demonstrations of on-chip DNA purification using electromagnetic coils on the bottom of the microfluidic chip which are activated and hold the magnetic beads (and attached DNA) at the bottom of the separation channel / chamber while unwanted materials are washed away (Azimi *et al.*, 2011, Ganguly *et al.*, 2010, Smistrup *et al.*, 2005, Tennico and Remcho, 2010, Yamanishi *et al.*, 2010). However, manipulating beads with electromagnets is susceptible to heating effects that may damage the sample (Lien *et al.*, 2009, Ramadan and Gijs, 2011). While there have been attempts to take advantage of the heat generated by electromagnet coils for use in on-chip PCR (Lien *et al.*, 2009), the need to account for the heating from electromagnets sets additional constraints on the design of on-chip SP systems (Gijs *et al.*, 2010).

Consequently, permanent magnets are usually more effective and less complex sources of magnetic fields for on-chip bead manipulation (Hatch and Stelter, 2001, Ramadan and Gijs, 2011). There are several examples of bead trapping with handheld permanent magnets to purify DNA from clinical samples (Bahi *et al.*, 2011, Hu *et al.*, 2011, Peeters *et al.*, 2010, Wang *et al.*, 2011, Welch *et al.*, 2011, Yeung and Hsing, 2006). However, because permanent magnets cannot be turned on or off as easily as electromagnets they need to be moved far enough away from the DNA purification region when their influence is no longer needed. For repeatable point of care and reproducible results the magnet motion needs to be automated (Gijs *et al.*, 2010). While this increases the complexity of on-chip DNA purification systems, there have been several demonstrations that employ integrated motor-controlled permanent magnets for DNA purification on lab on a chip system (Hopwood *et al.*, 2010, Hurth *et al.*, 2010, Pipper *et al.*, 2008, Ramadan and Gijs, 2011).

Bead trapping or transport

After deciding on a source of the magnetic field, a suitable bead capture mechanism must be chosen. There are 2 main approaches to manipulation magnetic beads on lab on a chip systems: holding beads stationary and washing away unwanted materials (Chen *et al.*, 2010, Wu *et al.*, 2010) or dragging the beads away from the raw clinical sample (Duarte *et al.*, 2010, Ramadan and Gijs, 2011).

Bead trapping can be accomplished by creating an external magnetic field and holding the beads against the wall of the separation chamber while unwanted cellular materials are washed away with fluid flow (Chen *et al.*, 2010, Martínez *et al.*, 2010, Tennico and Remcho, 2010, Wu *et al.*, 2010, Yamanishi *et al.*, 2010). For example, Lien *et al.* (2009) used static Chargeswitch beads and electromagnetic coils to purify DNA from human saliva samples. Similarly, the Mathies research group used sequence-specific magnetic beads held stationary in a separation chamber to bind DNA in a fully integrated lab on a chip system for sample-in answer out analysis (Liu *et al.*, 2011).

However, bead trapping is inefficient because potentially inhibitory materials also get bundled into bead conglomerates that form on the walls of the separation chamber – reducing the purity of extracted DNA and the efficiency of microfluidic DNA analysis (Hatch and Stelter, 2001, Ramadan and Gijs, 2011).

To address this limitation of bead trapping systems, lots of modifications have been made to static bead separation. For instance, self-assembled magnetic beads and microstructures in the separation chamber have been combined with external magnetic fields to increase the surface area available for DNA binding and improve purification efficiency (Issadore *et al.*, 2011, Mohamadi *et al.*, 2010, Saliba *et al.*, 2010, Sivagnanam *et al.*, 2010, Yu *et al.*, 2011). In addition, quadrupolar magnet arrangements have been used enhance the efficiency of DNA purification with magnetic fields by controlling the trajectory of the magnetic particles and allowing them to scan zones inside the purification chamber for the analyte of interest (van Pelt *et al.*, 2011, Williams *et al.*, 2009).

However, these demonstrations with elegant magnet arrangements increase the complexity of on-chip DNA purification systems (Gijs *et al.*, 2010). As a result, bead transport, an alternate and more efficient bead capture paradigm is often employed in the literature. Bead transport involves moving beads away from lysed clinical samples instead of holding them stationary. This usually maximizes the washing of the beads and allows ample opportunity to remove unwanted debris lodged within the bead clump (Ramadan and Gijs, 2011).

Although bead transport provides greater purification efficiency, its associated tradeoff is the need for a large magnetic field gradient to move beads – greater than the magnetic field required to keep beads stationary (Gijs *et al.*, 2010). Also, motion control systems are often required to move permanent magnets in order to create the required magnetic field gradient (Hopwood *et al.*, 2010, Hurth *et al.*, 2010).

3.3 Design of initial approach

The on-chip DNA purification system described here is based on the transport of magnetic beads through a separation channel to purify DNA from lysed human cheek cells. The initial design of the SP system was laid out by Dr. G.Kaigala, and I continued with the project when I joined the AML. This project was conceived as a follow up to past work that demonstrated inexpensive genetic amplification and analysis on a single microchip and instrument (Kaigala *et al.*, 2008). The novelty of the DNA purification project would lie in the use of a dynamic DNA purification process that automated the motion of an external permanent magnet with stepper motors and carried out DNA extraction, amplification, and analysis from lysed cells with minimal human intervention. Also, Chargeswitch magnetic beads would be used for DNA extraction on-chip by pH-controlled capture and release of DNA.

However, there have now been published demonstrations in the literature of dynamic magnetic bead-based DNA purification from raw clinical samples with automated permanent magnet control for repeatability (Duarte *et al.*, 2010, Hopwood *et al.*, 2010, Hurth *et al.*, 2010, Ramadan and Gijs, 2011). The Landers group transported magnetic beads across a separation channel to purify DNA from raw clinical samples and found that this was advantageous to a static bead extraction approach (Duarte *et al.*, 2010) – but still with manual magnet control.

Ramadan and Gijs (2011) rotated an array of permanent magnets with a DC motor to transport magnetic beads coated with mouse antibodies. The magnets were rotated sequentially to move the bead plug down the length of the separation channel. The beads were sequentially trapped and released to improve the washing of the DNA and improve the extraction efficiency. The sample preparation system was used to detect mouse antibodies using a sandwich immunoassay and fluorescent detection with a fluorescence microscope.

Furthermore, Hopwood *et al.* (2010) used Chargeswitch® magnetic beads to extract DNA from human buccal cells on a microfluidic platform for forensic analysis. The automated SP system made use of a servomotor to move the permanent magnet that transported beads and attached DNA away from cell lysate, followed by thermal cycling with a Peltier element, and DNA analysis with miniaturized high voltage supply for microchip CE.

Similarly, Hurth *et al.* (2010) used a permanent magnet attached to a servo motor controller to purify DNA attached to Chargeswitch® magnetic beads from human buccal swabs. This was followed by automated transfer of the sample into a PCR chamber using paraffin valves, on-chip thermal cycling using a Peltier element, and microchip CE. This system was applied to DNA fingerprinting for forensic applications.

Nevertheless, the systems described above still need to be optimized to meet the cost, portability, and time requirements for a point of care system (Brennan *et al.*, 2009, Dineva *et al.*, 2007, Kim and Gale, 2008). The system presented by Ramadan and Gijs (2011) employs syringe pumps for fluid control and uses a large and expensive fluorescence microscope for optical detection. Hopwood *et al.* (2010) presented an integrated SP-PCR-CE solution; however, the system still required a well-trained operator and had a run-time of 4 hours. While Hurth *et al.* (2010) used pre-loaded cartridges to facilitate hands-free sample analysis, the overall reaction took three and half hours to complete. There is still work to be done to allow the use of microfluidics systems for DNA purification in point of care settings.

I will now describe the implementation of magnetic bead-based DNA purification using Chargeswitch® magnetic beads and an automated XY stage for permanent magnet motion. Tube-based experiments were first performed to validate the performance of the DNA purification protocol. Thereafter DNA purification was performed with the XY stage and integrated with on-chip real time PCR and melting curve analysis. I will begin the discussion with a description of the XY stage.

3.3.1 XY stage

Because SP is the first step of the POC diagnostic, it sets an efficiency limits on the remaining downstream processes. As a result, the SP process must be efficient in the extraction process. In addition, a suitable SP mechanism must allow the extraction of nucleic acids rapidly and with limited external infrastructure with provision for future miniaturization of the device. Towards this end, we developed an automated XY stage to operate a magnetic-bead based sample preparation technique.

As part of my undergraduate final year project (EE 401), I built the automated SP stage along with D.Cao, T.Voon-How, & H.Lu. This work was completed under the supervision of Dr.Backhouse and V.Sieben at the AML. We custom-designed an X-Y stage to move a magnet with micrometer-precision in vertical and horizontal directions. The X-Y stage was designed to allow a wide range of magnet motion in 2 dimensions for highly versatile operation and to perform complex choreography. The stage was built (~ $300 in labour) from two aluminum plates, each approximately 7 cm^2.

The Atmel microcontroller (Atmega 32, Atmel Corporation, San Jose, USA) receives movement commands from the toolkit's central PIC microcontroller unit (PIC18F455O, Microchip technology inc., Arizona, USA) via a Serial Peripheral Interface (SPI). The PIC18F455O is designated as the "master" and supplies SPI control inputs to the Atmel (the "slave") to initiate XY motion of the stepper motors. The stage's microcontroller translates these commands into coordinated PWM pulses that cause the motor controller chips to drive the stepper-motor-based X-Y stage linear actuators (26DBM10D2U-L, Portescap Danaher Motion, Pennsylvania, USA). The linear actuators are chosen for their fine 25.0-μm step resolution, and large 26-mm movement range.

Furthermore, a controller-driver circuit is used to operate the stepper motors for X-Y stage movement. This circuit consists of a motor controller and a motor driver. Two motor controllers (L297, STMicroelectronics, Mississauga, Canada) - one for each motion axis – are used to translate clock pulses and direction logic from the Atmel microcontroller into stepper motor control waveforms. The step waveforms from both motor controller chips feed into a motor driver (ULN2803A, STMicroelectronics, Missassauga, Canada) that consists of eight Darlington pairs (four pairs per motor controller). The motor driver chip responds to the step waveforms by energizing corresponding coils within the stepper motors to physically move the motors.

A reference absolute position is obtained through an initialization software routine that zeros the stage with 2 optical switches. Photo logic slotted optical sensors (OPB930W, Optek Technology, Texas, USA) with high sensitivity, 3.18mm slot width and 3.3 mm sensing distance are used to implement the initialization. They are small and lightweight and do not hinder stage mobility. When the sensors are blocked they output 0.4V, otherwise they supply 2.4V. Two low power operational amplifiers (MC33172, STMicroelectronics, Missassauga, Canada) are used to convert optical sensor voltages to TTL logic levels of 0V and 5V. Consequently, when an optical sensor is blocked, the input voltage to the microcontroller is 0V and when its clear, the input voltage to the microcontroller is 5V. This allows easy determination of the XY stage's zero position.

Magnetic force on the beads

The microchip design includes a simple, valveless 13 mm separation channel bounded on either side by a 2 mm diameter and 1.1mm depth well. To determine how far the external permanent magnet (Magcraft grade N40 Rare-Earth Neodymium-Iron-Boron (NdFeB) Discs, 0.25 inch diameter, 0.125 inch thickness) should be placed away from the microchip, we performed calculations to estimate the magnetic field experienced by the beads inside the separation channel. A simplified model of bead motion through the separation channel assumes that we need to supply sufficient magnetic force to overcome frictional force preventing bead motion through SP channel – here we assume negligible fluid flow and gravitational force, and calculate the force required to overcome only hydrodynamic interactions. In his PhD thesis, Sieben (2009) calculated the magnetic force on the beads at various distances from the chip. When the magnet is placed 2 mm away from the chip, the beads experience a force B = 0.2 Tesla, ΔB = 93.9 Tesla/m, and Force = 140.5 pN.

Sieben (2009) also empirically determined that the optimal vertical separation between the microchip and the permanent magnet was 2mm. At a 2 mm separation, the beads were captured by the magnet and uniformly dragged across the separation channel. At 5mm separation, the beads "hopped" along the channel surface and there were noticeable lines along the channel as beads stuck to its surface. In this regime, "wiggling" the magnet from side to side helped to capture more beads and reduce sticking. Above 15mm separation, the magnetic beads did not show significant motion even when the magnet was jerked vigorously from side to side. I followed the design laid out by Sieben (2009) and positioned the permanent magnet 2 mm away from the microchip to ensure uniform bead motion along the separation channel.

Bead clumping in separation channel

Because the amount of DNA collected during the SP step limits the concentration of analytes available for downstream amplification and analysis, it is important to maximize the amount of DNA collected during the SP step. When I joined the AML, on-chip SP was performed manually i.e. the operator moved a permanent magnet by hand and tried to transfer beads from the SP input to output well. This approach was not repeatable and required an experienced operator to obtain significant transfer of beads during the on-chip SP process.

In addition, beads often formed large clumps that were too big to enter the separation channel. Clumping occurred most often at the start of the SP experiment. Magnetic bead clumping occurred most often at the start of the on-chip SP experiment when the lysate mix[2] is added to the SP input well. During this step, the permanent magnet is positioned directly underneath the input well – resulting in beads rushing towards the magnet and forming a large clump at the bottom of the well. In about half of the experiments, the mass of beads formed in the input well was too large to enter the separation channel, and needed to be moved by hand back and forth to break them up into little pieces that could fit into the separation channel. This manual manipulation of beads was not repeatable and increased the time required for DNA separation – and increasing the time available for cellular debris to diffuse across the separation channel and into the SP output well.

When SP was performed using the automated XY stage, bead clumping prevented repeatable DNA separation. I explored approaches to remedy this problem. I avoided changes

---

[2] SP lysate mixture contains biological samples and magnetic beads and its preparation is described in section 3.3.2.

to microchip design given the cost and lead time associated with such endeavours. A simple and repeatable protocol change to eliminate bead clumping would be the ideal solution.

My first attempt was to choreograph magnet motion so that the bead clump was moved from side to side within the input well. The objective was to break up the bead clump into smaller chunks that could enter the separation channel – mimicking the manual solution to the bead clumping problem. The wiggle action was implemented by sending motion commands to the stepper motor with specifications for the center and extremes of the back and forth motion[3]. However, I found that even when the magnet was wiggled back and forth over a 2-mm radius at the start of the on-chip SP experiment, the bead clumping problem persisted. It appeared that manual manipulation of the permanent magnet was required to finesse the beads into the separation channel once a clump had formed.

At this point, I decided to eliminate the bead clump by altogether avoiding its formation – removing the need for intricate (and unrepeatable magnet motions). To accomplish this, I changed the starting position of the permanent magnet from directly beneath the SP input well to just on the edge of the separation channel i.e. ~2mm inside the separation channel on the input side (see figure 3.3.3). In this scenario, when the magnetic beads are added to the SP input well they are immediately drawn into the separation channel and form a bead column inside the channel. This bead column could be moved successfully through the separation channel and into the SP output well. With this protocol change, there were no more bead clumping problems and over 95% of the beads added to the SP input well were successfully transferred into the output well. I estimate that 95% of the beads were transferred into the output well based on visual inspection of over 20 on-chip SP runs. I estimate that 5% of the beads stick to smooth surfaces along the walls of the SP input well.

SP firmware

I wrote firmware in C++ to automate motion of the XY stage from the SP input well to the output well. This consisted of sending bytes containing X and Y commands to the microcontroller unit attached to the XY stage[4]. I designed the firmware so that the XY moved in steps of 1.3 mm and waited for 5 s after each motion to allow the bead column in the separation channel to catch up. I implemented a second sweep of the magnet across the separation channel following the same pattern of 1.3-mm steps and 5-s waits to ensure that no beads were left in the separation channel. Dr. R. Johnstone improved on this draft of the SP firmware. He rewrote the firmware so that the magnet moves continuously in steps of 25.4 μm and completes a single sweep of the separation channel in 100 s. This approach ensures that beads and held close to the magnet and reduces the likelihood of beads being left behind because the magnet moved too quickly[5].

The XY stage has preset start and stop positions of the permanent magnet with coordi-

---

[3] The wiggle motion was implemented during my undergraduate final year project and is described in the "XYstage Report EE401 2008" file in the supplementary information CD.

[4] My SP script is provided in the "sp-firmware.c" file in the supplementary information.

[5] Dr Johnstone's version of the firmware is provided in the "sp.c" file in the "TTK Firmware version 300" folder in the supplementary information CD.

nates ranging from 0 to 1000 units in the X and Y directions. When the system turns on, the position of the magnet is zeroed to X and Y coordinates of (0,0) by the action of the optical sensors. The coordinates of the SP channel and wells are fixed based on how the TTK gantry was designed – and do not vary from chip to chip (unless there are errors/misalignments during microfabrication). The first step in the SP process is to move the magnet to (420,435) so that it is centred vertically in the middle of the separation channel and located just on the outside of the SP input well as shown in figure 3.1 – this follows the discussion in section 3.3.1 about reducing bead clumping. Next, the XY stage is moved the magnet at in 25.4 μm steps from (420, 435) to (0,435) – dragging the beads and attached DNA into the SP output well in the process. The total run time for moving the beads from the input to the output well was chosen as 100s to allow sufficient time for magnetic beads to move across the separation channel but not enough time for diffusion of unwanted biological components (e.g. cellular debris and lysis buffer). The magnet is held in place for 1 minute while the separation buffer is removed[6]. Finally, the XY stage moves the magnet back to (0,0) to complete the automated SP process.

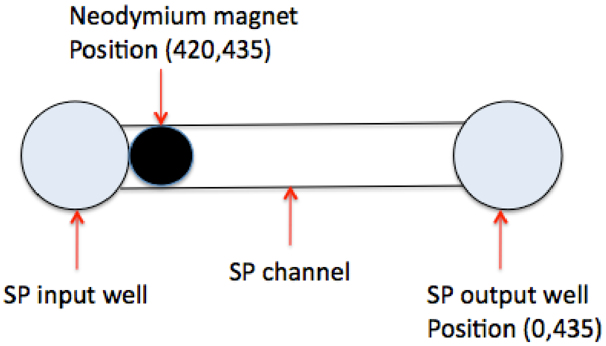

Figure 3.1: Starting position of the permanent magnet and SP output well. The coordinates are set according to the design of the TTK gantry and range from 0 to 1000 units in the X and Y directions. The magnet's starting position is (0,0) then it moves to (420,435) just prior to the start of the SP process. When beads are added they are immediately drawn into the separation channel without clumping because of the position of the magnet. Then the XY stage moves the magnet and beads to the SP output well located at (0,435)

3.3.2 Off-chip DNA purification (reference method)

The conventional DNA purification process involves the use of a micropipetter, a swab, and reagents from a standard sample preparation kit (ChargeSwitch™ gDNA Buccal Cell Kits, Cat. # CS11021, Invitrogen, Carlsbad, CA). Nucleic acids are purified using Chargeswitch™ magnetic beads by controlling their surface charge with the pH of the surrounding liquid.

---

[6] Removal of the separation buffer is done manually with a pipette as described in "TTK SPPCRCE Protocol v1.02" in the supplementary information. This is one of the few manual steps involved during on-chip SP, and work is underway at the AML to replace this with an automated valve-based approach.

In low pH conditions ($pH < 6.5$), Chargeswitch™ beads are positively charged and bind to the negatively charged backbone of DNA. The bead/DNA conjugate is separated from the surrounding solution by the application of a magnetic field and the DNA is subsequently eluted in high pH conditions ($pH > 8.5$).

The standard off-chip (i.e. tube-based) extraction was performed as a reference experiment to test the Chargeswitch™ kit and to compare with on-chip results. For efficient on-chip purifications, the manufacturer's protocol was modified by replacing the Chargeswitch™ wash buffer and elution buffer with our SP separation matrix (25% sucrose, 1% Tween20, in Chargeswitch™ wash buffer) and PCR master mix, respectively. Tween20™ was used to enhance bead washing effects to remove debris while sucrose was added to the separation matrix to increase its density and viscosity and prevent diffusion across the separation channel (Jegat *et al.*, 2001). Meanwhile, elution buffer was eliminated since the DNA could be eluted by simply mixing with PCR reagents ($pH > 8.5$).

The ß2m gene was purified from human cheek cells to test our SP protocol and reagents. Buccal swabs were obtained from a healthy volunteer with informed consent using a 15 cm sterile swab (AMG Medical, Montreal, QC) applied to the left and right buccal surfaces for 30 seconds each. The DNA extraction process does not inactivate potential biohazards in the biological sample. Consequently, all SP materials were treated like potential biohazards, and the use of a biosafety hood and strong lab safety practices are required for this work. Furthermore, to reduce collection differences the same volunteer provided all buccal swabs. When multiple experiments were performed on the same day, up to 3 swabs were collected from the same cheek – this could introduce variations in the amount of cells (and DNA) extracted by the SP process.

The swabs were incubated for 15 minutes in 500 μL of lysis buffer to elute and lyse the epithelial cells. This was followed by a 10-minute incubation with 5 μL of Proteinase K to digest histones and improve primer access to DNA during PCR. Subsequently, 25 μL of purification buffer, 5 μL of Chargeswitch® beads (stored in 10 mM MES (2-(N-morpholino) ethanesulfonic acid), pH 5.0, 10 mM of NaCl, 0.1% Tween20), and 12 μL of 10% Tween20(TM) (Sigma Aldrich, USA) were added to produce a mixture we referred to as the "SP lysate". 5 μL of SP lysate was added to a tube containing 5 μL of SP separation matrix (25% sucrose, 1% Tween20 in ChargeSwitch® wash buffer). The lysate was mixed thorougly with the separation matrix by pipetting up and down.

The Chargeswitch® kit manufacturer's method for collecting magnetic beads from the SP lysate calls for forming a bead clump at the bottom of a test tube and removing all the supernatant[7]. Subsequently, the beads were washed with Invitrogen elution buffer and again all the supernatant was removed while holding the beads in place with a permanent magnet. Finally, PCR reaction mix was added to the beads. To mirror on-chip separation processes as closely as possible, the bead collection process was modified. The magnetic beads were collected into a pellet at the bottom of the tube using an external magnet. Next, 1 μL of the bead suspension was removed using a micropipetter. Instead of adding the entire

---

[7] See "Chargeswitch® gDNA blood kit" instruction manual in supplementary information.

1 μL volume of beads and SP separation matrix present in the pipette tip to the PCR mix, only the magnetic beads were transferred by placing a permanent magnet directly under the PCR tube. This process left behind almost all the separation matrix in the pipette tip. This ensured that the beads were transferred into the PCR reaction with minimal volume contributions from the SP separation matrix[8].

After adding magnetic beads from off-chip sample preparation to the PCR mixture, thermal cycling was performed in a commercial PCR machine (PTC-200, MJ Research, MA, USA). The thermal cycling conditions were pre-denaturation at 90˚C for 120s, post-extension at 72˚C for 120s, and 35 cycles of denaturation at 90˚C for 10s, annealing at 60˚C for 20s, and extension at 72˚C for 20s. A 24 μL PCR reaction mixture for the amplification of ß2m DNA from SP contains 2.5 μL of 10X PCR buffer (containing 200 mM Tris-HCl and 500 mM KCl, pH 8.4), 2.0 μL of 50 mM MgCl2 (final concentration of 4 mM), 0.5 μL (5U/μL) of platinum Taq polymerase, 0.5 μL of 10 mM dNTPs, 0.5 μL of 1% BSA, 1.0μL of DMSO (4%), 0.5 μL of reverse primer, 0.5 μL of Alexa-647-labeled forward primer, 2.5 μL of 10x LCgreen plus™ (Idaho Tech., USA), 13.5 μL of PCR grade water (nuclease-free, MP Biomedicals Inc. OH,USA). For SP tests, magnetic beads are added to the master mix. This is replaced with 1 μL of distilled water for no-template controls and 1 μL of 50 ng/μL of ß2m genomic DNA for positive controls). Pt Taq DNA polymerase kits (including Pt Taq, 10X PCR buffer and MgCl2), forward and reverse primers were ordered from Integrated DNA Technologies (Coralville, IA, USA), and dNTPs were purchased from Invitrogen Canada Inc. (Burlington, ON, Canada).

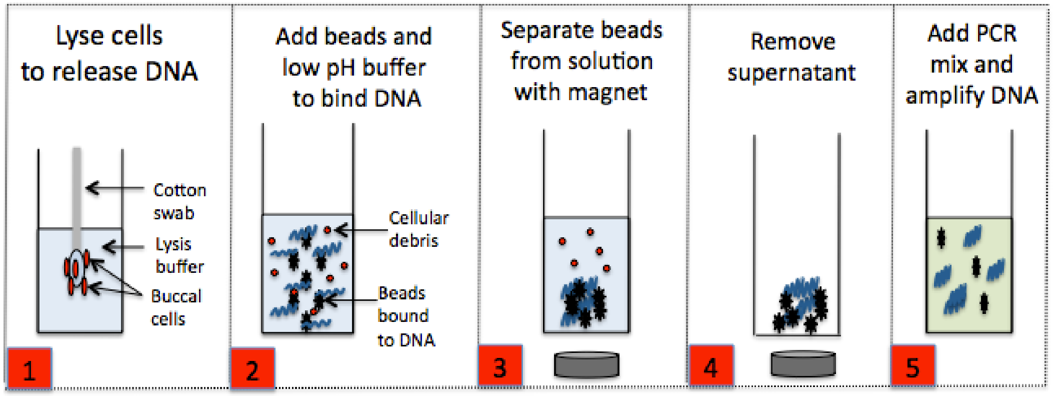

Figure 3.2: Illustration of multiple step processes performed using conventional tube-based DNA purification. (Adapted from Invitrogen Product Manual)

3.3.3 On-chip DNA purification

To perform on-chip SP, cheek swabs were obtained and incubated (as described above for the off-chip separation method) and the SP lysate was prepared using the same reagents.

---

[8] The manufacturer does not recommend adding washing buffers to PCR reactions as described in the instruction manual in the supplementary information.

The SP output well (see fig. 3.3) was filled with 5 μL of separation matrix. At this point, a syringe is applied to the SP input well to suck the separation matrix from the output well until it filled the separation channel right up to the edge of the input well. This ensured free-flowing motion of beads through the channel. The magnet was then positioned at its starting coordinates on the edge of the SP input well (as discussed in section 3.3.1).

Next, 4 μL of SP lysate was added to the SP input well. The magnetic beads were immediately drawn into the SP channel under the influence of the permanent magnet. At this point, automated SP motion was carried out by the SP module driven by the C++ firmware described in section 3.3.1. The magnetic beads (and attached DNA) were dragged through the separation matrix and into the SP output well. We believe that the density and viscosity of the separation matrix enhanced the helped to wash the beads and enhanced separation of the beads from unwanted cellular debris.

At the end of automated XY stage motion, the beads were held in place by the permanent magnet in the center of the output well. Then the contents of both the input and output wells were emptied with a micropipetter leaving only the beads in the output well. Subsequently, 4.8 μL of ß2m PCR mix was added to the output well in preparation for on-chip PCR. The 24-μL master mix described in section 3.3.2(containing everything but beads and DNA) was divided into five 4.8 μL aliquots. Magnetic beads from on-chip SP were added to one such aliquot and accompanied by no-template controls with 0.2 μL of water or positive controls with 0.2 μL of 50ng/μL ß2m genomic DNA. The magnet was moved to its zero coordinates (0,0) and the beads and PCR reagents were mixed by pipetting up and down several times. The pH of the PCR mix (pH of 8.8) was high enough to elute DNA from the magnetic beads. Finally, 5 μL of the mixture of PCR reagents, DNA, and magnetic beads was transferred from the SP output well on the microchip into a PCR tube which was placed in a conventional PCR machine for off-chip thermal cycling (PTC-200, MJ Research, MA, USA) using the same PCR conditions as in section 3.3.2.

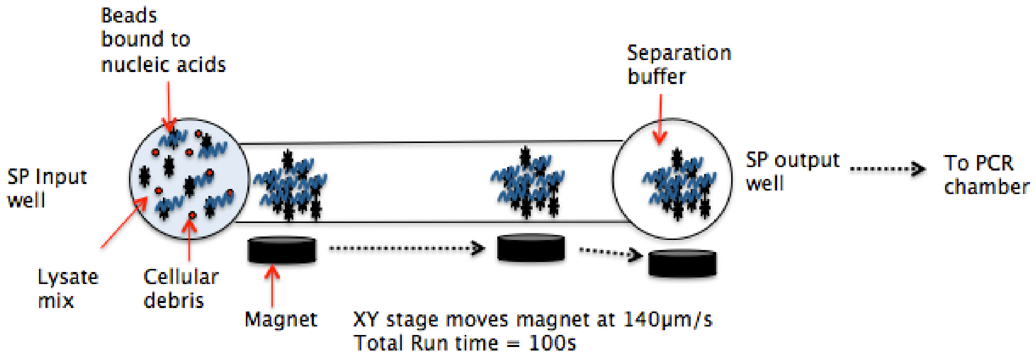

Figure 3.3: Illustration of on-chip bead-based sample preparation. Magnetic beads and attached DNA were separated from unwanted cellular debris using an automated XY stage. This approach is advantageous because it allows the extraction of DNA from raw clinical samples on a single microfluidic chip and instrument with demonstrated capability for DNA amplification and analysis

The advantage of on-chip SP is that it is automated and does not require a trained operator. While the conventional protocol for SP with Chargeswitch® beads takes place in a tube and is carried out by a trained operator. Our approach is performed in an on-chip channel and does not require manual intervention other than adding and remove sample from the chip with a pipette. This minimizes the training required and eliminates a lot of variability in the on-chip SP step[9]. Also, our protocol largely follows the manufacturer's instructions (see instruction manual) but it is simplified to ease on-chip implementation. First, the manufacturer calls for two additions of lysis buffer, one before and another after beads are added to the SP lysate. In tests conducted by collaborators at the MDG lab, one lysis step was found to be sufficient for efficient amplification of ß2m DNA from cheek cells. Also, as described earlier, the use of the manufacturer's elution buffer was replaced by releasing DNA from beads with PCR master mix. Again, this step reduced the complexity of DNA extraction without a significant loss in PCR product strength.

This proof of principle demonstration is part of ongoing efforts at the AML to integrate on-chip SP with amplification and analysis on the same microfluidic platform. While other demonstrations in the literature have been hampered by cost and complexity concerns, our proposed solution adapts a conventional DNA purification kit for use on a microfluidic chip in a large automated fashion. While there are still some manual handling steps required in this demonstration (i.e pipetting to add and remove samples from the chip), the separation of DNA from unwanted cellular debris is accomplished with an automated XY stage that eliminates variabilities and difficulties encountered during manual separation such as bead clumping as described in section 3.3.1. This was accomplished using a custom-built XY stage that was constructed for a total component cost of less than \$300 and integrated with a lab on chip instrument for DNA amplification and analysis with a total component cost of less than \$1200 (see appendix C).

3.4 Results and discussion

After performing on-chip SP and off-chip PCR in a thermocycler, I performed microchip CE in a commercial instrument (μTK, Micralyne Inc., Edmonton, AB). The microchips were designed for use with the instrument with standard CE settings of injection for 80s at 300V, followed by separation for 150s at 300V[10]. PCR was performed using the same recipe as provided in section 3.3.2. Complete protocols for off-chip PCR and off-chip CE are provided in "TTK SPPCRCE Protocol v1.02" in the supplementary information.

While positive controls with 50 ng/μL of ß2m genomic DNA gave positive outcomes, magnetic beads from on-chip SP did not give repeatable PCR products. In February 2009, although 6/6 ß2m positive controls (purified DNA in standard PCR mix) showed DNA peaks in electropherograms, only 1/5 on-chip SP samples gave similar positive results. The

---

[9] Ongoing work at the AML is exploring approaches to a completely hands-free on-chip SP implementation to further reduce variations associated with manual handling steps.

[10] Detailed descriptions of CE conditions are provided in Kaigala *et al.* (2008).

following hypotheses were considered as potential reasons for failure of the on-chip SP process.

1. **PCR inhibition by microchip surface**: I established that this was not a chip-related problem by performing the conventional tube-based SP. I prepared 11 tube-based SP samples, performed PCR in conventional thermocycler, and CE analysis in a μTK using the CE protocol provided in Kaigala *et al.* (2008). Only 3 out of 11 tube-based SP experiments showed a positive PCR outcome. This strongly suggests that failure of on-chip SP experiments was not due to a microchip problem, rather this suggests that a problem with reagents used during either SP, PCR, or CE was the culprit.

2. **PCR reagents**: To test which step of the reaction (SP, PCR, or CE) was responsible for the failed SP experiments, I performed off-chip PCR-CE experiments (skipping the SP step entirely) on conventional instruments. I obtained 14/14 positive PCR outcomes when I performed PCR with ß2m genomic DNA instead of purifying DNA from buccal cells. This indicated that there was a problem with the SP reagents or protocol that resulted in failures in both tube-based and on-chip SP experiments.

3. **Protocols and handling**: Because proper handling of reagents and adherence to protocols is essential to successful experiments, J.Lauzon, an experienced member of the MDG lab, repeated my experiments to ensure that there were no user-specific errors during the SP processes. No protocol or handling errors were observed and her on-chip SP experiments did not show any improvements.

4. **Degraded SP reagents**: The next hypothesis that was considered was that the SP reagents could be degraded. Of the SP reagents described in section 3.3.2, Proteinase K is the most susceptible to environmental factors and requires storage at -30˚C. In addition, it is prone to damage from multiple freeze-thaw cycles. While the manufacturer's documentation stated that Proteinase K should last for 6 months after first use, experience suggested that it degraded faster if it was repeatedly exposed to room temperature. I switched to a freshly ordered supply of Proteinase K (leaving all other reagents the same) and obtained 3 out of 3 positive PCR outcomes in on-chip SP experiments (with off-chip PCR/CE). Figure 3.4 shows an electropherogram from a successful on-chip SP experiment. This proved that degraded Proteinase K was the reason for failed on-chip SP experiments. I modified the SP protocol so that the stock of Proteinase K is split into 5 μL aliquots that are stored at -30˚C for one-time use only.

3.4.1 Contamination

Another problem encountered was the appearance of PCR product peaks in no-template controls. I was able to identify these peaks as unwanted ß2m DNA contaminating negative controls. In this section, I will describe efforts towards understanding this problem, eliminating hypotheses, and the eventual resolution of the contamination saga. This endeavour spanned several months because of the sporadic nature of the contamination problem.

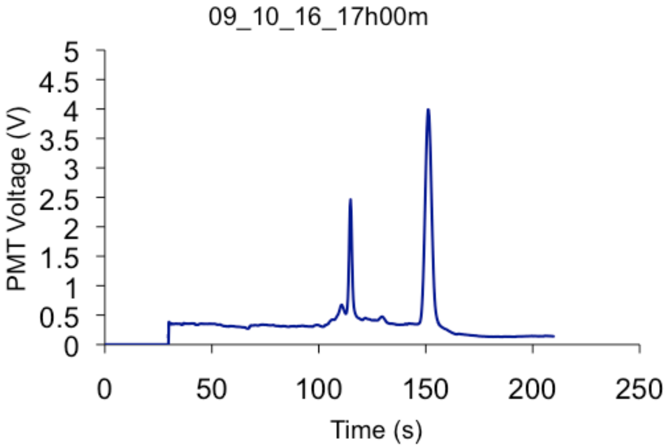

Figure 3.4: Electropherogram performed by the author using a commercial microchip-based system (μTK, Micralyne Inc., Edmonton, AB) showing primer and product peaks for ß2m DNA purified from human cheek cells. SP was performed on-chip followed by PCR in a thermocycler with conditions described in section 3.3.2. The protocol for on-chip CE is provided in the "TTK SPPCRCE v1.02" document in the supplementary information

Replicates of experiments were required to establish that I could obtain negative controls on a repeatable basis. In addition, this was a time-consuming process because of the time associated with ordering new stocks of primers and PCR reagents. I strongly recommend working with small, disposable aliquots of PCR reagents thereby exposing the main reagent stock to as little risk of contamination as possible.

Poor primer design can result in the formation of unwanted amplicons or primer-dimers. To test this hypothesis, a Basic Local Assignment Search Tool (BLAST) prediction (Karlin and Altschul, 1993) was performed to determine the expected size of the ß2m amplicon using the forward (GTACTCCAAAGATTCAGGTTTA) and reverse (CGGCAGGCATACTCATCTTTTT) primers designed for amplification of DNA samples from SP-PCR experiments [11]. The only amplicon obtained from the BLAST prediction with no base-pair mismatches with the primer sequence was the ß2m template in human DNA which is 235 bp long. The next gene most likely to be amplified was the zinc finger, matrin-type 4 (ZMAT4) gene which is 118bp long; however, there were 6 mismatches between the forward and reverse primers and the DNA sequence of the ZMAT4 template – indicating a smaller likelihood of this sequence being amplified.

Furthermore, CE analysis provided a size estimate for the PCR product in no-template controls. The amplicon from no-template controls appeared at the same position as the PCR product in the positive (i.e. "with template") controls (35 ± 5 s as seen in figures 3.4 and 3.7) . A CE experiment with a DNA size standard (ALFExpress, Amersham Biosciences,

---

[11] A BLAST search was performed using the primer design tool at the National Center for Biotechnology Information available at http://blast.ncbi.nlm.nih.gov/.

NJ, USA) estimated the size of the PCR product as 250 ± 20 bp (following the approach laid out in Kaigala *et al.* (2010)) which is in agreement with the 235 bp estimate from the BLAST search. Consequently, primer-dimers were ruled out as the reason for the unwanted peaks in no-template controls. This could potentially be confirmed by sequencing the PCR product from contaminated experiments, however, that was beyond the scope of this thesis.

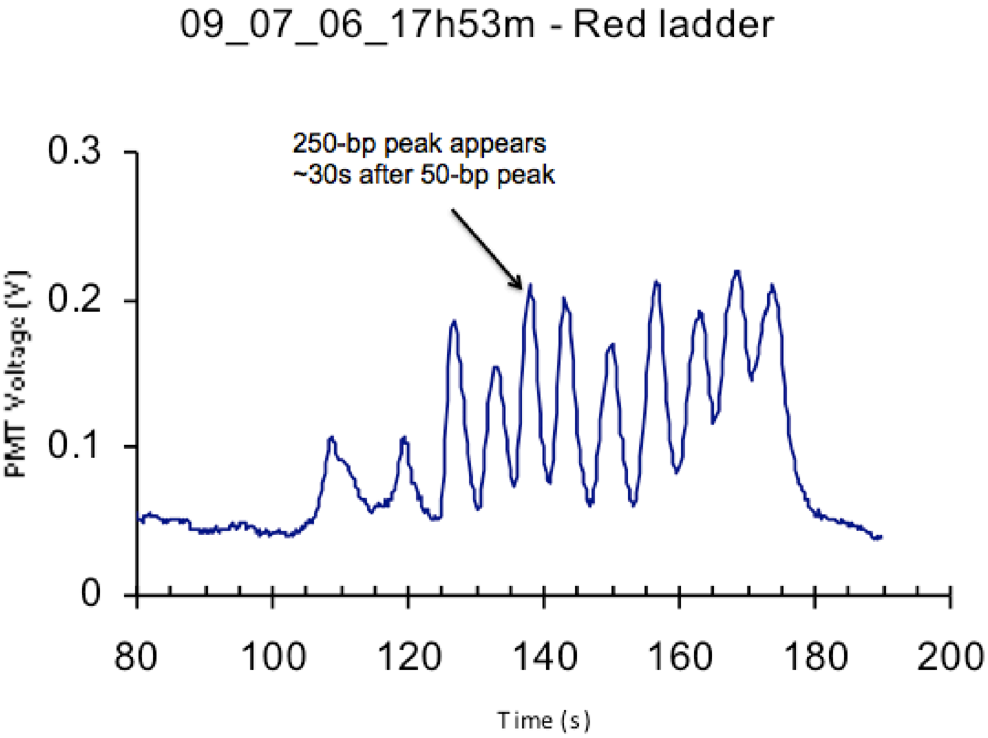

Figure 3.5: Electropherogram of DNA red ladder. Experiment was performed by M.Nielsen at the AML following protocols provided Kaigala *et al.* (2010). This experiment showed that a 250-bp DNA template should appear at approximately 30 ± 2 s (error in determining center of peak) away from the 50-bp peak (first one). This red ladder experiment was used to determine expected positions for PCR products and to size the DNA peak that appeared in CE experiments with no-template controls

.

To rule out handling and equipment-related errors, filtered pipette tips were used in all experiments. Microchips were also sealed off from air and kept in clean petri dishes handed only with gloves until it was time for on-chip experiments. In addition, biosafety hoods were used for all SP and PCR experiments to prevent cross-contamination. In addition, work spaces in the MDG lab were separated – with separate "no-template" hoods for negative controls. I also discarded my SP and PCR reagents and started with brand new aliquots for all my work. I repeated my SP and PCR no-template controls, deliberately changing specific variables to identify which of the reagents were tainted. I performed negative controls to determine if my SP and PCR reagents had been contaminated. I set up the following PCR reactions:

1. PCR mix with water added instead of DNA template – this would indicate contamination in my PCR reagents since this reaction does not involve SP reagents or the PCR-CE chip.
2. PCR mix with magnetic beads extracted from "dummy" tube-based SP mix that contained all SP reagents except buccal cells – in combination with experiment 1, this would indicate contamination in the SP reagents.
3. PCR mix with SP separation matrix added to the reaction instead of DNA – this would test the purity of the STW buffer which was the only reagent that the magnetic beads in the SP lysate come into contact with before entering the PCR mix.

These negative controls were accompanied by a positive control with ß2m genomic DNA to ensure that the PCR reagents were functional and could generate PCR products. Experiment 1 (water-only) showed only a primer peak in its electropherogram (see figure 3.6), suggesting that the PCR reagents were free from contamination. Also, experiment 2 showed only a primer peak suggesting that both my PCR and SP reagents were clean. Experiment 3 (separation matrix added to PCR reaction) showed only a primer peak suggesting that the SP separation matrix was clean. While these tube-based controls did not show contamination, they needed to be repeated to ensure that I had not just achieved clean results on a one-time basis, but those results could be consistently obtained when experiments were performed on-chip.

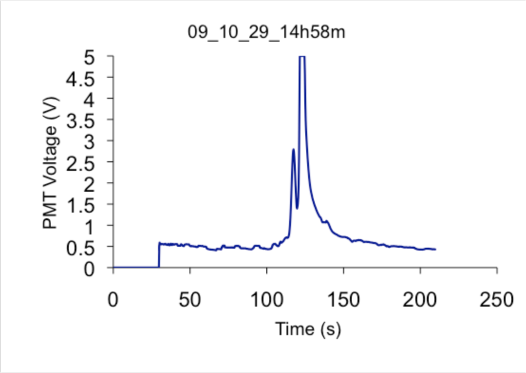

Figure 3.6: Electropherogram of no-template control with water added to PCR mix instead of DNA. Reaction was performed by the author following the protocol laid out in "TTK SPPCRCE v1.02" protocol in the supplementary information. Only a primer peak was observed in this control indicating that the PCR reagents were clean

The following day I repeated the negative controls described above to ensure that they were reproducible. I performed 2 experiments: an on-chip SP negative control (i.e. all SP reagents except buccal cells with separation of beads on-chip) as well as a tube-based no-template control with PCR reagents to check that PCR reagents were still clean. This time around the no-template control showed a small PCR product peak in addition to the primer peak (see figure 3.7) – indicating the presence of contaminants in the PCR reagents. Although this experiment was performed with exactly the same protocol as the clean runs in figure 3.6, there is obvious contamination in this experiment. In addition, the negative control where magnetic beads (without buccal cells) were extracted on-chip also showed a PCR product peak. This suggested that there might be contamination from the microchip surface in addition to contamination from the PCR reagents.

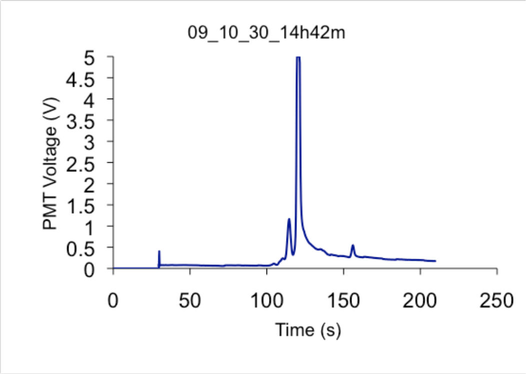

Figure 3.7: Electropherogram of tube-based no-template control with PCR reagents only. The experiment was a repeat run following the same protocol as in figure 3.6 and was carried out to check that I could consistently obtain clean negative controls. The presence of a PCR product peak (just after 150 s) in this no-template control indicates that the PCR reagents were contaminated

Since tube-based no-template controls with PCR reagents only showed PCR product peaks (see figure 3.7), I was able to rule out the microchip surface as the source of contamination observed in these experiments. This experiment suggested that the PCR reagents were contaminated with ß2m DNA in the MDG lab. I discarded my aliquots of PCR reagents and obtained new supply from a fresh stock. The presence of contamination even in conventional no-template controls suggested that there was a high level of contamination in the work area. To alleviate this problem, our research group embarked on an extensive lab cleanup – wiping down all bench surfaces with bleach, detergent, and alcohol in an effort to remove the contaminants. This was especially important because ß2m DNA is present in human skin cells; hence, even flakes of skin present in the lab environment could potentially lead to false positives.

In addition, we modified our protocols to require a no-template control and a positive control along with every experiment performed in the lab. Subsequently, I performed 12 more negative controls – of which 5 showed PCR product peaks in their electropherograms. To rule out user error or handling issues, other members of the MDG lab performed negative controls with ß2m DNA but they also saw PCR product peaks in their no-template controls. This suggested that wiping down the MDG lab was not sufficient to eliminate the ß2m contamination observed.

At this point, we explored another approach to purify experimental reagents. The PCR reaction mix (except UV-sensitive components like primers, Taq polymerase, and DNA template) was exposed to UV light in a biosafety hood for 5 minutes before each PCR run to denature any DNA contaminants inadvertently introduced to the reaction. After UV exposure, Taq polymerase, primers, and DNA template were added to the reaction mix. Although UV exposure reduced the contamination rate from 42% to 13%, it did not completely eliminate the problem. In addition, there were concerns about potential degradation resulting from exposing magnetic beads and other PCR reagents to UV light, so the UV exposure method was discontinued.

After repeated attempts to obtain consistently clean no-template controls in the MDG laboratory on the 6th floor of the electrical engineering building, Professor Backhouse decided that we should move to the Glerum lab in the Department of Medical Genetics. The rationale behind the move was that the continued failure to obtain clean negative controls at the MDG lab pointed to a baseline level of contamination in that lab that was not overcome despite extensive cleaning. Part of the reason for the failure to eliminate contamination in the MDG lab might be been overcrowding of that lab and also a delayed identification and response to the contamination problem. During my initial work at the MDG lab, I did not run no-template controls for every experiment – this might have allowed the contamination problem to grow unchecked for several months. It seemed a reasonable approach to start fresh with new reagents and protocols, in an environment where ß2m contamination was not already established. This suggestion was strengthened by the fact that initial no-template controls carried out in the Glerum lab came back clean, indicating that environmental and procedural problems were major factors contributing to the lingering contamination problem in the MDG lab.

At the Glerum lab, new protocols were instituted that required no-template controls along with every experiment. This was implemented to facilitate early detection and elimination of contamination and prevent a build-up of DNA in the work area. After establishing strict protocols and moving to a clean work environment, 3 on-chip SP experiments were performed followed by off-chip PCR in the thermocycler, and CE analysis in the μTK. In all 3 cases, strong positive outcomes were obtained with contamination-free no-template controls – suggesting that our on-chip SP protocols and infrastructure operated well on a standalone basis. Furthermore, all future on-chip SP experiments were accompanied by no-template controls allowing the early detection of contamination. With this new approach and in the new environment, we were able to overcome the ß2m contamination problem and demonstrate successful on-chip SP.

Chapters 4 will describe the on-chip real time PCR module while chapter 6 will discuss the integration of on-chip SP and PCR subunits. Standalone SP on-chip showed strong PCR product peaks for all 3 on-chip SP runs as shown in figure . In chapter 6, I estimate the strength of the PCR products obtained during on-chip SP and provide potential reasons for the variability observed.

3.5 Closing remarks

This chapter discussed the development of an automated SP module for DNA purification on the TTK. There are several different approaches to on-chip DNA purification in the literature (Chen *et al.*, 2007a, Dineva *et al.*, 2007, Kim *et al.*, 2009). Among these, the use of functionalized magnetic beads is advantageous because it is suitable for concentration of samples, provides large surface area for DNA extraction, and can allow for specific DNA binding mechanisms that are compatible with downstream reactions (Lien *et al.*, 2009, Liu *et al.*, 2011, Ramadan and Gijs, 2011). I initially set out to perform dynamic DNA purification by moving Chargeswitch® magnetic beads away from cell lysate using an automated XY stage that was designed during my final year project while I was an undergraduate student. At the time, the novelty of the system would lie in its use of dynamic bead capture to improve DNA purification efficiency, and in the automated combination of DNA purification, amplification, and analysis once a lysed cell sample is loaded onto the microchip. However, there have been recent demonstrations of dynamic magnetic bead-based SP from raw clinical samples (Duarte *et al.*, 2010, Ramadan and Gijs, 2011) as well as publications in which DNA is extracted from buccal cells using the same Chargeswitch® magnetic beads employed in this thesis (Hopwood *et al.*, 2010, Hurth *et al.*, 2010). As such, future work related to dynamic DNA purification with magnetic beads should be focused on eliminating the reliance on bulky and expensive components (Ramadan and Gijs, 2011) and reducing overall reaction time to allow for true point of care applications (Hopwood *et al.*, 2010, Hurth *et al.*, 2010).

I described the AML's approach to on-chip SP using a custom-built XY stage and a separation channel on a microchip. For a total component cost of less than $300, our laboratory implemented on-chip DNA extraction using Chargeswitch® magnetic beads. Lysed samples were added and removed from the microchip using a pipette. Afterwards, a central microcontroller directed the separation of DNA from unwanted cellular debris in an automated manner using a permanent magnet attached to a custom-built XY stage. The development of the X-Y stage began while I was an undergraduate student. I integrated the stage with the TTK and developed protocols to reduce bead clumping and ensure smooth transfer of beads and DNA across the separation channel. This involved positioning the permanent magnet outside entrance of SP input well to reduce bead clumping and writing firmware in C++ to time magnet motion and ensure that beads were transferred from across the separation channel. The SP module was tested on a standalone basis by performing on-chip SP, followed by PCR in a conventional thermocycler and CE on a commercial microchip instrument (μTK). This approach was taken to ensure that SP performed well independently of other on-chip processes implemented on the TTK (i.e. real time PCR and MCA). Chapter 6 considers the integration of on-chip SP with real time PCR and melting curve analysis.

During this endeavour, I encountered problems including the contamination of no-template controls. Initially, 42% of the no-template controls resulted in false positives. CE analysis revealed that the contaminant was the same size as the expected ß2m PCR product suggesting that the false positives were not due to primer-dimers, rather they were due to the presence of ß2m DNA in the work environment. The false positives appeared even in tube-based experiments indicating that the problem was not specific to on-chip work. Attempts were made to resolve the contamination problem by a thorough cleanup of the MDG lab, segregation of work areas to create "DNA-free" zones, and exposure of PCR reagents to UV light. While these efforts reduced the rate of false positives to 13%, they did not eliminate the problem. This led to the conclusion that ß2m DNA (ubiquitous in human skin cells) was abundant in our work environment and the failure to detect and address the contamination problem early had allowed the contamination problem to become entrenched in the MDG lab. The contamination problem was eradicated by moving to the Glerum lab, where there was no history of ß2m work and strict protocols were instituted to ensure early detection of contamination. After establishing new protocols, 3 on-chip SP experiments were performed followed by off-chip PCR in the thermocycler, and CE analysis in the μTK. For all 3 runs, strong positive outcomes were obtained after CE analysis with no trace of contamination in the no-template controls. This validated the design of the SP module on a standalone basis.

The SP module described in this chapter overcomes the cost challenge since it does not rely heavily on expensive instrumentation (see appendix C for a breakdown of component costs. In addition, the separation of magnetic beads from cellular debris is automated and only requires a user to add and remove the sample. While there are still manual handling steps (i.e. chemical cell lysis and pipetting), this proof of principle demonstration showed an inexpensive method for purifying DNA from raw clinical samples. Future work at the AML will explore approaches to transfer chemical cell lysis onto the microchip and reduce the complexity and cost of the SP module by using a single servo motor instead of an XY stage.

The next step in the development of the LOC system for point of care analysis was to combine on-chip SP and on-chip real time PCR. Chapter 4 describes the development and testing of the real time PCR module.

CHAPTER 4

Real time PCR

Real time PCR is a variation on traditional PCR that permits real-time monitoring of DNA amplification. Data gathered during real time PCR (collected as an amplification curve) allows us to make inferences about the starting concentration of DNA and PCR reaction efficiency – important parameters in some clinical applications (Kubista *et al.*, 2006).

This chapter describes the re-design of the TTK to facilitate the implementation of on-chip real time PCR. I played a central role in the hardware, firmware, and software design for real time PCR thermal regulation and optical detection on the TTK. Furthermore, I designed algorithms and scripts to analyze real time PCR data, and interpret our results.

4.1 Overview of on-chip real time PCR systems

To provide background and rationale behind our real time PCR design choices, I will begin with a brief overview of on-chip real time PCR systems. This is a large and diverse field, as such, I will only discuss state of the art advancements.

Most bench-top thermocyclers use electrically heated metal plates to carry out PCR reactions in plastic tubes. This macroscale setup has large thermal mass leading to slow heating and cooling rates and corresponding long reaction times (hours). On-chip PCR reduces thermal mass by using highly conductive materials such as silicon and glass. This results in speedy PCR reactions that promote the adaptation of nucleic acid assays in point of care settings (Zhang *et al.*, 2006). Furthermore, on-chip solutions require reduced sample & reagent use leading to cost savings. Also, on-chip PCR systems can be readily integrated with real time amplification monitoring, and post-PCR melting curve analysis can also be easily automated in a microfluidic system.

There are 2 main paradigms in the design of on-chip PCR systems. In time-domain architectures, the PCR reaction mix is heated through required temperatures in the stationary chamber. This can be modelled after bench-top systems with Peltier plates for heating or use other heating methods to increase ramp rate and reduce reaction time. Meanwhile, in space-domain architectures PCR mix is moved around to different temperature zones. This includes “continuous flow” systems where liquid is moved by pumping along a channel as well as “droplet-based” systems where fluid handling is carried out in droplet form. An advantage of droplet-based systems is that it helps to automate fluid handling and reduce microfabrication concerns in continuous flow systems by eliminating the need for long channels (Pipper *et al.*, 2008). Space-domain systems can allow for faster reactions since the temperature zones are already at stable temperatures; however, they can entail more complicated microfabrication and fluid handling demands (Zhang *et al.*, 2006).

On-chip real-time PCR systems combine thermal cycling with optical detection on a microfluidic platform. Stationary on-chip PCR systems can be easily modified to perform real time PCR by incorporating optical detection systems for real time amplification monitoring. However, equipping continuous flow systems for real time PCR is more challenging since the PCR reaction is spread over large area making it difficult to observe the PCR reaction. However, droplet systems can often be manipulated readily and permit relatively easy integration with real time PCR optical detection infrastructure (Chen *et al.*, 2007a, Pipper *et al.*, 2007).

Northrup et al were the first to perform real time PCR on a LOC platform. They modelled their system after conventional real-time PCR machines. They designed a silicon microchip for rapid heating and cooling with microfabricated windows to allow optical detection. The microchip and supporting electronics and hardware requirements fit into a briefcase for portable on-chip diagnosis of up to 20 copies per reaction of HIV virus (with a CT value of ~35). Their biological assay employed specific Taqman probes to bind to the DNA sample of interest; as a result, they did not perform melting curve analysis (Northrup *et al.*, 1998). While they obtained fast reaction times and sensitive results, further miniaturization than a briefcase-sized system is desirable for true portability and low-cost. Furthermore, while silicon is easy to micro-machine, it is opaque to optical detection and requires surface passivation to prevent reaction inhibition (Cho *et al.*, 2006)

In a state of the art demonstration, Cho et al presented a portable microfluidic system for the clinical diagnosis of Hepatitis B virus using on-chip real time PCR and MCA (Cho *et al.*, 2006). Their microfluidic system was commercialized as the Samsung GenSpector® TMC1000. They designed a silicon-glass microchip with 1μL PCR volume for rapid reactions at temperature ramp rates up to 20°C/s. The authors used disposable glass chips to hold PCR reagents and a permanent silicon chip for heating. Using this approach, they achieved a temperature uniformity of ± 0.5°C during a 25 min real time PCR reaction. Their optical detection module was made up of an LED light source and a CCD camera for inexpensive and portable fluorescence monitoring. Clinical testing of their instrument showed excellent reproducibility of on-chip results with mean Ct values of 19.28 ± 0.09 cycles over 90 different samples with sensitivity approaching 100 copies per chamber. However, because of the use of permanent silicon heating plate, the system is still quite bulky and is more representative of a bench-top system. The authors also acknowledge that the system requires more miniaturization to be a truly portable and inexpensive lab on a chip solution (Cho *et al.*, 2006).

Pipper *et al.* (2008) describe a droplet-based real time PCR microchip. Their system utilized magnetic bead based DNA extraction and pre-concentration followed by on-chip real time PCR and MCA for the rapid diagnosis of bird flu in less than 30 mins (Pipper *et al.*, 2008). However, this instrument relied on bulky and expensive optical detection equipment i.e. mercury lamp for illumination, optical microscope and photomultiplier tube for detection, and oscilloscope for recording fluorescence data.

To curb the dependence on bulky equipment, the same research group presented a compact and inexpensive optical detection system (Novak *et al.*, 2007). This optical detection instrument is modelled after a DVD head and makes use of LED illumination and photodiode detection. In addition, it employs a lock-in amplifier for noise-free operation in ambient light. This portable optical detection system was characterized with fluorescein dye and had a limit of detection (LOD) of 1.96 nM of fluorescein (comparable to conventional real-time PCR instruments). However, the authors do not provide data from clinical applications of this compact optical detection module.

Lee's research group present a state of the art integrated instrument for on-chip sample preparation followed by real time PCR amplification and analysis (Lien *et al.*, 2009). Starting with saliva samples, they performed automated cell lysis, DNA extraction, and real-time PCR on the same microfluidic chip in less than an hour. The microchip consisted of copper resistive micro-coils that are actuated using DC electric fields. Samples are pumped into the DNA extraction chamber with on-board pneumatic micro-pumps. Extracted DNA was amplified by on-chip real time PCR with specific Taqman probes. The authors successfully detected the presence of deletion mutations in human cells with a limit of detection of 12 pg/μL. This is comparable performance to conventional off-chip extraction and amplification procedures (Lien *et al.*, 2009). While this device automates and integrates multiple diagnostic processes (extraction, real time amplification, and detection), its high cost and limited portability restrict its application in point of care settings. In particular, this demonstration relies on a photomultiplier tube (PMT) and a mercury lamp for optical detection – both bulky and expensive modules.

4.1.1 Limitations of state of the art systems

Although on-chip real time PCR systems like those demonstrated by Lien *et al.* (2009) and Pipper *et al.* (2008) can provide comparable sensitivity to conventional real time PCR instruments, their widespread adoption is limited by a reliance on bulky and expensive optical detection infrastructure such as mercury lamps, lasers, fluorescence microscopes, and photomultiplier tubes (Chen *et al.*, 2007a, Kaigala *et al.*, 2010, Yager *et al.*, 2006). **There is a strong need for a portable and inexpensive LOC system with a scalable and integrated optical detection module.**

4.2 Design of initial approach

With the challenges facing LOCs in mind, the TTK was designed to be a portable lab on a chip system that is independent of large and expensive conventional equipment (Kaigala *et al.*, 2008). To implement on-chip real time PCR, we needed to re-design and test the following system modules:

1. thermal regulation
2. optical detection

4.2.1 Thermal regulation

To check the performance of the TTK's temperature control algorithm and to ensure accuracy of chip calibration data, the temperature of the PCR chamber needed to be monitored. Temperature measurement on microfluidic systems is a diverse and challenging field (Liu *et al.*, 2002). There are different approaches to temperature regulation on lab on a chip platforms. Although on-chip PCR systems have the potential for faster and more uniform heating than their conventional off-chip counterparts, precise design, modelling, and testing are required to take advantage of these benefits (Chaudhari *et al.*, 1998). This means that there is a need for accurate temperature measurement technologies on microfluidic platforms.

Recent reviews by Zhang *et al.* (2006) and Samy *et al.* (2008) describe state of the art approaches to temperature measurement in lab on a chip devices. For example, one method for temperature measurement in lab on a chip devices is to insert a thermocouple into the on-chip PCR chamber; however, inserting metal thermocouples can drastically alter the temperature distribution inside the PCR chamber. Another approach is to use microfabricated thermocouple junctions deposited on the microchip for accurate temperature measurement without significant systematic shifts. But microfabricated sensors often have complex fabrication demands and the deposition of metal sensors inside the PCR chamber can inhibit PCR reactions. Infrared thermometry is another on-chip thermometry technique that provides the surface temperature profile of a reaction mixture in an on-chip PCR chamber. This has limitations when the whole temperature profile (instead of just the surface temperature) of the reaction mixture is required (Chaudhari *et al.*, 1998).

In our TTK instruments, thermochromic liquid crystals (TLCs) are used to measure PCR chamber temperature. TLCs were chosen because of their accuracy, precision (±1.5°C bandwidth), and ease of use (chips can be filled with TLCs suspended in liquid and operated as if they were filled with PCR reaction mixture instead). Much of the background on TLC temperature measurement is provided in past work from the AML (Hoang *et al.*, 2008) but I will summarize the key details here for completeness. Thermochromic liquid crystals (TLCs) are organic cholesterol-based compounds that have temperature dependent optical behaviour. This results in apparent colour changes as the temperature of the PCR reaction chamber is varied (Chaudhari *et al.*, 1998). The temperature of the TLCs can be quantified by imaging the crystals with a camera or spectrometer and measuring the "hue" or the shade of the colour of the TLCs. The use of TLCs for on-chip measurements is further simplified by the fact that they can be dispersed in liquids and loaded into PCR chambers to measure the temperature of on-chip PCR systems using the exact same settings as a real on-chip PCR reaction.

PCR heating is implemented in the AML's microchips by supplying current to a platinum heating element which surrounds the PCR chamber. To get a desired PCR chamber temperature ($T_{chamber}$), a known current is applied to the heater. The current supplied to the heater is calculated using resistive properties (thermal coefficient of resistance and resistance at 0˚C) of the heating element. These chip parameters are measured when the microchip is manufactured (as described in section 4.2.1).

Temperature calibration

The PCR chamber temperature was not measured directly rather its value is inferred using the empirical relationship between heater and chamber temperatures. In order to accurately measure heater temperature, each microchip undergoes a temperature calibration process wherein its thermal properties (temperature coefficient of resistance and resistance at 0˚C) are determined. First, all bottom plates of microchips (containing the heating element) are annealed at 200˚C at atmospheric pressure for 2 hours. Annealing ensures that thermal properties of the platinum heating element will not change during regular use (the TTK firmware sets a temperature safety limit of 170˚C for the heating element). Annealing is performed according to protocol 11P[1] in the AML's microfabrication protocol binder. I will summarize the details here for completeness.

The thermal properties of microchip bottom plates are measured by immersing the microchip in a water bath (HAAKE Phoenix II PI circulator, Thermo Electron Corp., Waltham, MA, USA) and setting the temperature to 25˚C, 40˚C, 60˚C, 70˚C, 80˚C, and again at 25˚C (to check for hysteresis). The resistance of the heating element was measured 3 times at each of these temperatures using a Fluke 179 multimeter (Fluke corporation, Ontario, Canada). A least squares regression was then used to estimate the temperature coefficient of resistance, the resistance at 0˚C, as well as the uncertainties in those values. The acceptance criteria for microchips to pass the calibration was set as a maximum uncertainty in temperature of ± 2˚C at 170˚C with a 99% confidence interval. The calculations for error propagations in heater temperature measurements were completed by Dr. R. Johnstone and summarized in his report titled "Error in Heater Temperature Measurements using TTKs" that is provided in the supplementary information CD.

On the TTK, knowledge of the heater's thermal properties and the current supplied to the heater can be used to estimate the heater temperature. The heater is placed in one of the arms of a wheatstone bridge, while the other arm contains a variable resistor. The use of a variable resistor allows the user to balance the bridge (so that the current flowing between the branches is zero) prior to the start of each run. This allows the heater resistance to be separated into 2 components – its value when the bridge was zeroed at the start of the

---

[1] Resistive element annealing and calibration, version 2.1

experiment, and the change in heater resistance corresponding to the current supplied to the heater.

Step by step derivations of the relationship between the change in heater resistance and heater temperature are provided in Dr. R. Johnstone's "Error in Heater Temperature Measurements using TTKs" report. To summarize, the heater temperature is given by equation 4.1.

$$T_{\mathrm{h}} = T_{\text{heat sink}} + \frac{\Delta R_{\mathrm{h}}}{m} \tag{4.1}$$

where T_h is the heater temperature, $T_{\text{heat sink}}$ is the heat sink temperature, ΔR_h is the change in heater temperature, and m is the temperature coefficient of resistance obtained as the slope of microchip calibration experiments in the water bath described in protocol 11P in the AML microfabrication binder.

An empirical relationship between heater and chamber temperatures was obtained by measuring the heater temperature required to obtain colour changes in TLC-filled microchips. This empirical T_c-T_h relationship was used to predict future conversions between heater and chamber temperature. S. Poshtiban performed the initial experiments to determine an empirical relationship between heater and chamber temperatures. Her procedure and results are summarized in the "Thermal Calibration Report" provided in the supplementary information CD. I will summarize the key points here.

Thermochromic liquid crystals with transition temperatures of 58.6˚C, 70.6˚C, and 93.6˚C were obtained (R58C3W, R70C3W, R93C3W, Hallcrest, Glenview, IL, USA). Microchips were filled with the crystals and bonded as described in S. Poshtiban's "TLC chip preparation protocol" also provided in the supplementary information. 3 microchips were prepared with the 93.6˚C crystals and the 70.6˚C crystals respectively, while 2 microchips were filled with the 58.6˚C crystals. The heater temperature was set manually until the TLC crystals were observed to turn green – with observations carried out in a dark room under light illumination from a cold light source (L-150A; Radiant Optronics, Singapore) placed ~10cm above the microchip. The room temperature was fixed to 22˚C in the firmware. Using the data gathered from all 8 microchips, an experimental relationship between the heater and chamber temperatures was obtained as shown in equation 4.2.

$$T_{\mathrm{c}} = 2.15T_{\mathrm{h}} - 37.95[^{\circ}C] \tag{4.2}$$

where T_c is PCR chamber temperature and T_h is heater temperature.

Temperature variations

Prior to on-chip real time PCR experiments, TLC measurements on the TTK were repeated to measure the variation in PCR chamber temperature. PCR reactions are temperature sen-

Table 4.1: Manufacturer's specifications for expected TLC colour transitions

TLC	Start of green (˚C)	Maximum green (˚C)
R58C3W	58.6	59.7
R70C3W	70.6	71.7
R93C3W	93.6	94.7

sitive, and significant variations in annealing, extension, or denaturation temperatures may result in anomalies such as the formation of primer dimers or the inactive of Taq polymerase enzyme – leading to the failure of microchip PCR experiments (Zhang *et al.*, 2006). Thermochromic liquid crystals (TLCs) were used to measure the static PCR chamber temperature[2].

I used PCR-CE-4 chips that were filled with TLC crystals by S. Poshtiban according to her April 2010 AML protocol [3]. Observations were made by eye by A.Olanrewaju, F.Hejazi and S.Groendahl using a cold light source (L-150A; Radiant Optronics, Singapore). The light source was placed ~10cm above the PCR chamber of the chip and was mounted on a light microscope (SPZT40; Carton Optical, Canada) to keep it vertically above the chip. Regular fluorescent room lighting in the AML served as the background[4].

Chip parameters used to determine current settings for the thin film heater were the resistance, R, measured with a Fluke 179 multimeter and the temperature coefficient of resistance (TCR) obtained during microfabrication described in section 4.2.1. Theoretical information on the TLCs used was obtained from Hoang *et al.* (2008) and are summarized in table 4.1. Two metrics for TLC temperature transition are provided by the manufacturer, namely:

- "Start of green" – temperature at which a green fringe first appears and covers less than 10% of the PCR chamber.
- "Maximum green" – temperature at which a strong green colour first fills greater than 90% of the PCR chamber.

I measured PCR chamber temperature by entering desired test temperatures into the TTK GUI and holding the temperature constant for 10 s. These measurements were carried out using the same microchips that were used by S. Poshtiban. The objective of these measurements was to determine the variation in PCR temperatures on the TTK. The full protocol for measuring static TTK temperature with TLCs is provided in the "Static TTK temperature measurement with TLC chips" report provided in the supplementary information. For the microchip filled with 58.6˚C-rated TLC crystals, the PCR chamber temperature

---

[2] "static" here refers to the fact that we allow sufficient time. Dr.R. Johnstone empirically determined an open-loop time constant of 2.5 seconds for the TTK. Four time constants (10 seconds) were allowed for system equilibration before measuring the temperature with TLCs

[3] See "TLC chip preparation protocol" by S. Poshtiban in the supplementary information CD for details on how the chips were made and stored

[4] The full procedure for static TLC temperature measurements is provided in the"Static TTK temperature measurement with TLC" protocol in the supplementary CD that accompanies this thesis.

was set to a temperature range of 58 to 64°C to determine the precise temperature at which the TLC changed colour. Similarly, for the 70.6°C TLCs the temperature was varied from 70°C to 76°C, and for the 93.6°C TLCs the temperature was varied from 90°C to 95°C.

The temperature at which the start of green was observed was determined by eye. Although deciding on the colour transition was a subjective exercise, attempts were made to limit systematic error by requiring that at least 2 observers agree on the colour change. I estimated an error of ± 1°C in visual observations of TLC temperature based on the difficult in determining which shade of green was darkest.

TLC measurements indicated that the TTK (Angelina) showed a start of green transition of 62.7 ± 1.0 °C for the 58.6°C TLCs, 74.0 ± 1.0 °C for the 70.6°C TLCs, and 91.7 ± 1.0 °C for the 93.6 °C TLCs. These results indicated that the TTK was approximately 4°C colder than the manufacturer-specified TLC transition temperature at 58°C, 3°C colder at 70°C, and 2°C warmer at 94°C. This data suggested that even with the same microchips, the TTK did not provide the expected temperature behaviour specified by our empirically obtained relationship between heater and chamber temperatures.

These static TTK temperature measurements were used to provide recommendations for changes to be made to ensure repeatable thermal regulation on the TTK. Some of the recommendations put forward partly as a result of these measurements were:

- account for heat sink temperature fluctuations when calculating heater temperature
- correct for systematic errors associated with observing TLC colour transition by eye
- measure air gaps in TLC chips used to calibrate system
- measure microchip thickness and alignment variations

Festival of Calibrations

Because of the complexity of the tasks involved in the thermal calibration of our systems (i.e. control of parameters from microfabrication to biochemical protocols) a team at the AML was convened to address this endeavour from start to finish - this effort was dubbed the "Festival of Calibrations". The team comprised of M. Behnam, S. Groendahl, and J. Martinez-Quijada, under the supervision of Dr. Backhouse. Their findings will be described in detail elsewhere[5], but the sections related to on-chip real time PCR are summarized here for clarity and completeness. While I did not participate in the festival of calibrations, I followed the progress and changes made so that I could understand its impact on real time PCR work.

During the festival of calibrations, the following hypotheses were explored and tested as potential sources of temperature inaccuracy and non-uniformity in the TTK.

1. **Recording TLC measurements by eye:** One of the first warning signs indicating poor thermal calibration was that the measured PCR chamber temperature varied based on

---

[5] A manuscript summarizing the procedures and results of the "The Festival of Calibrations" is currently in preparation.

the choice of TLC-filled microchips. One of the sources of this discrepancy was user-dependent colour observations by eye. The TLCs change colour from grey to green and then to red as they pass through their transition temperature set points. In practice, we estimated a ± 1˚C variation in TLC temperature when transition temperatures are recorded by different users.

During the festival of calibrations, our research group switched from user-dependent observations by eye to automated measurements with a spectrometer. The spectrometer records the spectrum of the TLC-filled chip as shown in figure 4.1. The TLC transition temperature was defined as the temperature which provides the maximum ratio of the red spectral peak to green spectral peak. This ratio gave TLC transition temperatures that agreed with the manufacturer's specifications to within ± 0.5˚C when heating was performed on the water bath. This approach provided repeatable and user-independent measurements of PCR chamber temperature on the TTK.

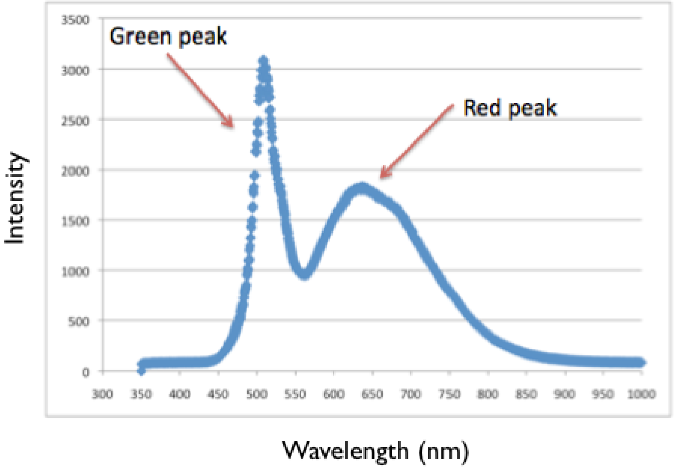

Figure 4.1: Sample spectrum obtained from TLC-filled microchip during festival of calibrations. TLC transition temperature was defined as the point at which the maximum ratio of red to green spectral peaks was obtained. This method provided repeatable and user-independent TLC temperature determinations that agreed with the manufacturer specifications when heating was carried out in the water bath. This spectral image was captured by A.Olanrewaju using a microchip (chip #0811C20) filled with 58.6˚C-rated TLCs at a temperature setting of 55˚C to show what the spectrum looks like.

2. **Microchip quality control:** While the use of a spectrometer eliminated some of the systematic error in TLC temperature measurement, there were still residual variations in PCR chamber temperature across different PCR-4 microchips that were filled with TLCs. Some of this variation was attributed to the need for stricter quality control during microchip fabrication and characterization. Prior to each on-chip PCR run, the resistance of the heating element of the microchip was recorded using a Fluke 179 multimeter as described in "TTK SPPCRCE v1.02" protocol in the supplementary

information. Measurements indicated that some microchips gave different resistance measurements from their initial water bath calibrations – suggesting that the chips' resistance properties had changed. This was likely due to physical defects that arose as a result of scratching the heater pad during use or imperfections in the heater ring that could be observed under a microscope.

Our initial approach did not account for changes in chip properties. To address these concerns, microfabrication techniques were re-evaluated in an effort to minimize damage to chips. All microchips were also inspected before and after experiments to identify chips with noticeable imperfections. As part of stricter quality control methods, all the infrastructure (water bath, DMMs) used to measure chip parameters (R & TCR) were calibrated against their data sheets to make sure they were in proper working order. The data obtained from each device was used as a correction factor in temperature measurements. Furthermore, the thermal properties of each chip were checked before and after microfabrication and on-chip operation in the water bath as described in section 4.2.1. If variations that fell outside a statistically-determined confidence interval were observed then the chip did not pass quality control and was not used for future experiments.

3. **Differences between thermal properties of TLCs and PCR mix:** In addition, inspection of TLC chips with an optical microscope showed that the thermochromic liquid crystals did not completely fill the 90-μm PCR chamber. The TLC chips were suspended in water and left to dry inside the PCR chamber (as described in "TLC chip preparation protocol" by S. Poshtiban). This reduced their overall volume, and resulted in the formation of an air gap inside the PCR chamber. The presence of an air gap in the PCR chamber significantly altered the temperature distribution.

   J.Martinez-Quijada modelled this effect with 3-dimensional finite element analysis[6]. These simulations suggested that the presence of an air gap inside the PCR chamber contributed to the difference between theoretical and experimental PCR chamber temperatures.

   In addition, because the thermal properties of TLCs are different from those of water and PCR reaction mix, it was necessary to simulate the PCR chamber temperature of a TLC-filled chip and compare that with a chamber filled with PCR cocktail. To this end, J.Martinez-Quijada developed a three-dimensional finite element model of the microchip and simulated temperatures when the PCR chamber is filled with different materials of interest. Consequently, temperature measurements were corrected for the thickness and thermal properties of TLCs in the PCR chamber – leading to more accurate determination of microchip temperature.

4. **Heat sink temperature variation:** Another source of variation in PCR chamber temperature was fluctuations in room temperature during experiments. At the time, the

---

[6] This is summarized in J.Martinez-Quijada's April 2010 report "Effect of Filling the PCR chamber in PCR-4 with Water, Oil, TLC and Air on TLC temperature measurements – Steady State Analysis".

firmware (see heater.c file in firmware version 220 folder in supplementary information) set a fixed room temperature value of 22°C for all experiments. However, there were noticeable temperature variations during on-chip PCR runs. Some of these variations were attributed to changes in heat sink temperature during on-chip PCR reactions. Temperature measurements with the mercury thermometer on the wall of the MDG lab in room 6-006 of the electrical engineering building showed that the room temperature varied by up to 3°C during a typical on-chip PCR reaction. This new insight suggested that the need to update equation 4.2 so that it depended not only on heater temperature but also on heat sink temperature. This new relationship between heater, chamber, and heatsink temperatures was obtained by setting desired heater temperatures, measuring PCR chamber temperature with well-characterized TLC chips, and recording heatsink temperature with calibrated thermocouples. From this new data set, a new empirically-derived equation was obtained in the form:

$$T_{\text{chamber}} = aT_{\text{heater}} + bT_{\text{heatsink}} \tag{4.3}$$

where a and b were constants obtained experimentally from a linear fit of T_{chamber}, T_{heater}, and T_{heatsink} and verified with FEM simulations (see chapter 5). This updated formula provided accurate readings of PCR chamber temperature without the need for an invasive sensor into the PCR chamber. In addition, the system was now capable of correcting for changes in ambient temperature during operation.

The result of our updated system characterization and calibration protocols was a robust system modelled by 3-dimensional finite element methods and verified by accurate TLC thermometry. We now have microchips with accurately known resistance properties and a system that can compensate for variations in chip thickness, heat sink temperature, & microfabrication changes. Consequently, we were able to proceed with on-chip real time PCR and MCA experiments with this robust and reliable system.

4.2.2 Optical detection

The original design for optical detection in our real time PCR-MCA instrument is illustrated in figure 4.3. For real time optical detection, a 340 mW royal blue LED (LXHL-LR3C; Quadica developments Inc., Ontario, Canada) and a CCD camera (Meade deep sky imager pro monochrome; Meade Instruments Corporation, Irvine, CA, USA) are used. The 455 nm wavelength LED provides illumination in the absorption range of the intercalating dye (LCgreen plus®; Idaho Tech., USA) used for real time PCR and MCA.

We chose LCgreen plus intercalating dye because it is a "saturation" dye designed for high resolution melting curve analysis and can detect the presence of DNA heteroduplexes that are often not observed with other dyes (Wittwer *et al.*, 2003). The optimal absorption and emission ranges for LCgreen plus® are 440-470 nm and 500-520 nm respectively [7]. Consequently, we designed our optical illumination and detection infrastructure to meet these wavelength requirements. As shown in figure 4.2, the excitation and emission filters were chosen to match LCgreen's optimal absorption and emission wavelengths.

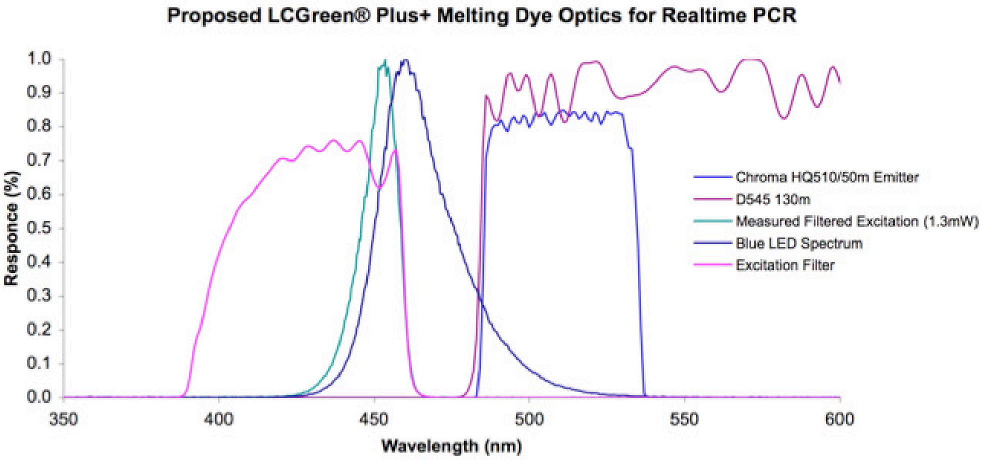

Figure 4.2: Filter design appropriate for detection of LCGreen plus® melting dye. The excitation filter was chosen so that it overlapped with the absorption range of LCgreen while the emission filter was chosen to match the dye's emission wavelengths. Spectra for the Chroma filters were downloaded from the company's webpage at www.chroma.com and are provided in the supplementary information CD, while the spectrum of the LED was measured using Ocean Optics spectrometer with LS-1 tungsten halogen light source (Ocean Optics, FL, USA).

Light from the LED is transferred into a 1-mm plastic optical fiber (Optical Grade Plastic Light Guide, Edmund Optics, NJ, USA) using a custom-built plastic fitting that is glued directly on top of the LED. Because LED illumination is dispersed over a 140° viewing angle, only the small fraction of light that enters the vertically-mounted fibre optic cable is collected. Consequently, there is a significant drop in optical power when the fibre optic cable is attached to the LED. Measurements with a handheld optical power meter (T54-018, Edmund Optics, NJ, USA) indicate that only 3mW of power is propagated by the fibre optic cable. This is a major source of sensitivity loss and improvements to this setup will be explored in future work (see chapter 7.2).

The fiber optic cable carrying LED light is then fed into an excitation filter assembly. This filter assembly consists of a bandpass excitation filter (D425/60x; Chroma Technology Corp., Bellow Falls, VT, USA) and 2 ball lenses. The excitation filter restricts the wavelength of LED illumination to 395–455 nm while the ball lenses focus light entering and exiting the filter. As a result of attenuation and scattering losses from non-ideal behaviour of the filter and lenses, the optical power of light in the fiber optic cable measured after the filter assembly is down to 500 μW. At this stage, the optical fibre is pressed against the side of the microfluidic chip and held in place using a custom-built brass holder.

---

[7] The manufacturer does not provide the full spectrum of LCgreen plus.

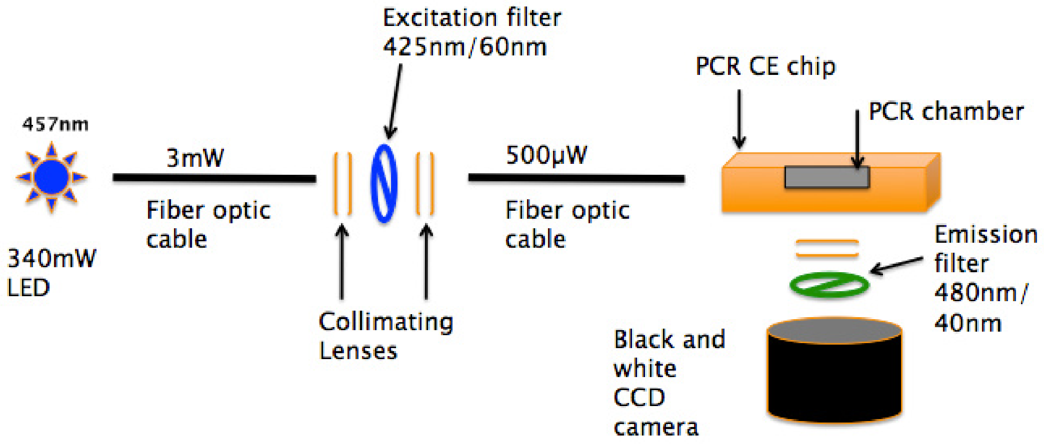

Figure 4.3: Illustration of initial optics design for real time PCR and MCA on the TTK. A 340 mW royal blue (455 nm) LED light source provides light which is coupled into a 1mm fibre optic cable, focused with ball lenses and filtered with excitation and emission bandpass optical filters. The fibre optic cable supplies light to the PCR/MCA chamber within the top glass layer of the PCR/CE-4 chip. Optical detection is carried out using a black and white CCD camera.

As shown in figure 4.3, the excitation light was coupled to the side of the chip (top layer glass, where the PCR chamber is hosted) using a optical fiber. In order to ensure the optical fiber was in a direct contact with the top glass layer (and not the PDMS membrane or bottom glass layer), the top glass layer was designed to be 500 μm larger at it sides. In addition, the tip of the optical fibre was well polished with fine sand paper (5x12' Dissipative hard laminated sand sheets, 3M, Ontario, Canada) and coated with a thin film of index matching gel (glycerol, n = 1.50) to maximize light entering the chip and minimize scatter at the fibre-chip interface.

Nevertheless, there are still power losses associated with transferring light from the optical fibre to the chip. Since the thickness of the top glass layer is 1.1 mm while the PCR chamber is only 90 μm thick, assuming negligible scattering, only 8.2% of the incident light reaches the fraction of the top glass layer that holds the PCR chamber. Consequently, in the best case scenario only about 41 μW of light is available at the PCR chamber for MCA illumination.

On the detection end, light emitted from the excited intercalator in the PCR chamber is gathered by a biconvex lens (15 mm diameter, 25 mm focal length, NT45-879; Edmund Optics Barrington, USA) and then passed through an emission filter (D480/40m; Chroma Technology Corporation, Bellow Falls, VT, USA). This emission filter blocks the excitation light dominated by scattered light from the microfluidic chip and reduces signal baseline levels at the CCD.

Figure 4.4 provides a scale diagram of the optical detection system of the TTK. This optical detection module was completed prior to my arrival at the AML; however, I familiarized myself with the nature and function of the system and applied it to real time PCR analysis. The CCD image sensor is 75 mm away from the biconvex focusing lens. Using the thin lens formula[8], the expected object distance was estimated as 37.5 mm. The optical detection system was adjusted using this value as a guideline to obtain a focused image. The CCD camera is connected to a laptop computer through a USB port. The camera is controlled by Autostar Envisage software (version 2.0, Meade Instruments Corp., Irvine, CA, USA). Using this software a user can set the exposure time and the black/white values of the light that define the contrast and resolution of the images captured.

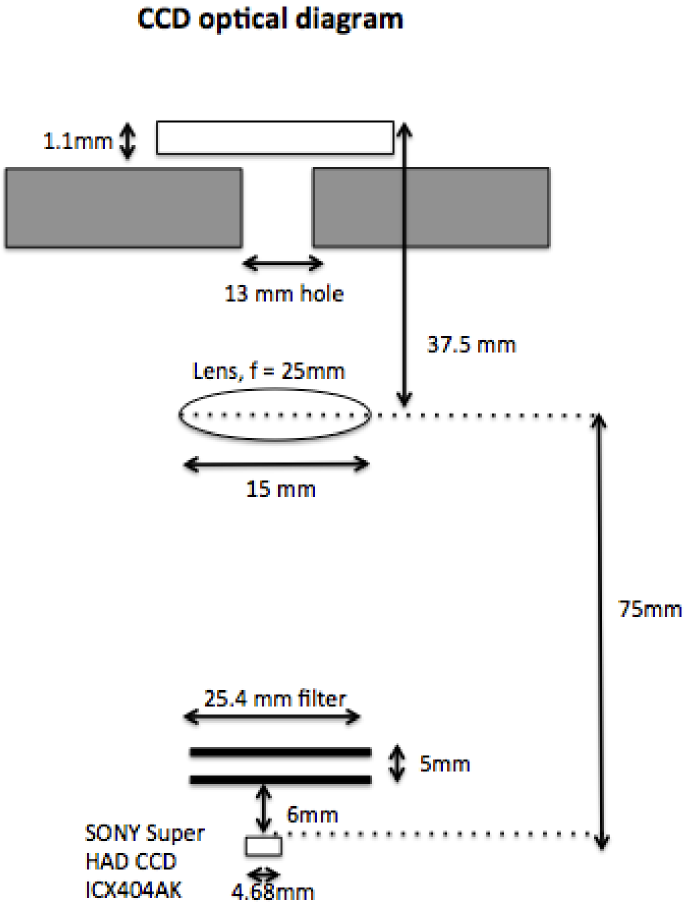

Figure 4.4: Diagram of CCD-based optical detection system in the TTK showing distances between optical components (not to scale). The design of the optical detection system was laid out by G.Kaigala and M.Behnam prior to my arrival at the AML.

The CCD camera was focused so that its viewing area captures ~50% of the PCR chamber. The CCD is set to an exposure time of 700 ms - an empirically-determined value that

---

[8] The thin lens formula states that the relationship between the focal length f, the image distance i, and the object distance o, is given by $\frac{1}{f} = \frac{1}{i} + \frac{1}{o}$.

provided suitable dynamic range for real time PCR detection. In addition, we also empirically determined optimal contrast settings of 4500 and 7000 for the CCD black and white values respectively. The exposure time and contrast settings were chosen so that when the PCR chamber was filled with ß2m PCR product [9] from the conventional thermal cycler, we only obtained 50% of the maximum fluorescence level – this criterion helps to ensure that there is no saturation during a real time PCR experiment and that there is sufficient light intensity to get useful data.

PCR chamber illumination

One of the difficulties with the initial optical illumination and detection design was the need to check the optical coupling to the PCR chamber before each run. It is essential that LED light is properly focused into the top glass layer of the microfluidic chip to reduce scatter and maximize MCA signal strength. However, there was significant variation in the width of the top glass layers of our microchips causing some chips to have very good light coupling when placed in the gantry while others were very difficult to work with. This problem is illustrated in figure 4.5. This light coupling problem reduced the sensitivity of our instrument and did not allow us to obtain repeatable fluorescence measurements from the system.

To address this issue, M.Behnam and C.Bargen (both at the AML) designed a brass LED holder with adjustable height. The setup works like a seesaw – turning the screw downwards raises the LED vertically and vice-versa. This permitted reproducible placement of chips of varying widths on the TTK gantry without significant variation in measured fluorescence. However, this problem was effectively eliminated with a chip-redesign. The top glass layer was made slightly (~0.5 mm) wider than the bottom layer. This made it easier to reproducibly make contact between the optical fiber and the top glass layer facilitating efficient light transfer into the PCR chamber with minimal need for manual optical fiber alignment before each experiment.

Wear and tear in fiber optic cable

Another problem that limited the sensitivity of our optical detection system was routine breakages in the optical fiber. The joint between the LED light source and the fiber optic cable (which is held together by a plastic fitting and glue) is susceptible to wear and tear. This joint consists of glue holding the fiber optic cable directly on top of the LED. During the testing and assembly phase of the optics module, this stress was particularly pronounced as different components were moved regularly. This led to frequent bends in the optical fiber that were difficult to detect because the length of the optical fiber is enclosed in a black light-proof plastic coating. The only signal that something was amiss with the optical fiber was when on-chip experiments failed or showed very little fluorescence. For example, when

---

[9] The ß2m product was prepared starting with 50 ng/μL of template DNA according to standard protocols provided in section 4.3.

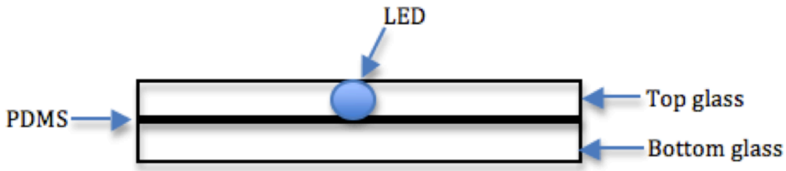

Good light coupling – LED light is focused entirely in top layer

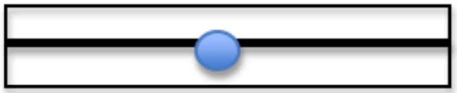

Bad light coupling – LED light enters both top and bottom layers

Figure 4.5: Illustration of proper and improper ways to transfer LED light into the microchip

measurements with a handheld optical power meter gave measurements as low as 50 μW from the optical fiber, the fluorescein limit of detection test described in chapter 5 did not show noticeable fluorescence. In fact, on-chip real time PCR and MCA experiments did not have sufficient optical power for the observation of DNA melting transitions. Instead images captured with the CCD camera were dark and did not have sufficient dynamic range to allow users to distinguish between melted and intact PCR product.

M.Behnam and I undertook the troubleshooting of reduced power supply to the PCR chamber. We performed light intensity measurements with an optical power meter and found that partial breaks in the optical fiber were most troublesome because the LED light did not go off completely, and often the light levels fluctuated and so appeared to be in good working order sometimes. However, power measurements showed that the light reaching the chip had dropped from 500 μW to ~50 μW – crippling the sensitivity of the system.

We addressed these optical fiber breaks by replacing the entire optical fiber, carefully polishing the exposed ends of the cable to reduce scatter. Then we established a new, secure glue joint between the LED and optical fiber that was positioned such that it was not susceptible to regular system movements. In addition, we implement regular optical power measurements to make sure the system provides acceptable LED power output. We defined acceptable power output as measurements of at least 500μW at the fiber optic cable that illuminates the PCR chamber.

4.2.3 Limit of detection (LOD) with fluorescein

Next, I characterized the system's sensitivity by measuring the fluorescence from serial dilutions of fluorescein dye in the PCR chamber. This test was done to check that the optical design and data acquisition/analysis techniques provided a sufficiently low limit of detection (LOD) to facilitate clinical applications. I chose fluorescein because it provides a system benchmark in a manner that can be repeated easily and relatively independent of complex biochemical processes.

I designed and performed this serial dilution experiment with technical assistance from Dr M.Behnam. I started with a stock solution of 1 mM fluorescein (Thermo Fisher Scientific, IL, USA) and diluted it in distilled water to produce 100 μM, 10 μM, & 1 μM solutions. Next, I filled the PCR input well with 5 μL of the each sample and pumped the liquid into the PCR chamber by actuating on-chip pneumatic valves as described in previous work (Kaigala *et al.*, 2008). After filling the PCR chamber with each dye dilution, I captured an image of the PCR chamber with the Meade Deep sky imager (DSI) CCD camera with exposure time set to 1 s, and black and white contrast settings of 7000 and 9000 respectively.

In order to estimate the background fluorescence level when there were no fluorophores in the PCR chamber, I first captured an image of the PCR chamber when it was filled with distilled water only. This baseline fluorescence level is due to the presence of dark currents (small currents inherent in a charge coupled device even in the absence of photon illumination). To determine the variation due to the noise in each image captured by the camera, I repeated this "water-only" measurement 40 times to obtain an estimate of the standard deviation of 0.37 units in the baseline fluorescence level.

Subsequently, I filled the PCR chamber with each of the 1 μM, 10 μM, 100 μM, and 1 mM concentrations of fluorescein, working from the lowest to the highest concentration. To prevent dye build-up in the PCR chamber between consecutive dilution experiments, I rinsed the PCR chamber thoroughly with distilled water (4 washes of 5 μL of distilled water between consecutive runs)[10].

I discarded the 1 mM data point because its average pixel intensity saturated the CCD camera. Saturation occurred because I chose CCD settings that were optimized for the detection of smaller dye concentrations (approaching 1 μM) but not for higher dye concentrations (approaching 1 mM). My reasoning was that the limit of detection was much lower than 1 mM fluorescein, given that the glow from the 1 mM sample was visible to the naked eye. Nevertheless, the elimination of the 1 mM data point reduced the number of data points available to obtain a relationship between the concentration of dye and fluorescence in the PCR chamber – thereby reducing the robustness and accuracy of the test[11].

In order to analyze the CCD images, I used ImageJ (Abramoff *et al.*, 2004) to calculate the average pixel intensity as described in section 4.3.2. The fluorescence data from the serial dilutions of fluorescein is summarized in table 4.2. The fluorescence values provided in table 4.2 do not have specific units but appear on a scale of 0 to 255 based on the resolution of images saved by the CCD camera. The Meade DSI camera has a maximum resolution

---

[10] In retrospect, I should have captured more than 1 image at each concentration so that I could obtain a more accurate estimate of the standard deviation of fluorescence and determine if this value changes as the fluorescence intensity increases. In addition, although visual inspection did not reveal dye build-up in the PCR chamber, I should have captured CCD images during the wash steps between dilutions to estimate how much (if any) dye build-up actually occurred.

[11] In future experiments with PCR product, I chose new CCD camera settings by filling the PCR chamber with 1x10^{11} copies/μL of ß2m PCR product (a strong PCR product obtained for system characterization as described in section 4.3) at room temperature and setting the black and white contrast settings such that the fluorescence intensity was only 50% of the maximum allowable level. In practice, this prevented saturation at high concentrations but also allowed detection of smaller concentrations of PCR product.

of 16-bits when images are saved in a raw, uncompressed format. However, to reduce the amount of storage space required during a typical real time PCR experiment, images were saved in a compressed JPEG format instead[12].

Table 4.2: Fluorescence measurements were obtained from a PCR-CE-4 chip (#0901C18) when it was filled with different concentrations of fluorescein dye. Four fluorescence data points were acquired for concentrations ranging from 10^{-6} to 10^{-3} M; however, fluorescence saturated the CCD camera at 10^{-3} M because the camera's exposure (1.0 s) and contrast settings (black = 7000 units, white = 9000 units) were optimized to detect smaller concentrations of dye. The three non-saturating fluorescence data points were used to estimate the system's limit of detection as discussed in section 4.2.3.

Concentration (M)	**Fluorescence (arb. units)**
1×10^{-3}	255.00
1×10^{-4}	175.45
1×10^{-5}	66.32
1×10^{-6}	21.68
Distilled water	7.32
Standard deviation of background signal	0.37

The Beer-Lambert law describes the relationship between fluorescence intensity and concentration. The relationship between the amount of light transmitted, T, the original amount of light, T_0, and the product of the extinction coefficient, ϵ, optical path length, l, and concentration, c, of a liquid medium is given by the following equation:

$$\frac{T}{T_0} = 10^{-\epsilon \mathrm{lc}} \tag{4.4}$$

With 1 μM of fluorescein dye and an optical path length of 90 μM (equal to the depth of the PCR reaction chamber), I calculated a transmission ratio of 0.9985 using an extinction coefficient of 71000 $\mathrm{cm}^{-1}\mathrm{M}^{-1}$ for fluorescein dye[13]. Since nearly 100 % of the light is transmitted through the dye present in the PCR chamber, it can be considered an "optically thin" medium. This means that the fluorescence measured from the dye in the PCR chamber should be approximately directly proportional to the concentration of dye – so that a doubling of the concentration of dye in the PCR chamber results in a doubling of the fluorescence intensity measured by the camera.

---

[12] A single JPEG image is on the order of kilobytes instead of the megabytes required to save a raw CCD image. When 3000 images are saved for each real time PCR experiment, data storage becomes a bottleneck; hence, compressing images is advantageous. However, as will be discussed in section 4.2.3, image compression has significant ramifications on how quantitation is carried out with CCD images.

[13] I obtained the extinction coefficient of fluorescein from Thermo Fisher Scientific's Pierce protein products website at www.piercenet.com, accessed on february 22, 2011.

Non-linear relationship between fluorescence and dye concentration

However, it is apparent the data in table 4.2 does **not** follow a linear pattern because a 3 order of magnitude change in dye concentration (1 μM to 100 μM) only results in a single order of magnitude change in fluorescence intensity (21.68 units to 175.45 units).

I explored several hypotheses to explain this non-linearity of the fluorescence – concentration relationship. I ruled out dye build-up in the PCR chamber given the use of multiple wash steps between dilutions and the absence of visual evidence suggesting build up while the experiment was carried out. Similarly, I eliminated the image sensor as a potential source of non-linearity since the SONY HAD CCD® sensor in the Meade DSI camera is a linear detector.

While investigating the CCD camera, I realized (on the suggestion of Professor Backhouse) that the CCD camera contains a 16-bit analog-to-digital converter. However the images used in this serial dilution experiment were compressed into an 8-bit JPEG format (with pixel intensities ranging from 0 to 255 units) to reduce storage requirements. Consequently, I considered the hypothesis that JPEG compression introduces non-linearity into fluorescence data.

Gamma compression

When quantitating CCD images, it is best to work with uncompressed data (Medberry *et al.*, 2004). This would require storage of the full resolution image so that any variations in fluorescence intensity would be transferred directly to the CCD image. However, when images are compressed into 8-bit formats such as JPEG, image data is encoded so that the information can be presented optimally on display systems (mostly computer monitors) and interpreted easily by the human eye. Image data is usually encoded in a non-linear manner to cancel out the non-linear behaviour of display systems (Medberry *et al.*, 2004, Poynton, 1996) such as cathode ray tubes which produce a brightness that is not linearly related to current supplied to them. In addition, non-linear image encoding schemes can be further advantageous because they permit contrast enhancement techniques that take advantage of the way the human eye perceives intensity (Joseph, 2002).

Consequently, when saving JPEG images, most CCD-based systems introduce a power law encoding scheme to account for the non-linear nature of display systems and the human eye. This usually takes the form:

$$y = x^{\gamma} \tag{4.5}$$

where y is the intensity of the compressed image, x is the intensity of the original image, and γ is a constant which controls the power law relationship between input and output intensity values. The exact value of γ depends on the design of the CCD camera – specifically which contrast enhancement techniques the manufacturer employs.

The net effect of this power law relationship is that when a γ – compressed image is presented on a non-linear display system like a CRT or flatscreen computer monitor, the image appears at the proper brightness level (Medberry *et al.*, 2004). In effect, gamma correction is designed to cancel out non-linear display of compressed JPEG images on computer monitors. For example, (Poynton, 1996) notes that cathode ray tube displays usually have an inherent gamma factor of 2.2 because of the way electrons strike the display surface when they are translated into brightness on the screen. This results in images being displayed at the proper brightness levels when a 0.45 gamma factor is introduced during compression cancels out inherent 2.2 gamma factor in the display (Poynton, 1996).

In order to use CCD images for quantitation in applications that require digital analysis, it is important to account for the non-linear gamma introduced during image compression before making inferences about sample concentrations in processes such as capillary electrophoresis or melting curve analysis (Medberry *et al.*, 2004). Gamma correction involves applying the inverse of the gamma correction factor to pixel intensities of JPEG images to effectively linearize the image and permit downstream quantitation (Poynton, 1996). This is best done when the exact gamma value for the specific camera is available from the manufacturer. However, this is not always the case – the gamma factor for the Meade DSI camera used in this thesis was not provided by the manufacturer.

To correct the non-linearity in the CCD images gathered while characterizing the qPCR-MCA system developed in this thesis, I obtained an experimental estimate of the gamma factor used to the encode JPEG images from the Meade DSI camera by applying a power fit to the serial dilution data in table 4.2 as shown in figure 4.6. I applied a power fit to the raw data to obtain an estimate of the gamma value applied when encoding the CCD image into the JPEG format.

First, I subtracted the baseline fluorescence level when the CCD was filled with water only. This noise baseline is due to dark current produced in the CCD camera even when photons are not captured (this may be due to current in the CCD as a result of thermal effects). So, to obtain the actual actual relationship between the intensity of the original and compressed images, one must first subtract the baseline due to dark noise.

The power relationship between the fluorescence intensity and dye concentration of fluorescein dye obtained in figure 4.6 is as follows:

$$y - y_0 = 24497\, x^{0.53} \tag{4.6}$$

where y is the average pixel intensity, y_0 is the fluorescence baseline due to dark noise[14], and x is the concentration of fluorescein. I obtained a gamma value of 0.53 with R-squared (coefficient of variation) value of 0.993. Poynton (1996) states that the most commonly used gamma values for JPEG compression are 0.45, 0.55, and 0.68. The experimentally determined gamma value of 0.53 is only 4 % different from the theoretical value of 0.55. In

---

[14] I measured this as 7.32 ± 0.37 units over 40 images with water only in the PCR chamber.

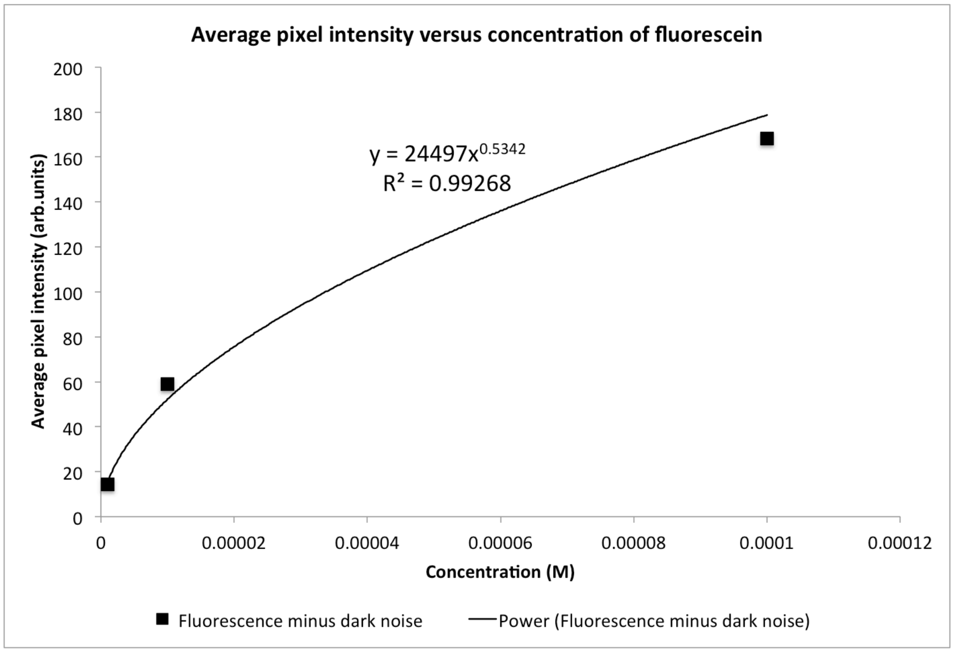

Figure 4.6: Fluorescence versus concentration graph for serial dilution of fluorescein dye. JPEG-encoded images from the Meade DSI camera were analyzed in *ImageJ* software and the average pixel intensities were calculated as shown in table 4.2. I applied a power fit to the data set to estimate the gamma compression factor (i.e. non-linearity) introduced during JPEG encoding (Poynton, 1996).

addition, the strong agreement between the power fit and the raw data (R^2 = 0.993) suggests that this is a relatively accurate representation of the non-linearity introduced when images are compressed by the Meade CCD camera.

Next, I estimated the limit of detection of the system in terms of fluorescein. The limit of detection (LOD) is the required concentration of dye such that the change in average pixel intensity measured by the CCD camera would be equal to 3 times the standard deviation of the background noise signal (i.e. 3 sigma). As mentioned in section4.2.3, the standard deviation across 40 dark images from the CCD camera was 0.37 units[15]. Consequently 3 times the standard deviation (3 sigma) is equal to 1.11 units. The limit of detection of the system can be calculated as 7.34 nM as follows:

$$\begin{aligned} 1.11 &= 24497\, x^{0.534} \\ x &= 7.34 \times 10^{-9} \end{aligned} \tag{4.7}$$

---

[15] This standard deviation value of 0.37 agrees with similar estimates obtained from dark CCD images captured during the pre-denaturation step of real time PCR reactions when the LED is turned off and the camera is sealed from background light. For example, in the sample data set provided in the “Pmal-QPCR-analysis.txt” file the supplementary information, the standard deviation of the 120 images captured during pre-denaturation is 0.25 units.

Estimating LOD in terms of DNA

The objective of the serial dilution experiment was to determine if the system provided sufficient sensitivity for clinical real time PCR and MCA applications. One can estimate the LOD of the system in terms of PCR product by using the theoretical relationships between the optical properties of fluorescein dye and LCgreen plus (the intercalator used in our on-chip real time PCR and MCA tests). I set out to calculate the theoretical concentration of DNA that would be required to produce the same number of photons captured by the optical detection system as when the PCR chamber is filled with the limit of detection concentration of fluorescein i.e. **what concentration of DNA gives the same fluorescence intensity as the limiting concentration of fluorescein?**

First, I calculated the number of photons captured by the optical detection system when the limiting concentration of fluorescein is present in the PCR chamber. This is a multistep process starting with the calculation of the number of photons supplied by the LED light source. The number of photons per second illuminating the PCR chamber is:

$$\begin{aligned} nE_{\text{photon}} &= P \\ n &= \frac{P\,\lambda}{h\,c} \\ &= \frac{500 \times 10^{-6} Js^{-1} \times 455 \times 10^{-9}\ m}{6.6 \times 10^{-34}\ J \times 3 \times 10^{8}\ ms^{-1}} \\ &= 1.15 \times 10^{15}\ photons/s \end{aligned} \tag{4.8}$$

where n is the number of photons per second, E_{photon} is the energy of a photon, λ is the wavelength of the LED light source, h is Planck's constant, c is the speed of light, and P is the optical power. When the 90 μm PCR chamber is filled with the limit of detection concentration of fluorescein, the fraction of light transmitted (transmission ratio) can be calculated using the Beer-Lambert law as follows:

$$\begin{aligned} \frac{T}{T_0} &= 10^{-\epsilon\ C\ \Delta y} \\ &= 0.999989 \end{aligned} \tag{4.9}$$

where T is the amount of light transmitted through the fluorophore, T_0 is the original amount of illumination light from the LED, $\epsilon = 8 \times 10^{4}\ cm^{-1}M^{-1}$ is the extinction coefficient of fluorescein (Cubitt *et al.*, 1995), $C = 7.34 \times 10^{-9}$ M is the limit of detection of the system in terms of fluorescein dye, and $\Delta y = 90\ \mu m$ is the depth of the PCR chamber.The remaining light that is not transmitted is absorbed by the fluorophore. Consequently, the amount of light absorbed by the fluorophore can be calculated as follows:

$$\begin{aligned} \Delta A &= n\,(1 - 0.999989) \\ &= 1.27 \times 10^{10}\, photons/s \end{aligned} \tag{4.10}$$

where ΔA is the number of photons per second absorbed by fluorescein, and n = 1.15 x 10^{15} is the number of photons/s supplied by the LED.

Next, one can express the number of photons captured by the optical detection system as a relationship between the geometry of the optical detection system (the collection efficiency of the system), the properties of the fluorophore (the quantum efficiency of the dye), and the amount of illumination light absorbed by the fluorophore (ΔA). Using these values, I calculated the the number of photons per second captured by the optical detection system as:

$$N = QE \times CE \times \Delta A \tag{4.11}$$

where ΔA is the number of photons per second absorbed by the fluorophore, QE = 0.91 is the quantum efficiency of fluorescein Cubitt *et al.* (1995), and CE is the collection efficiency of the optical detection system. I estimated the collection efficiency as the fraction of illumination light available to the optical detection system. This depends on the geometry of the optical system. I estimated the half angle of the maximum cone of light that can provide light that enters or exits the lens attached to the CCD camera based on dimensions of the optical detection system (described in section 4.2.2). The idea here is that the collection efficiency is approximately equal to the ratio of the solid angle subtended by the lens to a sphere with the same radius. In other words, the collection efficiency is approximately equal to the fraction of the sphere of illumination light that is captured by the optical detection system. The collection efficiency was estimated using the formula:

$$CE = \frac{\Omega}{4\,\pi} = \frac{2\,\pi\,(1 - cos\theta)}{(4\,\pi)} \tag{4.12}$$

where Ω is the solid angle of light collection, and θ is the half angle of the maximum light cone entering the lens. θ is obtained from the relationship:

$$NA = n_{\text{air}}\ \sin\theta \approx \frac{D}{2f} \tag{4.13}$$

where n_{air} = 1 is the index of refraction of air, and NA is the numerical aperture of the biconvex focusing lens (NT45-879, Edmund Optics, Barrington, USA) which can be approximated as the ratio of the diameter D of the lens to the 2 times the focal length f (25mm).

Equation 4.13 gives a value of theta equal to 17.5°. Plugging this value into equation 4.12 gives a collection efficiency equal to 0.023.

Using this estimate of the collection efficiency, one can calculate how much light is captured by the optical detection system using equation 4.11.

$$\begin{aligned} N &= QE \times CE \times \Delta A \\ &= 0.91 \times 0.023 \times 1.27 \times 10^{10}\, photons/s \\ &= 3.02 \times 10^{8}\, photons/s \end{aligned} \tag{4.14}$$

The results of this calculation suggest that when the PCR chamber is filled with a concentration of fluorescein equal to the limit of detection of the system (7.34 nM), then approximately 3.02 x 10^8 photons/s are captured by the optical detection system. This represents that amount of fluorescence available to the optical detection system. To determine the concentration of DNA required to produce the same fluorescence intensity in the CCD camera, I repeated the calculations presented above but switched to the optical properties of LCgreen plus. I set the number of photons/s captured by the CCD as a target, and rearranged the terms in equation 4.11 to number of photons absorbed by LCgreen plus.

$$\begin{aligned} \Delta A &= \frac{N}{QE \times CE} \\ &= \frac{3.02 \times 10^{8}}{0.8 \times 0.023} \\ &= 1.64 \times 10^{10}\, photons/s \end{aligned} \tag{4.15}$$

where N = 3.02 x 10^8 is the amount of light captured by the optical detection system as calculated in equation 4.11, QE = 0.8 is the quantum efficiency of LCgreen plus dye (Mao *et al.*, 2007), CE = 0.023 is the collection efficiency of the optical detection system.

Essentially, I calculated the number of photons per second that would absorbed by LCgreen plus to produce the same fluorescence intensity as when the PCR chamber is filled with the limiting concentration of fluorescein. To determine the limit of detection of the system in terms of DNA, I calculated the concentration of LCgreen plus required in the PCR chamber to produce ΔA = 1.64 x 10^{10} photons/s. I did this by rearranging the terms in equation 4.10 to solve for the transmission ratio needed to so that 1.64 x 10^{10} photons/s are absorbed by the fluorophore. The number of photons, n as calculated in equation 4.8, supplied by the LED light source is independent of the choice of dye, so the required transmission ratio is:

$$\begin{aligned}(1-\frac{T}{T_0}) &= \frac{\Delta A}{n}\\ \frac{T}{T_0} &= 1-\frac{1.64\times10^{10}}{1.15\times10^{15}}\\ \frac{T}{T_0} &= 0.999986\end{aligned} \tag{4.16}$$

Subsequently, I calculated the required concentration of LCgreen plus dye so that the transmission ratio calculated according to the Beer–Lambert law is equal to 0.999986. I rearranged the terms in equation 4.9 to solve for the required dye concentration.

$$\begin{aligned}\log\frac{T}{T_0} &= -\epsilon\, C\, \Delta y\\ C &= \frac{-1}{\epsilon\,\Delta y}\ \log\frac{T}{T_0}\\ C &= \frac{-1}{58000\ cm^{-1}M^{-1}\times 90\times10^{-4}cm}\ \log 0.999986\\ &= 1.16\times10^{-8}\ M\end{aligned} \tag{4.17}$$

where C is the concentration of LCgreen plus, Δy = 90 μm is the depth of the PCR chamber, $\frac{T}{T_0}$ is the transmission ratio, and ϵ = 58000 cm^{-1}M^{-1} is the extinction coefficient of LCgreen plus obtained from estimates of similar dyes by Mao *et al.* (2007).

Equation 4.17 predicts that one would need 11.6 nM of LCgreen plus to obtain the same amount of photons available to the optical detection system as when the PCR chamber is filled with 7.34 nM of fluorescein (the limit of detection). This passes a logical first examination since one expects the limit of detection with LCgreen plus to be slightly higher since the primary differences in the calculation were the use of the extinction coefficient of LCgreen plus (58000 cm^{-1}M^{-1} instead of that of fluorescein (80000 cm^{-1}M^{-1}) as well as the use of the quantum of efficiency of LCgreen plus (0.8) instead of that of fluorescein (0.91). Both of those numbers are smaller for LCgreen plus than fluorescein, and the net effect in the calculation was a higher limit of detection of LCgreen plus i.e. the system is less sensitive to LCgreen plus.

However, the comparison between fluorescein and LCgreen plus is incomplete since multiple molecules of intercalating dyes bind to each DNA molecule. I calculated the actual limit of detection of the system with respect to DNA by considering that the saturating intercalating dye has multiple molecules per base pair of PCR product. While the manufacturer of LCgreen plus does not provide an official number of dyes per base pair of LCgreen plus[16], I estimated the number of dye molecules of LCgreen plus per base pair of DNA as

---

[16] The LCgreen plus info sheet provided at the Idaho Technology website refers to publications by Wittwer *et al.* (2003) which show results from the dye but do not provide the number of dyes per base pair or the extinction coefficient of LCgreen.

being the same of that of SYBR Green I, a competing intercalating dye that has been closely linked with LCgreen plus and has more published properties in the literature Herrmann *et al.* (2006), Wittwer *et al.* (2003). Zipper *et al.* (2004) found that the measured values of the maximum fluorescence intensity from SYBR green dye stayed roughly constant as the number of dye molecules per base pair was increased from 10 to 100. Consequently, they concluded that SYBR green dye saturates at 10 dyes per base pair – this would make up the manufacturer's recommended concentration for a real time PCR reaction (i.e the concentration added to a single 25-μL reaction, commonly known as the 1x solution).

I assumed that LCgreen plus, being a similar intercalating dye, would have similar properties – so I estimated the number of dye molecules per base pair of LCgreen as 10. With this number, I estimated the limit of detection of the system in terms of the 235-bp ß2m PCR product used in preliminary testing of on-chip real time PCR and MCA (as described in section 4.3) as:

$$\frac{1.16 \times 10^{-8}\, moles}{1L} \times \frac{650\, g}{1\, mole} \times \frac{235\, bp}{10\, dpbp} \times \frac{10^{9}\, ng}{1\, g} \times \frac{10^{-6}\, L}{1\, \mu L} = 1.77\, ng/\mu L \tag{4.18}$$

This means that the limit of detection of the system in terms of ß2m PCR product is approximately 1.77 ng/μL. A PCR product on the order of 1-100 ng/μL would represent an intermediate/typical product strength, while a PCR product on the order of pg/μL would be considered a trace amount of PCR product (Lee *et al.*, 2010).

Closing remarks on LOD

A limit of detection of 1.77 ng/μL suggests that while the optical detection system developed here does not represent the state of the art, the system will have sufficient sensitivity to identify medium to high-strength PCR products[17]. As a result, I proceeded to test real time PCR and MCA performance of the system with ß2m PCR product. In addition, I will re-iterate that real time PCR and MCA data presented in this thesis was corrected for non-linear encoding of JPEG images with an experimentally determined gamma factor equal to 0.53. This linearization of CCD data was performed as one of the data analysis steps during real time PCR as described in the following section. This correction yielded real time amplification curves that appeared to have a more exponential growth phase instead of the more linear increase seen in the absence of gamma correction. Finally, I would recommend that in future work, real time PCR data should be saved in uncompressed formats free from non-linear encoding schemes. This will simplify the task of analyzing and interpreting experimental data.

---

[17] A comparison of instrument sensitivities in terms of ng/μL of DNA depends strongly on the choice of sample but still provides an initial estimate of instrument sensitivity.

4.3 Results and discussion

After characterizing the TTK's thermal and optical subsystems, experiments were performed to demonstrate proof of principle on-chip real time PCR. M.Behnam and I performed on-chip real time PCR experiments with ß2m gDNA. The ß2m gene was chosen as a target for these experiments because of prior work (and primer design) that had been completed by our research group and collaborators in past demonstrations involving microchip PCR and CE. This allowed us to test the ß2m assay off-chip and on-chip with capillary electrophoresis (as described in chapter 3).

4.3.1 On-chip real time PCR with ß2m genomic DNA

The reaction mixture for a 25-μL ß2m PCR is summarized in table 4.3. It contains 2.5 μL of 10X PCR buffer (containing 200 mM Tris-HCl and 500 mM KCl, pH 8.4), 2.0 μL of 50 mM MgCl2 (final concentration of 4 mM), 0.5 μL (5U / μL) of platinum Taq polymerase, 0.5 μL of 10 mM dNTPs, 0.5 μL of 1% BSA, 1.0μL of DMSO (4%), 0.5 μL of reverse primer, 0.5 μL of Alexa-647-labeled forward primer, 2.5 μL of 10x LCgreen plus™ (Idaho Tech., USA), 13.5 μL of PCR grade water (nuclease-free, MP Biomedicals Inc. OH,USA) and 1.0 μL of 50 ng / μL of genomic ß2M DNA (replaced with distilled water for negative control experiments). Pt Taq DNA polymerase kits (including Pt Taq, 10X PCR buffer and MgCl2), forward and reverse primers were ordered from Integrated DNA Technologies (Coralville, IA, USA), and dNTPs were purchased from Invitrogen Canada Inc. (Burlington, ON, Canada).

The forward primer was end-labeled with Alexa® 647 dye to permit capillary electrophoresis on the PCR products as a post-PCR test to confirm the results of real time PCR and MCA. This was feasible because the emission spectra of Alexa® 647 and LCgreen plus dyes do not overlap – Alexa® 647 absorbs light at a wavelength of 650 nm, and emits light at 665 nm (i.e. it operates in the red wavelength range) (Kaigala *et al.*, 2008) while LCgreen plus absorbs light in the 440-470 nm range, and emits light in the 500-520 nm range (Wittwer *et al.*, 2003).

The setup for on-chip PCR conditions were the same as in our other work (Kaigala *et al.*, 2010) – I will summarize the details and slight differences here for completeness. The PCR temperature settings were: 90˚C pre-denaturation for 120 s, 72˚C post-extension for 120s, and 35 cycles of 90˚C for 30 s (denaturation), 60˚C for 30 s (annealing), and 72˚C for 30 s (extension). Optical detection was carried out with the CCD camera according to settings described in section 4.2.2. The LED light source was programmed to turn on and off at the beginning and end of the extension step. This was implemented by toggling the output of an digital output pin on the system's microcontroller at the start and end of the extension step using C++ code.

Table 4.3: PCR recipe for ß2m genomic DNA. The fluorescence intensity of the reaction increases as LCgreen plus intercalating dye increases its fluorescence as it binds to newly formed double-stranded DNA. The forward primer was end-labeled with Alexa® 647 to permit post-PCR capillary electrophoresis to confirm reaction results.

Concentration	Reagent	Volume (μL)
	H2O	13.5
1X	LCGreen plus	2.5
1X	10X PCR buffer	2.5
10 μM	5′-5Alexa647N/GTACTCCAAAGATTCAGGTTTACTCAC-3′	0.5
10 μM	5′-ACGGCAGGCATACTCATCTTTTTCAG-3′	0.5
10 mM	dNTPs	0.5
50 mM	$MgCl_2$	2.0
0.02%	BSA	0.5
5 U/μL	Pt. Taq	0.5
4%	DMSO	1.0
50 ng/μL	ß2m genomic DNA	1.0
	Total:	**25**

4.3.2 Real time PCR data processing algorithm

I will now discuss the data analysis algorithm that I developed to construct an amplification curve from CCD camera images gathered during each on-chip real time PCR reaction. The real time PCR analysis algorithm is provided in the "qpcr-analysis-final.py" file in the supplementary information.

Calculating average pixel intensity

First, average pixel intensity values were computed for each picture by passing the image folder to ImageJ(Abramoff *et al.*, 2004). ImageJ is an open-source image processing application written in Java and freely distributed online. It is a robust and open platform that allows users to write custom scripts in programming languages like Python, Java, and C. This permits automated and sophisticated image analysis quickly and inexpensively. I wrote a script in the ImageJ macro language[18] that scans all the pixels in each image[19] and returns a value for the average pixel intensity. As described in section 4.2.2, the camera was focused inside the PCR chamber so that its viewing area contains roughly ~60 % of the PCR chamber and does not include any chamber walls. As a result, each image shows the brightness of the PCR chamber without having to select or exclude specific regions for analysis[20].

Figure 4.7 shows a plot of fluorescence against time obtained during an on-chip real time PCR experiment with ß2m DNA. The CCD camera is turned on before the start of

---

[18] Source code for the ImageJ script is provided in "imagej-script.c" file in the supplementary information accompanying this thesis.

[19] Each image captured by the Meade DSI® camera is 648 x 488 pixels.

[20] The protocol for CCD camera alignment during on-chip real time PCR and MCA detection is provided in "Protocol for optical detection in Angelina using Meade CCD Camera" in the supplementary CD that accompanies this thesis.

the PCR experiment is turned off after the completion of the run. When the LED is off, the fluorescence level is low (baseline due to dark current); however, when the LED turns on during the extension step, there is measurable fluorescence intensity due to the PCR reaction – which increases from cycle 1 to cycle 35.

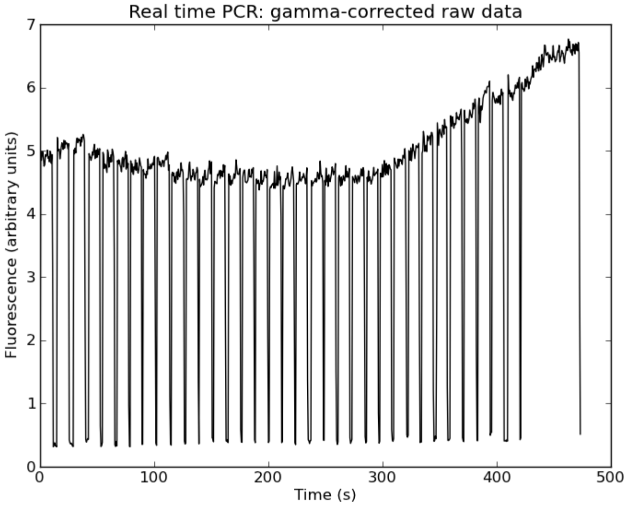

Figure 4.7: Raw fluorescence signal from on-chip real time PCR with ß2m genomic DNA. Regular rises and dips in the signal correspond to the LED turning on and off at the start and end of the extension step. Data was acquired by M.Behnam and analyzed by A.Olanrewaju in July 2010.

Nevertheless, during the PCR reaction, one observes a gentle fluorescence decline for the first 500 images then a rapid fluorescence increase up to the end of the experiment. In addition, at the end of the experiment, there is a sustained increase in fluorescence without any dips in the fluorescence (corresponding to the LED turning off). This corresponds to the 120-second post-extension step at 72°C. During this time, remaining single-stranded DNA molecules are extended resulting in the formation of new double-stranded DNA molecules and increased fluorescence.

The continued increase in fluorescence during this post-extension step suggests that there were a lot of single-stranded DNA molecules left in the on-chip ß2m reaction during the post extension step. This hypothesis seems plausible since there is no clear plateau phase in the amplification curve in figure 4.7,

Gamma correction

The next step in analyzing the CCD images gathered during real time PCR was to perform gamma correction to eliminate non-linear encoding of the images (Poynton, 1996). I accomplished this by adjusting each fluorescence value by raising it to an exponent equal to 0.53 – the experimentally determined gamma factor the Meade CCD camera. As described in section 4.2.3, the experimentally obtained relationship between fluorescence and concentration is given by equation 4.6. In order to reverse this relationship, I calculated its inverse as follows:

$$x = (\frac{y}{K})^{1.87} \tag{4.19}$$

where K is a scaling constant, x is the corrected fluorescence value, and y is the original fluorescence value. This equation is the inverse of the relationship derived in equation 4.6 that details the non-linearity that arises during image storage.

According to equation 4.6, the constant K should be equal to 24497; however, the relationship will be linear with any fixed choice of the scaling constant – but the slope of the line will change. When a constant equal to 24497 is applied, the fluorescence values in the graph are very small (on the order of 10^{-6}). This distracts from meaningful investigation of the properties of the real time PCR curve. Consequently, I scaled the relationship by choosing the scaling constant K to be equal to 10 since the CCD camera settings were chosen such that fluorescence values gathered by the CCD during on-chip real time PCR range between 10^1 and 10^2 units. Choosing a scaling factor of 10 gave fluorescence values that were easy to work with while the application of the exponent (1.87) linearized the relationship between fluorescence and concentration of fluorophore in the PCR chamber. I applied the correction in equation 4.19 to all the data points and obtained new fluorescence values shown in figure 4.8.

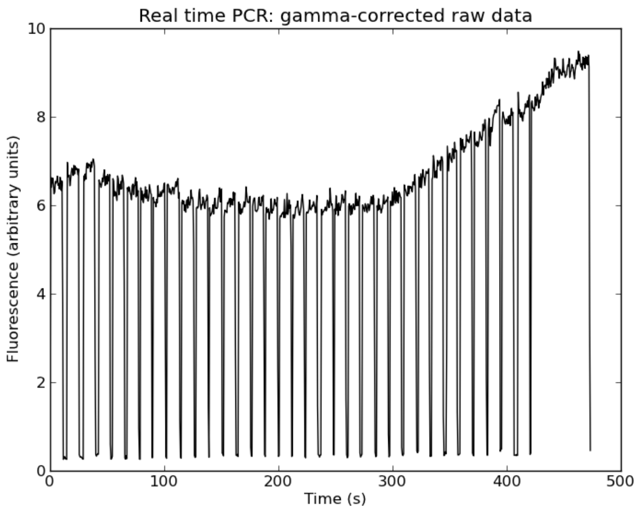

Figure 4.8: Gamma correction of real time PCR data to correct non-linear image encoding by camera as described in section 4.2.3. I applied the transfer function in figure.

It is immediately evident that gamma correction confers a more pronounced curved shape to the plotted real time PCR data. The fluorescence increase in figure 4.8 appears to be a more significant and nearly exponential rise which is in greater agreement with the expected sigmoidal behaviour of real time amplification curves (Rutledge, 2004) than the gently sloping curve obtained in figure 4.7 prior to gamma correction.

Sorting fluorescence data according to PCR cycle numbers

After obtaining the average pixel intensity of all images gathered during the reaction, the next step was to sort the images according to the cycles they were acquired. Because the TTK and CCD employ separate graphical user interfaces, the images were not immediately labeled with the correct cycle number. It was undesirable to have an operator manually sort the images according to cycle number as they were being acquired. As such, I wrote a script in Python to perform automated image sorting (and analysis). I identified each extension step by the turning on/off of the LED leading to a corresponding jump in average pixel intensity. I defined the start of an extension step as: the first image such that the camera fluorescence increased by a factor of at least 1.5 (and stayed at this elevated level). Similarly, I defined the end of an extension step as the first image such that the camera fluorescence decreased by a factor of at least 1.5 (and stayed at this reduced level). These definitions were chosen to select only images with drastic changes in fluorescence intensity as a result of a change of state of the LED.

As one can observe in figure 4.7, there were fluctuations as well as spikes and dips in fluorescence intensity when the LED was turned on/off. As such, it was undesirable to have the script look for a specific fluorescence value corresponding to an LED on/off event. Moreover, the fluorescence intensity was gradually rising throughout the experiment as more double stranded DNA was produced. As such, it seemed optimal to identify extension steps by comparing consecutive average pixel intensities to look for large fluctuations from one image to the next. Defining the start and end of the extension step with this fluorescence comparison approach yielded accurate results and proved robust enough to correctly identify all images gathered in all 35 cycles of the ß2m proof of principle test as well as 3 SP-PCR experiments with buccal cells (see chapter 6), and 1 real time PCR experiment with malaria plasmids.

Next, I averaged the fluorescence over all the images during each extension step (on average 30 images were captured in each extension step) and created a graph of fluorescence versus cycle number as shown in figure 4.9. This exercise was comparable to finding the envelope of the raw fluorescence signal. I included the first and last images (transition points) captured during the extension step in my calculations of real time PCR fluorescence. I made this decision because the CCD camera and the TTK make use of separate graphical user interfaces that are not synchronized in time. This meant that the camera did not capture the exact same number of images during each extension step. The on-chip real time PCR data provided in the "qpcr-sample" text file in the supplementary information[21] illustrates this point – as the number of images captured during each extension step varies from 28

---

[21] The data in "qpcr-sample" was obtained during an on-chip experiment with *Plasmodium* plasmid DNA. The nature of the sample is not the crucial detail here, rather I would like to draw the reader's attention to the intensity of the images captured during the real time PCR experiment.

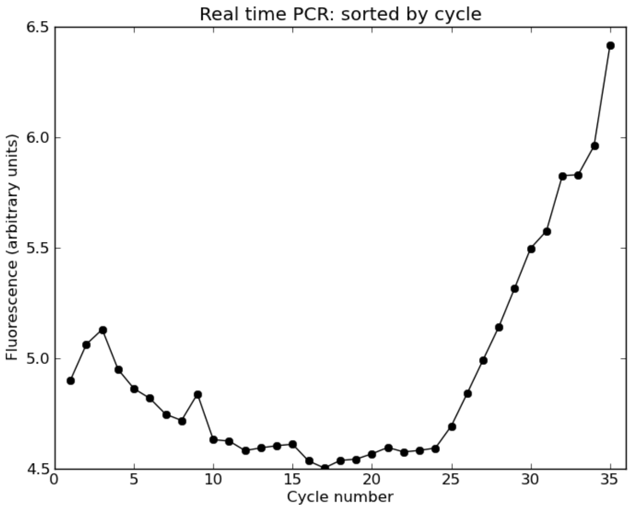

Figure 4.9: In order to eliminate the need for an operator to manually sort real time PCR data according to cycle number, I scripted the separation of images according to their cycle numbers by scanning the average pixel intensities of chronologically-acquired images for LED on/off events. Bumps in the fluorescence data are due noise in the CCD camera (as will be described in detail in chapter 5 as well as the inclusion of transition points when LED turns on/off. Smoothing of the amplification curve is discussed in section 4.3.2

images to 32 images.

To avoid introducing systematic error by analyzing one data set differently from the others, I decided to include all the data points gathered during each real time PCR experiment and to eliminate any resulting noise bumps (from the transition points) by filtering the data. This approach seemed sensible given that each real time PCR experiment provided more than 800 images (data points) permitting the application of smoothing filters without significantly blurring features of the amplification curve.

Smoothing real time PCR data

To get rid of bumps in the raw fluorescence data, I applied a centred 15-point moving average filter to the raw data. As illustrated in figure 4.10, this removed sharp jumps introduced by transition points (at the start and end of extension steps) as well as CCD noise (described in detail in chapter 5).

Baseline subtraction

It is evident in figures 4.8, 4.9, and 4.10, that there is an initial fluorescence decline in the real time PCR curve followed by a rapid fluorescence increase starting just after cycle 20 [22]. This initial fluorescence decline also appears in raw data from conventional real time

---

[22] Raw data for this experiment is provided in the file "b2m-QPCR-July15.xls" in the supplementary information.

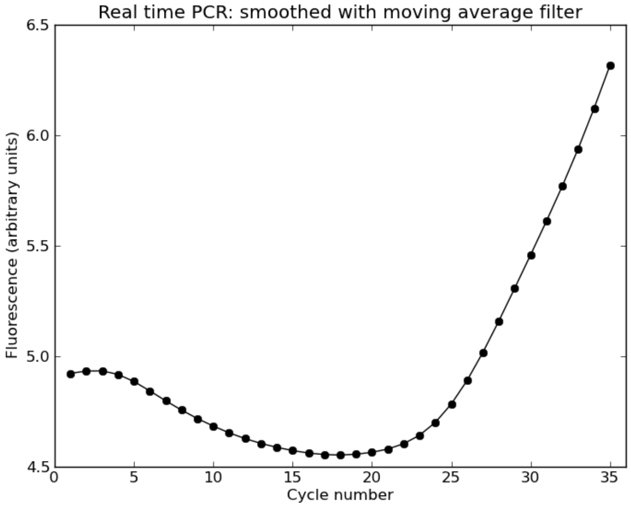

Figure 4.10: Smoothing real time PCR data. I removed bumps from sorted real time PCR data by applying with a moving average filter. I identified the source of noise in the data and described the rationale behind noise removal in chapter 5.1.3.

PCR machines like the Lightcycler and is attributed to temperature-dependent fluorescence decrease of the intercalator and adsorption of the dye by PCR chamber walls in microchip-based systems (Cady *et al.*, 2005).

Baseline correction to eliminate this dye-dependent fluorescence decrease is common in the literature (Neuzil *et al.*, 2010, Rutledge, 2004, Schefe *et al.*, 2006). As such, data gathered from a conventional machine usually shows zero fluorescence during this initial decline period, and then begins to show non-zero increasing fluorescence values once the fluorescence stops decreasing. This allows the user to ignore the ever-present fluorescence decrease and focus on important features of the amplification curve such as the cycle threshold.

Real time PCR curves are usually U-shaped, with the left side representing the gently sloping fluorescence decrease due to dye effects, and the right side representing the rapid exponential fluorescence increase as double stranded DNA is made. Rutledge (2004) suggest defining the baseline as the minimum point of the real time PCR curve (usually somewhere near the middle of the curve) and setting the fluorescence of all the cycles leading up to this point to zero. Next, the minimum value is subtracted from all fluorescence values obtained in cycles after the minimum point.

This was implemented in Python as follows:

```
# ''data'' is an array containing real time PCR fluorescence values
min_index = data.argmin()
min_value = data.min()
# equate all values before min_index to 0 since fluorescence is decreasing
for i in range (0, min_index):
        data[i] = 0
```

```
# subtract min_value from all values after min_index to remove baseline
for i in range (min_index, size(data)):
        data[i] -= min_value
```

Using this simple baseline subtraction approach, I removed the initial fluorescence decline and plotted the amplification curve with a focus on the fluorescence increase as shown in figure 4.11. This allowed examination of important features of the real time PCR reaction such as the calculation of the cycle threshold (Ct value) as described in chapter 1.

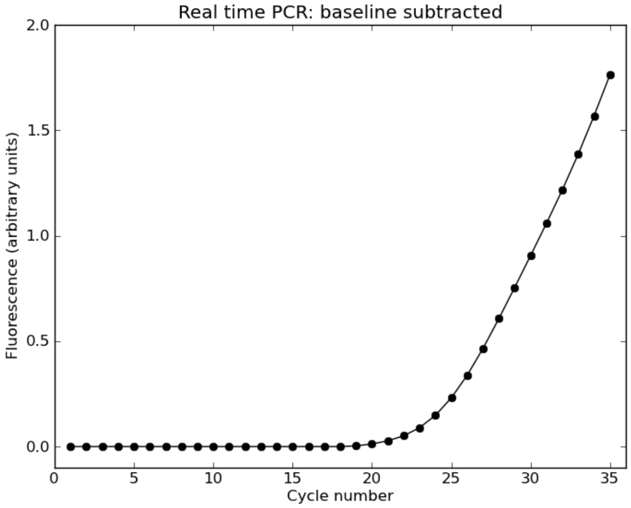

Figure 4.11: The baseline of the amplification curve was removed as described in section 4.3.2, to remove the initial fluorescence decline that is also observed in conventional systems using a simple minimum-subtraction technique described by Rutledge (2004).

Calculating the Ct value

The Ct value is defined as the cycle at which real time PCR fluorescence exceeds background levels (Mackay, 2004). As described in chapter 1, the Ct value is directly proportional to the starting DNA concentration – an important parameter in diagnostic tests (Wilhelm and Pingoud, 2003). A low numerical value for Ct indicates early onset of amplification above background levels. For two PCR reactions with the same efficiency, a lower Ct value corresponds with a larger starting amount of DNA and vice-versa (Gudnason *et al.*, 2007).

One approach to calculating the Ct value involves defining a noise threshold that encompasses the fluorescence from cycles where there is no clear fluorescence increase. This noise threshold usually also includes a measure of fluorescence variation within a cycle as a result of the signal to noise ratio of the instrument in use (Mackay, 2004). There are several different mathematical algorithms for calculating Ct values (many of them proprietary), and these differences can also lead to variations in Ct values between instruments

(Atrazhev *et al.*, 2010, Kubista *et al.*, 2006). This makes a comparison of Ct values between different instruments a tedious and potentially misleading exercise.

I calculated Ct values by adapting the threshold method put forward by Rutledge (2004). I defined Ct as the cycle at which the amplification curve intersects 3 times the standard deviation of noise in the CCD images. I calculated the noise level by determining the standard deviation of fluorescence in each of the images gathered with the CCD camera off. This was advantageous because each real time PCR experiment provided a wealth of dark images captured while the LED was turned off between PCR extension steps. On average 40 images were captured in the time between extension steps[23]. After applying the gamma correction in equation 4.19, the average standard deviation of dark images captured between extension steps (over all 35 cycles of an on-chip real time PCR experiment) was found to be 0.07 units. As such, I defined the Ct value as the cycle number corresponding to a fluorescence equal to 3 times noise level above the baseline i.e. the cycle number corresponding to a fluorescence equal to 0.21 units.

For the data set shown in figure 4.11, the cycle threshold i.e. intersection of noise and amplification curves occurs just after cycle 23 as shown in table 4.4. The raw data for this experiment is provided in full in the "qpcr-smooth.txt" file in the "Ct calculation" folder of the supplementary information. Here, I have focused on the first few images after the fluorescence baseline. As described in section 4.3.2, I implemented baseline subtraction to remove the initial fluorescence decline up to cycle 19 – the point at which the fluorescence in the amplification begins to increase as seen in the raw amplification curve in figure 4.8.

Table 4.4: Data points for Ct calculation for the amplification curve in figure 4.11. I truncated the data provided in the "qpcr-b2m-gdna-smooth.txt" file in the "Ct calculation" folder of the supplementary information to show how the Ct value was calculated by determining the intersection of the amplification curve with the noise baseline.

Cycle number	Fluorescence (arbitrary units)
19	0.00
20	0.01
21	0.03
22	0.05
23	0.09
24	0.15
25	0.23

To estimate the Ct value with the threshold method, I determined the intersection between the amplification curve and three times the standard deviation of noise (0.21 units). Since fluorescence values were only available for each cycle, I used linear interpolation to calculate the Ct value. For the data set in table 4.4, a fluorescence of 0.21 units lies between

---

[23] See qpcr-gamma.txt file in the supplementary information for a sample data set illustrating this.

cycles 24 and 25, so I calculated the Ct value as follows:

$$Ct = 24 + \frac{0.23 - 0.21}{0.23 - 0.15} = 24.3 \tag{4.20}$$

This gave a Ct value of 24.3 units. I estimated the uncertainty in the calculated Ct value using the standard deviation in the noise baseline (0.07 units) as follows:

$$\Delta Ct = \frac{0.07}{0.23 - 0.15} = 0.9 \tag{4.21}$$

In summary, I estimated the Ct value for the real time PCR experiment shown in figure 4.11 as 24.3 ± 0.9 cycles. This is an estimate based on the threshold calculation method. While there are many sophisticated Ct calculation algorithms in the literature (Mackay, 2004, Rutledge, 2004, Schefe *et al.*, 2006), this simple estimate provides a starting point for analysis of on-chip real time PCR results. It gives a metric that can be used to compare the amplification efficiency of real time PCR results on the same instrument.

However, as described in chapter 1, to determine the actual starting quantity of DNA in the reaction, one would need to perform absolute or relative quantification requiring the use of either a calibration curve generated through serial dilutions of a standardized PCR product (Schefe *et al.*, 2006) or by a comparative Ct value method that also requires a well-characterized PCR product (Kubista *et al.*, 2006). I recommend the quantitation of real time PCR products as a topic for further research in chapter 7.

4.3.3 Application: real time PCR with *Plasmodium malariae*

After the proof of principle test of on-chip MCA with ß2m PCR product, the system was tested with a more clinically relevant target – *Plasmodium malariae*. Malaria is an endemic and often fatal disease that poses a risk to over 40% of the world's population (Hay *et al.*, 2009). There are 4 main species of the *Plasmodium* parasite that causes malaria: *P.falciparum, P.ovale, P.vivax*, and *P.malariae*, of which *P.falciparum* is the most deadly (Hänscheid and Grobusch, 2002). Each year, there are over 500 millions cases of *P.falciparum* infection resulting in more than a million 1 million fatalities in sub-saharan Africa alone (Hay *et al.*, 2009).

The gold standard for malaria diagnosis in point of care settings is optical microscopy. It is an inexpensive and productive method for identifying malaria parasites in whole blood. However, microscopy can miss malaria parasites when the degree of infection is low or if the operator is inexperienced. Recent work in the literature has shown that real time PCR assays can be designed for malaria diagnosis in conventional settings in order to provide accurate and user-independent identification of each of the malaria strains (de Monbrison *et al.*, 2003). Lab on a chip technologies have the potential to offer portable and inexpensive real time PCR instruments for point of care malaria diagnosis. The focus of this work was the amplification and detection of the malaria samples (details on sequences and primers will be provided in following section) on the TTK and to compare on-chip results with state of the art conventional methods.

Along with Dr.B.Taylor and Dr.M.Behnam, I performed initial experiments with PCR products from the Lightcycler to measure the melting temperature of experiments with malaria samples on the TTK and to compare them with values obtained on the Lightcycler. Next, on-chip real time PCR and MCA were performed using malaria samples on the TTK. At this stage, I was involved mostly in a data analysis role. Dr.Behnam and Dr.Taylor performed the on-chip real time PCR and MCA experiments, while I analyzed the data obtained. PCR reagents and PCR products for each of the 4 main malaria strains were obtained from our collaborators from the Provincial Laboratories for Public Health (Edmonton, AB). Primer sequences and target templates will be provided for all samples tested in the following section. Each 25 μL reaction mix contained 10^6 copies of malaria plasmid. This corresponds to 24,000 copies of plasmid in a 600 nL on-chip PCR reaction. This is much higher than the single copy limit for the clinically-relevant tests (Lee *et al.*, 2010); however, this experiment was designed as an initial assessment of the system's capability for clinical work with the potential for future dilution experiments to approach clinically-relevant amounts of DNA.

Off-chip real time PCR and MCA with *P.malariae*

It is important to ensure that samples of interest provide acceptable amplification on the conventional system (Lightcycler) prior to on-chip work. Consequently, our first step was to perform off-chip real time PCR and MCA with our samples on the Lightcycler to characterize them. Initial tests on the Lightcycler by Dr.B.Taylor revealed that *P.malariae* provided the strongest real time amplification curve among the different strains. Shokoples *et al.* (2009) suggest that this variation in the strengths of the PCR reactions might be due to different reaction efficiencies. The variations in reaction efficiency might arise as a result of sequence variations in the clinical samples tested within the primer binding regions.

The *P.malariae* sample was prepared on the Lightcycler using the PCR reaction mixture provided in table 4.5. The malaria template samples were obtained from blood collected by the Provincial Laboratories for Public Health – and confirmed as infected with malaria by optical microscopy and DNA sequencing as described in Shokoples *et al.* (2009). DNA was purified using the PSS GC12 instrument (Precision System Science Co. Ltd.) and the 18S gene for each Plasmodium species was cloned into the pGEM-T vector (Promega) as described by Shokoples *et al.* (2009). Subsequent experiments were conducted using plasmids prepared from PCR product. Unique forward primers were designed for each malaria species, while a conserved genus-specific reverse primer was used to amplify each of the malaria strains. Lightcycler thermocycling conditions for real time PCR were predenaturation at 95°C for 120s, followed by 45 cycles of denaturation at 95°C for 10s, annealing at 58°C for 20s, extension at 70°C for 20s, and finally post-extension at 70°C for 120s.

First off-chip controls were performed on a conventional real time PCR machine (Lightcycler) to measure the run-to-run variation in real time PCR results. Two real time PCR ex-

Table 4.5: PCR recipe for 145 bp *P.malariae* PCR product obtained from the publication by Shokoples *et al.* (2009). Real time PCR and MCA were performed on the TTK and on the Lightcycler.

Concentration	Reagent	Volume (μL)
	H2O	13
1X	LCGreen	2.5
1X	10X PCR buffer	2.5
700 nM	Pmal F primer CCG ACT AGG TGT TGG ATG ATA GAG TAA A	1.75
700 nM	Plasmo 2 R primer AAC CCA AAG ACT TTG ATT TCT CAT AA	1.75
200 uM	dNTPs	0.5
2 mM	$MgCl_2$	1
0.02%	BSA	0.5
0.4 U	Pt. Taq	0.5
10^6 copies	Pmal template (*Plasmodium* 18S rRNA gene)	1
	Total:	**25**

periments were performed with the *P.malariae* PCR recipe on the Lightcycler to study run-to-run variation on conventional system. Lightcycler data was processed by proprietary software that performs background subtraction and normalization (Ririe *et al.*, 1997). The amplification curves shown in figure 4.12 had Ct values of 18.63 and 22.71 on the Lightcycler. This difference in Ct values may be attributed to run-to-run variations in the efficiency of the PCR reaction(Kubista *et al.*, 2006). The PCR products were identified by melting curve analysis as will be described in chapter 5.

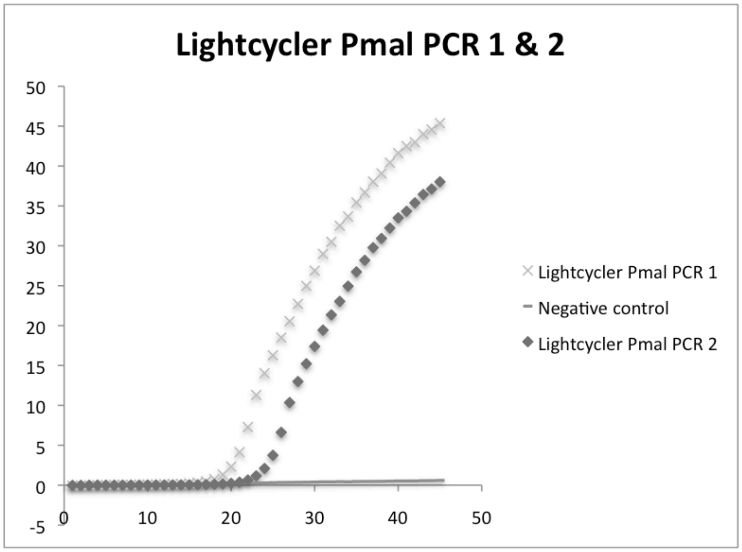

Figure 4.12: Lightcycler amplification curves for *P.malariae* prepared using the PCR recipe in table 4.5. Ct values of 18.63 and 22.71 cycles were obtained on the Lightcycler. This experiment was carried out to study the run-to-run variation in Ct values obtained on the Lightcycler. Data was acquired and analyzed by Dr.B.Taylor.

On-chip real time PCR and MCA with *P.malariae*

After demonstrating that the *P.malariae* samples could be reliably detected on the Lightcycler, on-chip real time PCR and MCA were performed on the TTK. The PCR master mix provided in table 4.5 was used while the on-chip thermocycling conditions were: predenaturation at 90˚C for 120s, followed by 45 cycles of denaturation at 90˚C for 10s, annealing at 58˚C for 20s, extension at 70˚C for 20s, and finally post-extension at 70˚C for 120s. Fluorescence data was acquired during the extension step of each PCR cycle. These data analysis steps included the sorting, gamma correction, smoothing, and baseline subtraction as described in section 4.3.2. On-chip MCA was performed immediately after completion of the real time PCR reaction to check the identity of the real time PCR product as described in chapter 5.

Figure 4.13 shows the amplification curve for on-chip real time PCR reaction with *P.malariae*. Using the threshold technique described in equation 4.20, a Ct value of 18.9 ± 0.6 cycles was calculated. The real time PCR curve has a similar shape to the off-chip chip control which appears to fit the theoretical "sigmoidal" expectation for an amplification curve (Rutledge, 2004).

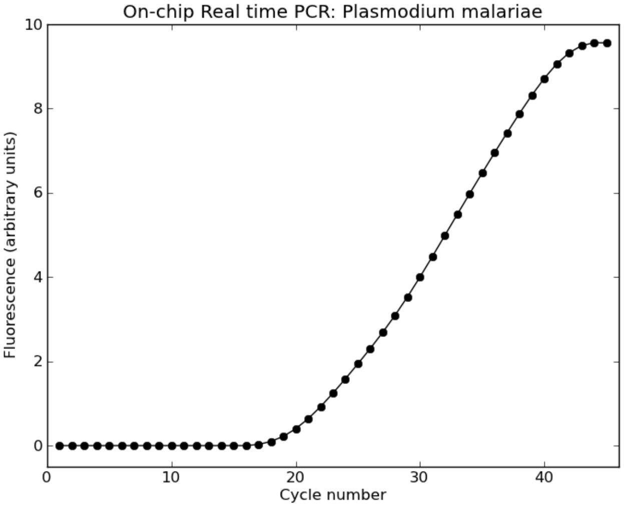

Figure 4.13: Amplification curve for on-chip real time PCR experiment with *P.malariae*. Using the threshold method described in equation 4.20, I calculated a Ct value of 18.9 ± 0.6 cycles. Data was acquired by Dr.M.Behnam and Dr.B.Taylor. Data analysis was performed by A.Olanrewaju.

The strength and melting temperature of the on-chip PCR product was compared with the off-chip product using melting curve analysis. This is described in chapter 5.

4.4 Closing remarks

This chapter described the development and testing of on-chip real time PCR on the TTK. The two main subsystems of the TTK required for real time PCR are the thermal regulation and optical detection modules. These modules were designed by Dr.G.Kaigala and Dr.M.Behnam as part of past work aimed at on-chip PCR-CE at the AML (Kaigala *et al.*, 2008). However, when I joined the lab, I began testing and adapting these modules to permit on-chip real time PCR and MCA.

As described earlier in this chapter, my contributions to on-chip real time PCR on the TTK were:

- characterizing the thermal regulation system by performing measurements with thermochromic liquid crystals,
- measuring the optical power output from each stage of the optical detection system to determine areas most prone to wear and tear,
- carrying out serial dilutions with fluorescein dye to measure the system's limit of detection,
- correcting non-linearities in CCD images as a result of gamma encoding,
- scripting a data analysis algorithm in Python to sort, smooth, and remove the baseline from real time PCR data,
- and calculating the Ct value of real time PCR experiments according to the threshold method.

I performed initial PCR chamber temperature measurements with thermochromic liquid crystals (TLCs) and detected sizeable temperature variations (up to 4°C warmer than design specifications). I found that temperature variations were partly due to fluctuations in room temperature (up to 3°C during a typical PCR reaction) and systematic errors associated with subjective measurement techniques while obtaining TTK temperature with TLCs. To overcome these inaccuracies in the TTK temperature, our research group embarked on a calibration exercise to eliminate the major sources of variation.

While I was not directly involved with the Festival of Calibrations[24] I stayed abreast of the findings so that I could apply the newly-developed protocols and measurement techniques to on-chip real time PCR experiments and data analysis[25]. During the Festival of Calibrations, thermocouples were installed to monitor and compensate for variations in room temperature, TLC-filled microchips were inspected under a light microscope allowing for adjustment of their temperature readings to account for the effect of air gaps in the

---

[24] The Festival of Calibrations was a team effort at the AML to address the complexity of the tasks involved in the thermal calibration of our systems as described in section 4.2.1.

[25] The techniques, findings, and results from the Festival of Calibrations are being prepared by our research group and will be summarized in future work.

PCR chamber. Furthermore, the subjective TLC transition temperature measurements obtained by human eye were replaced with objective and automated measurements using a spectrophotometer. Overall, these improvements greatly increased the accuracy of temperature control in the TTK.

The optical detection system used during on-chip real time PCR is comprised of royal blue (457nm) LED illumination, optical filters, and CCD detection. LED light was channeled through an optical fiber directly into the side of the PCR chamber while CCD detection was carried out directly under the PCR chamber – perpendicular to the illumination. Emission from the sample in the PCR chamber (containing LCgreen plus intercalating dye) was captured by a lens/filter system mounted onto the CCD camera as shown in figure 4.5.

The system's limit of detection was assessed by serial dilution of fluorescein dye in water. This was done to check that the optical detection system was sensitive enough to observe the presence of PCR product. Serial dilution data summarized in section 4.2.3 showed a non-linear relationship between the fluorescence intensity recorded by the CCD camera and the concentration of dye in the PCR chamber. This non-linearity was introduced during gamma correction of CCD images when they were converted from 16-bit raw images into 8-bit compressed JPEG images. Gamma compression of JPEG iamges is usually carried out by raising fluorescence values to an exponent γ with a value that is usually one of 3 commonly used values: 0.45, 0.55, and 0.68 (Poynton, 1996). However, the exact γ value for each camera may vary depending on the manufacturer's choices regarding contrast enhancement.

Since the γ correction factor for the Meade DSI camera was not provided by the manufacturer, I obtained an experimental estimate equal to 0.53 by applying a power fit to the serial dilution data. The experimentally determined gamma value falls within the accepted theoretical range for standard γ values and was obtained with a very good power fit (with a coefficient of variation of 0.993). After accounting for gamma correction, I calculated a limit of detection of 1.77 ng/μL of PCR product as shown in equation 4.18. This indicated that the TTK's optical detection system was sensitive enough to detect intermediate and very strong PCR products (Lee *et al.*, 2010). To confirm this, I performed a proof of principle experiment with ß2m genomic DNA. The LED light source turned on and off at the start and end of each extension step. CCD camera images were carried out continuously throughout the entire experiment – with on average 30 bright images gathered during each extension step and 40 dark images gathered during the time between extension steps.

Because the TTK and camera graphical user interfaces are not synchronized in time, I incorporated the sorting of images into my automated Python script for real time PCR analysis to eliminate the need for an operator to manually sort images during each PCR experiment. My Python script for data analysis consisted of multiple steps and processes. First, I calculated the average pixel intensity of each image using ImageJ software. Then I scanned all the fluorescence values for LED on/off events that allowed me to separate images according to the cycle number in which they were acquired. Next, I applied the gamma correction factor in equation 4.19 to linearize the fluorescence data. Then I smoothed the data as described in section 4.3.2 with a moving average filter to remove noise introduced by CCD variations (discussed in chapter 5). In addition, I removed the dye-dependent fluorescence baseline in the amplification curve that is also observed and discussed in conventional systems (Cady *et al.*, 2005, Rutledge, 2004) to allow a focus on the fluorescence increase following the cycle threshold. Finally, I calculated the cycle threshold by estimating the intersection of 3 times the noise baseline (the standard deviation of all the dark images acquired during each real time PCR experiment).

The amplification curve for the ß2m genomic DNA experiment showed a clear fluorescence increase with a Ct value of 24.3 ± 0.9 cycles. I followed this up by testing *Plasmodium malariae*, one of the 4 main strains of malaria and a more clinically-relevant target. The *Plasmodium malariae* assay shown in figure 4.12 was developed by Dr.B.Taylor according to work summarized in Shokoples *et al.* (2009). Dr.M.Behnam completed on-chip experiments at this stage while I worked primarily in a data analysis role. We observed significant on-chip amplification with a Ct value of 18.9 ± 0.6 cycles as shown in figure 4.13.

The strong on-chip amplification curves obtained for the ß2m and *P.malariae* assays strongly suggest that the TTK can amplify and detect DNA by real time PCR. However, to confirm the intensity and identity of the PCR products amplified, post-PCR analysis is required. Chapter 5 discusses the theoretical background for MCA as well as its implementation on the TTK platform.

CHAPTER 5

Melting Curve Analysis

In chapter 4, I discussed the design, development, and testing of a portable and inexpensive real time PCR system at the AML. Real time PCR monitors amplification progress and provides important information about the starting DNA concentration and relative reaction efficiency. However, real time PCR does not distinguish between amplification curves for different amplicons (Kubista *et al.*, 2006), hence it is important to identify the amplicons after a PCR reaction. A variety of post-PCR DNA amplification techniques have been employed in the literature, including: gel electrophoresis, capillary electrophoresis, DNA microarrays, electrochemical detection, and melting curve analysis (Chen *et al.*, 2007a). However, melting curve analysis (MCA) stands out as a post-real time PCR analysis technique because it requires the same infrastructure and is seamless integrated with real time PCR (Herrmann *et al.*, 2006).

During MCA, a PCR product is slowly heated through its melting temperature (Tm) while the fluorescence from an intercalating dye is monitored. The resulting fluorescence profile ("melting curve") depends on the length and base sequence of the PCR product under investigation (Sundberg *et al.*, 2007). As described in chapter 1 MCA is an indirect assay that does not necessarily uniquely identify a DNA sample but can be used in conjunction with an absolute method of determining the identity of a double stranded DNA molecule (e.g. DNA sequencing or comparison with CE with DNA size standards). However, MCA can be used to distinguish amplicons of interest from unspecific PCR products, since primer-dimers are often shorter than the actual PCR products and tend to have lower Tm values (Kubista *et al.*, 2006). In addition, high resolution melting curve analysis with intercalating dyes has been applied in a variety of diagnostic applications such as the speciation of malaria parasites (de Monbrison *et al.*, 2003), the identification of single nucleotide polymorphisms (SNPs) (Sundberg *et al.*, 2007).

Furthermore, MCA can be integrated seamlessly and inexpensively with real time PCR reactions. Because melting curve analysis makes use of the same infrastructure (heater, optical detection) and reagents (DNA sample, intercalator) as real-time PCR, amplification and analysis can be completed sequentially in the same closed chamber with minimal human intervention. It is much more challenging and expensive to integrate and automate other post-PCR analysis techniques (e.g. capillary electrophoresis or gel electrophoresis) with real time PCR without increasing the complexity, human intervention, and the risk of contamination (Espy *et al.*, 2006).

Description of roles in MCA work

This chapter is focused on the implementation of MCA on the TTK. Towards this end:

- I designed and performed optical hardware calibration experiments with fluorescein dye to estimate system LOD
- I wrote software in Python to smooth and analyze MCA experimental data.
- I led efforts to interpret on-chip MCA results and resolve discrepancies between the TTK and the Lightcycler. I designed experiments to identify the source of the Tm offset between the TTK and Lightcycler.

I worked with Dr.M.Behnam and Dr.B.Taylor to resolve engineering and molecular biology problems during this project. As described in chapter 4, Dr.Behnam designed the original optics hardware and performed maintenance tasks on the TTK to ensure optical operation. Meanwhile Dr.Taylor designed the *Plasmodium malariae* assays used on the TTK and completed off-chip control experiments on the Lightcycler.

5.1 Design of initial approach

Our approach to MCA makes use of the hardware developed for real time PCR (discussed in the previous chapter). Amplicons in the PCR reaction chamber are heated uniformly from a start temperature (T_{start}) to a stop temperature (T_{stop}) at a slow and uniform rate (R_{mca}). During this time, the system's built-in CCD camera captures images of the chamber and records the fluorescence changes that occurs as the DNA is heated (MCA background was discussed in introduction chapter). Afterwards, images from the camera are analyzed to generate melt curves – plots of negative derivative of fluorescence against temperature – from which the melting temperature of the DNA is obtained.

I was involved in 2 key areas of the on-chip MCA implementation, namely:

1. temperature ramp: firmware designed to control sample heating from T_{start} to T_{stop} at ramp rate R_{mca}.

2. data analysis algorithm: algorithm and automated script to analyze images of sample in reaction chamber gathered during MCA ramp. This script generates melt curves and determines Tm values of the analyte.

5.1.1 MCA temperature ramp

Figure 5.1 provides a graphical overview of the operation of the MCA firmware. The source code for the MCA firmware is provided in the "tm.c" file in the supplementary information CD accompanying this thesis. The user enters the desired start temperature (T_{start}), stop temperature (T_{stop}), and ramp rate (R_{mca}) into text boxes in the TTK GUI. These temperature setpoints are passed to the system's central microcontroller using firmware commands. The setpoints are converted into equivalent heater temperatures using the empirical relationship between heater and chamber temperatures provided in equation 5.1.

The start temperature for the MCA temperature ramp is passed to the PI temperature controller (discussed in detail later) which sets the current supplied to the heater until the temperature reaches the desired start temperature. Next, the temperature is held constant for 15 s to allow sufficient time for equilibration[1].

After holding the temperature at T_{start}, the uniform temperature ramp is implemented by steadily raising the heater temperature in an open-loop format. This is accomplished by calculating new temperature set points every 10 ms that are passed to the PI controller. These new temperature set points are calculated by incrementing the current temperature by the product of the ramp rate and the time since the beginning of the ramp (i.e. time since end of 15 s hold at T_{start}). For example, at a ramp rate of 0.05°C/s, the temperature set point 10 s after the ramp began would be 65.5°C. It would take 600 s to reach a temperature set point of 90°C. When the temperature setpoint reaches T_{stop}, the temperature is held for 15s to allow for equilibration and the MCA run ends.

The operation of the MCA firmware can be summarized in four states (0–3) :

- state 0: Temperature controller heats chamber to T_{start}
- state 1: LED turns on, hold temperature at T_{start} for 15s[2]
- state 2: heat at rate R_{mca} until chamber temperature reaches T_{stop}. Update run-time every 100ms and check if temperature has reached T_{stop}. As described in chapter 4, the chamber temperature is not measured directly, rather the heater temperature is measured and mapped to the chamber temperature using an experimentally-derived relationship (see equation 5.1).
- state 3: hold temperature at T_{stop} for 15 s, then turn LED off

The firmware was written by Dr. R.Johnstone and tested experimentally (proof of principle on-chip MCA with PCR product) by A.Olanrewaju. In order to determine optimal

---

[1] As described in chapter 4, the open loop time constant of the system was estimated by Dr. R. Johnstone as 2.5 seconds, so a 15 s hold is equal to 6 time constants.

[2] M.Behnam and S.Groendahl estimate that TTK fully equilibrates at target temperature within 10s.

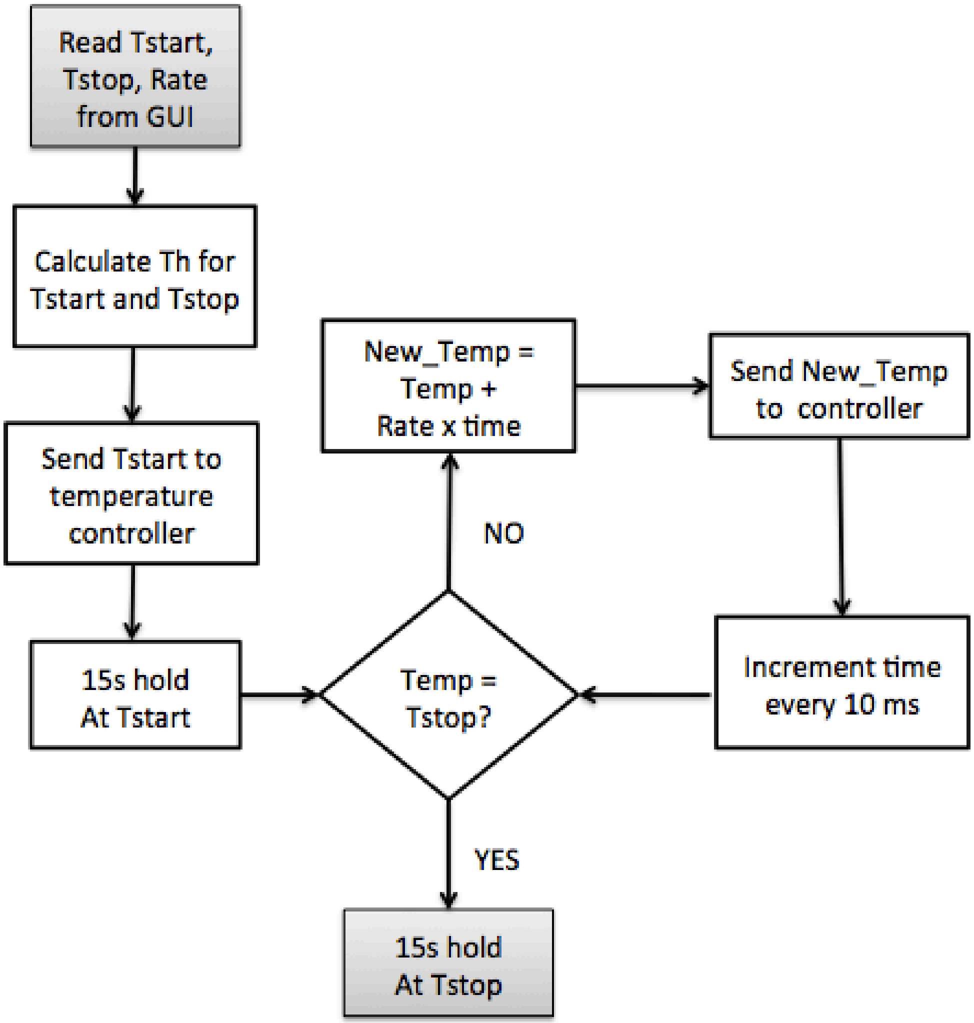

Figure 5.1: Flowchart describing MCA firmware. The microcontroller receives Tstart, Tstop, and ramp rate from the user through text boxes in the system's graphical user interface. The start temperature for the MCA temperature ramp is passed to the PI temperature controller. Next, the temperature is held constant for 15 s (i.e. 6 time constants) to allow for equilibration. Subsequently, the heater temperature is increased linearly by calculating new temperature setpoints by incrementing the current temperature with the product of the ramp rate and the time (since the start of the MCA ramp). These new setpoints are passed to the PI controller which controls the current passed to the heater and increases heater temperature accordingly. The run time in the temperature ramp is incremented every 10 ms and the MCA firmware continuously checks if the temperature is equal to the user-specified stop temperature. At T_{stop}, the temperature is held constant for 15s for equilibration and then the MCA run ends.

ramp rates for on-chip MCA heating, I referred to published MCA literature for a range of acceptable rates (Lee *et al.*, 2010). I passed along these suggestions to J.Martinez-Quijada who modelled the effect of different ramp rates on PCR chamber temperature uniformity in the TTK[3]. He found that ramp rates between 0.05 and 0.5˚C/s produce the expected linear temperature increase in the PCR chamber. As expected, slower ramp rates provide more accurate MCA temperature control, since the system is given more time to equilibrate; on the other hand, faster ramp rates (exceeding 0.5˚C/s) introduce unwanted temperature non-linearities – the temperature ramp begins to get rounded at the edges forming an S-shape instead of a linear increase in temperature (see modelling report in supplementary information).

Variations in heat sink temperature

The current implementation of MCA temperature current is very time sensitive. Run-times are updated every 10ms, and the current temperature is compared against the stop temperature. Heat sink temperature measurements are also timed operations that involve reading the current temperature in the thermocouple. In order to avoid incompatibilities in the timing of MCA temperature increments and heat sink temperature measurements, the Festival of Calibrations experimental team (Dr. M.Behnam, S.Groendahl) did not integrate real-time heat sink temperature monitoring with MCA temperature control.

Nevertheless, heat temperatures are recorded during every on-chip MCA experiment and are accounted for when calculating on-chip Tm values. As described in chapter 4, PCR chamber temperature is updated to account for heat sink temperature variations using the following equation:

$$T_{\text{chamber}} = 0.4649 T_{\text{heater}} + 0.5595 T_{\text{heat sink}} \tag{5.1}$$

where the constant coefficients were obtained by surface-fitting experimentally acquired TLC data[4].

Variations in chip thickness

M.Behnam inferred that if the top or bottom glass layers are too thin, the distance between the PCR chamber and the Pt thin film heater decreases resulting in higher $\text{T}_{\text{chamber}}$ values and vice-versa. This hypothesis was confirmed by FEM simulations from J.Martinez-Quijada. Consequently, we also correct for variations in chip thickness which may lead to variations in PCR chamber temperature. Again, this correction factor is applied after the completion of the MCA work (future work will explore the implementation of real time chip thickness corrections).

---

[3] Jose's FEM simulations for optimal on-chip MCA ramp rate are summarized in "Modelling report No.18 rev 1, February 26, 2009".

[4] These experiments were part of the Festival of Calibrations led by M.Behnam, J.Martinez-Quijada, and S.Groendahl.Their methods and findings are being compiled into a manuscript for future publication.

Prior to each MCA run, the thicknesses of the top glass layer, middle PDMS layer, and bottom glass layer are recorded with an optical microscope with a 5-μm resolution scale rule. We found the greatest variation in the thickness of the top and bottom glass layers (up to ± 50 μm), compared with minimal variations in the PDMS thickness (≤ 5 μm). FEM simulation suggested that the correction factor for the top glass is given by:

$$X_{\text{top}} = \frac{(T_{\text{chamber}} - 22^{\circ}C) \times 0.835 \times (1.1mm - t_{\text{top}})}{(72^{\circ}C \times 0.05)} \tag{5.2}$$

where X_{top} is the temperature correction factor for the top glass layer, t_{top} is the thickness of the top glass layer, and 1.1mm is the ideal thickness of the top glass layer. The correction factor (X_{top}) will be added to the chamber temperature ($T_{chamber}$) to give a more accurate value. For example, for a microchip with a top layer that is 1.08mm instead of 1.10mm, the correction factor for top glass layer thickness at 89°C is +0.3°C. Similarly, we calculate a correction factor for the bottom glass layer using:

$$X_{\text{bottom}} = \frac{(T_{\text{chamber}} - 22^{\circ}C) \times 0.43 \times (1.1mm - t_{\text{bottom}})}{(72^{\circ}C \times 0.05)} \tag{5.3}$$

where X_{bottom} is the temperature correction factor for the bottom glass layer, t_{bottom} is the thickness of the bottom glass layer, and 1.1mm is the ideal thickness of the bottom glass layer. This correction factor is different because the Pt heating element is located on the bottom glass layer. In this case, for a microchip with a top layer that is 1.08mm instead of 1.10mm, the correction factor for bottom glass layer thickness at 89°C is +0.2°C. After the completion of each MCA experiment, the PCR chamber temperature is updated to include the temperature correction factors that account for the top and bottom glass thickness variations as shown in equation 5.4. I implemented this by opening the TTK report file in MS Excel® and creating a new column to the right of the $T_{chamber}$ column. Then I plugged in the measured thickness for the microchip provided by M.Behnam during microfabrication and calculated $T^*_{chamber}$ values using equation 5.4. An example of this calculation is provided in the "Sample-Tc-correction-calculation" MS Excel® file in the supplementary information CD.

$$T^*{}_{\text{chamber}} = T_{\text{chamber}} + X_{\text{top}} + X_{\text{bottom}} \tag{5.4}$$

where $T^*_{chamber}$ is the actual PCR chamber temperature corrected for heat sink temperature, X_{top} is the temperature correction factor for top glass layer thickness, and X_{bottom} is the temperature correction factor for bottom glass layer thickness. At this stage, variations in PCR chamber temperature due to heat sink and microchip thickness variations have been accounted for using FEM simulations and empirical tests carried out during the Festival of Calibrations.

5.1.2 MCA data analysis algorithm

After designing the temperature control algorithm, the next step in MCA implementation is to acquire and analyze images of the PCR chamber during the MCA run. Optical illumination is provided by the LED which turns on at the onset of MCA state 1 (equilibration at T_{start}), and turns off at the conclusion of MCA state 3 (equilibration at T_{stop}) as described in section 5.1.1.

The algorithm for MCA analysis is similar to the one developed in chapter 4.3.2. However, there were a few key differences. First, instead of sorting images according to cycle number, images were arranged according to the temperature they were gathered – permitting the construction of a fluorescence versus temperature graph. Similarly, there was no need for baseline subtraction since MCA tracks the negative first derivative of fluorescence with respect to temperature i.e. -dF/dT vs T, where F is fluorescence and T is temperature.

Nevertheless, much of the analysis stayed the same. The average pixel intensity of each image was first computed in ImageJ, followed by gamma correction, and smoothing with a moving average filter. The Python source code for analysis of images captured during on-chip MCA is provided in the "mca-functions.py" file in the supplementary information CD. I will now discuss the unique features of the MCA data analysis script.

Mapping CCD images to temperature of acquisition

Although the system's GUI records PCR chamber temperatures throughout the MCA run, these values are not synchronized with the camera's start and stop times. The CCD camera is operated with a separate GUI (Autostar Envisage 2; Meade Instruments Corporation, Irvine, CA) that requires manual start/stop with the click of a button. The camera is turned on prior to the start of the MCA experiment and is turned off after the end of the MCA experiment. This way images are gathered throughout the on-chip experiment. However, the lack of synchronization between the CCD and TTK means that images are not immediately sorted according to the temperature at which they were acquired.

In order to match images captured to the PCR chamber temperature at the time they were captured, I organized images according to the start and stop of the MCA experiment. Two landmarks in the design of the MCA firmware are used to match images to the start and end times of the MCA temperature ramp. They are:

- when the LED turns on (i.e. before 15s hold at T_{start}).
- when the LED turns off (i.e after 15s hold at T_{stop}).

Optimal exposure time for the CCD camera was determined to be 0.7 seconds by measuring the fluorescence from the PCR chamber when it was filled with 1 x 10^{11} copies/μL of ß2M PCR product. Empirical tests showed that the camera actually captures 35 images per minute i.e. a real image capture time of 0.58 s (because of internal processes associated with storing images)[5].

---

[5] This was determined by counting the number of images per minute captured by the CCD camera when an

I identified the start of the MCA experiment by observing that when the LED turns on for the first time at T_{start}, the CCD camera will observe the maximum fluorescence throughout the MCA experiment. This is because as the temperature is increased gradually up to T_{stop}, the PCR product will melt and the fluorescence from the intercalator will decrease (Wittwer *et al.*, 2003). As such, I identified the image acquired at T_{start} as the image with the greatest average pixel intensity during each MCA experiment. Similarly, I identified the image acquired at T_{stop} by looking for the final image acquired before the LED turns off. This was implemented readily following the same approach described for selecting LED on/off events as described in chapter 4.3.2.

Furthermore, the start and stop times of the MCA ramp correspond to well-defined temperature setpoints. At the beginning of the MCA ramp, the temperature is equal to T_{start}, while at the end of the temperature ramp, the temperature is T_{stop}. Since the MCA firmware is designed to increase PCR chamber temperature linearly from T_{start} to T_{stop} and the CCD camera captures images at a fixed rate of 1 image every 0.58 seconds, I was able to assign a PCR chamber temperature to each image once I identified the images at T_{start} and T_{stop}.

Keeping the extra images captured during the 15s hold times at the start and end of the temperature ramp would introduce a shift in the melting temperature obtained during data analysis. An image capture rate of 1 every 0.58 seconds means that 9 images are captured during a 15s second time interval. As such, matching CCD images to the start and end times of the MCA ramp involved analyzing only those images between the 9th image after the LED turns on and the 9th image before the LED turns off. I estimate the impact of this truncation on temperature accuracy using the following calculation:

$$18 \div \frac{0.58 \times (T_{\text{stop}} - T_{\text{start}})}{0.05} \times (T_{\text{stop}} - T_{\text{start}}) \tag{5.5}$$

A temperature variation of 5% (1.5˚C) would arise during a typical MCA run with (T_{stop}-T_{start}) = 30˚C if I did not correct for the 15 second hold times at the start and stop of MCA experiments. Such a temperature offset would be important in clinical applications of the TTK. For example, the temperature gap between the melting temperatures of the *P.ovale* and *P.vivax* strains of malaria is only 2.6˚C (de Monbrison *et al.*, 2003). As a result, mapping CCD images to PCR chamber temperatures is an important task in ensuring that the TTK is fit for point of care applications.

5.1.3 Eliminating noise in MCA data

After mapping CCD images to corresponding PCR chamber temperatures, I plotted the fluorescence versus temperature (i.e. denaturation) curve. For the ß2m genomic DNA experiment described in chapter 4.3, the denaturation curve is shown in figure 5.2. The negative first derivative of fluorescence is also plotted against temperature to represent MCA data

---

exposure time of 0.7s was set in the camera GUI. This number (35 images per minute) was consistent across all the MCA runs checked (5).

in form of a peak – whose position can be tracked to provide a relative identification of PCR products (Herrmann *et al.*, 2006, Wittwer *et al.*, 2003).

Noise bumps are visible in the denaturation (fluorescence versus temperature) curve but the change in light intensity as DNA melts is still clearly visible. However, the melt (negative first derivative) curve is overshadowed by noise spikes because the noise is magnified when the first derivative of fluorescence is taken – resulting in large & haphazard noise spikes.

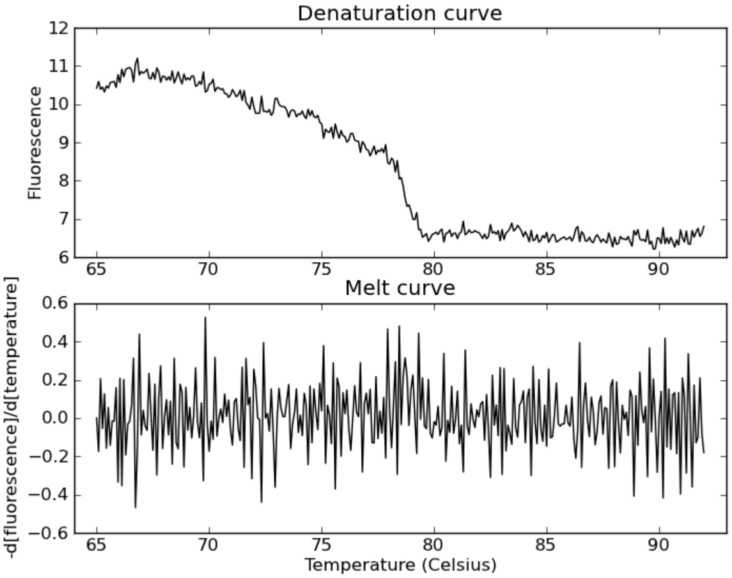

Figure 5.2: The denaturation curve (top) shows fluorescence change with temperature recorded during melting curve analysis of PCR product from on-chip amplification of 50 ng/μL of ß2m genomic DNA. The melt curve (bottom) is the negative first derivative of the denaturation curve and allows analysis of DNA melting by studying peak parameters. Noise spikes in the denaturation curve are amplified when the first derivative is taken to obtain the melt curve. The experiment was performed by Dr.Behnam and the data was analyzed by A.Olanrewaju

In order to properly eliminate the noise bumps, I first investigated their origin so that I could select an appropriate smoothing filter. I will now describe the procedures required to go from raw (and noisy) fluorescence data from ImageJ to smoothed melt curves and Tm values. I will discuss the major sources of noise in our system how we addressed them. **All sources of noise in MCA data are described in this section.** I initially used MS Excel for manual data processing then I wrote a Python script to automate the process and facilitate future integration with the TTK GUI.

To determine if variations in fluorescence were due to ambient light fluctuations, I observed images captured when the CCD camera was completely sealed from background light and the LED was turned off. These conditions are accomplished during the pre-denaturation step of on-chip real time PCR reactions. The system is at its normal operating temperature, covered by a cardboard box to seal off all room light while the LED is turned off.

Figure 5.3 shows images captured during the pre-denaturation step of the *P.malariae* assay described in chapter 4.3.3. The raw data for the fluorescence values in figure 5.3 is provided in the "Pmal-QPCR-analysis.txt" file in the "Noise" folder of the supplementary information.

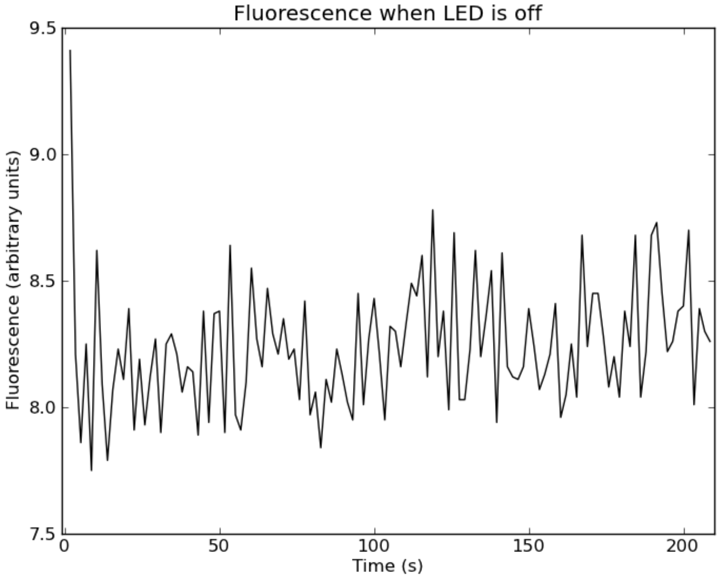

Figure 5.3: Fluorescence from consecutive CCD images captured with the CCD camera is sealed from ambient light and the LED is turned off. This data set was acquired during the pre-denaturation step of the on-chip real time PCR reaction with *P.malariae* providing CCD images at normal operating conditions (e.g. temperature). Numerous noise spikes were observed even in the absence of optical illumination to the CCD suggesting that the noise is inherent in the camera.

There are noticeable noise spikes even when ambient light is blocked. I inspected the images captured with the camera sealed off from background light and noticed horizontal lines that appear randomly with time as shown in figure 5.4. These lines appear to correspond to noise spikes in the fluorescence data. This suggests that the noise observed might be inherent in the CCD camera and largely independent of the illumination.

Inherent CCD noise is a plausible hypothesis since the manual for the Meade DSI camera indicates that it was designed for operation outdoors at room temperature[6]. In addition, the manufacturer recommends that the user take dark frames after letting the camera cool for 5 to 10 minutes.

The manufacturer does not mention operating the camera at high temperatures. For real time PCR and MCA applications, the camera is used at 40 to 70°C higher than the ex-

---

[6] Full operating instructions for the Meade DSI are provided in the manual "Meade® Deep Sky Imager: The Basics", Meade Corporation, Irvine, CA, USA, www.meade.com.

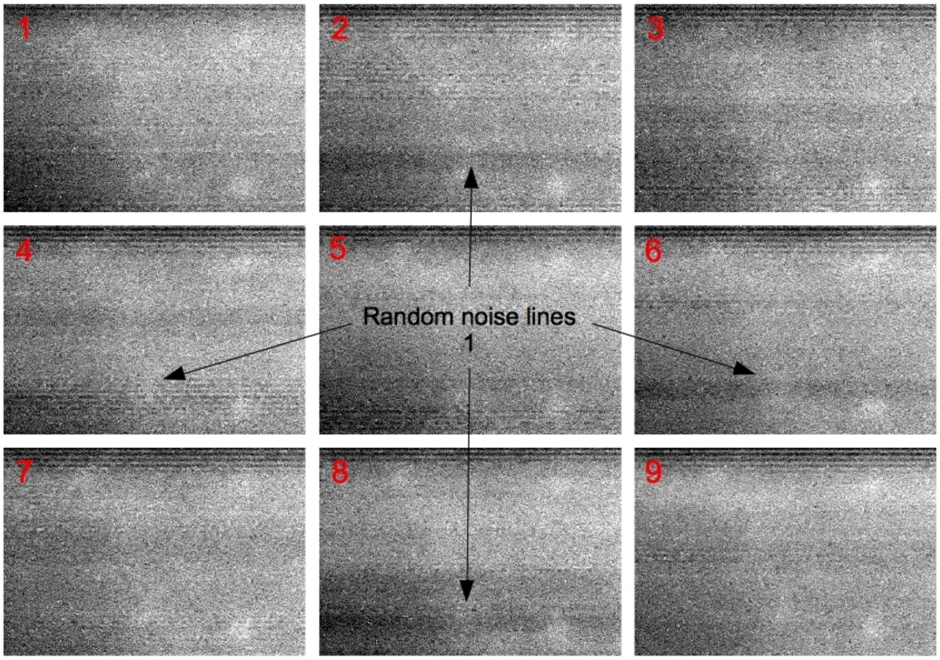

Figure 5.4: 9 images captured sequently with the the camera. Horizontal lines still appear across the screen. These lines correspond to noise spikes in the denaturation and melt curves.

pected operating temperature (room temperature of 25°C). This could introduce noise into the image captured by the CCD. In addition, the noise correction capability of the Meade CCD camera is not automatically enabled. Rather the user must take dark images at room temperature and subtract them from target images to correct for noise inherent in the camera.

In summary, it is feasible that the CCD images were so noisy because the camera was operated well above its recommended operating temperature. In addition, the camera does not automatically correct for noise variations unless dark images are specifically captured (at each temperature) to make such corrections.

In practice, when noise is a major concern in CCD camera imaging, active/liquid cooling components are usually added to minimize read noise (Karellas *et al.*, 1992). Consequently, the absence of active cooling components in our camera[7] might explain the large amplitude of noise spikes observed.

5.1.4 Smoothing MCA data

After identifying the primary source of noise in our MCA images as camera artifacts, I eliminated the bumps by applying a moving average smoothing filter to the MCA data. I will

---

[7] The AML selected the Meade deep sky imager pro monochrome because of its portability and relatively low cost. In addition, the camera was selected for capillary electrophoresis – which is carried out at room temperature, so the increased noise at elevated temperatures was not observed.

now discuss how the filter was chosen. For our application of choice (malaria diagnosis), I needed a separation between MCA peaks of at least 3˚C to be able to distinguish individual malaria strains (de Monbrison *et al.*, 2003). Consequently, the width of the smoothing window was chosen so that the number of data points corresponded to a temperature range of 3˚C as shown in equation 5.6.

$$W = \frac{3 \times \#Images}{T_{\text{stop}} - T_{\text{start}}} \tag{5.6}$$

where W is the size of the smoothing window (and is chosen as the nearest integer value), #Images is the total number of data points gathered during the MCA run, T_{start} and T_{stop} are the start and stop temperatures for MCA. For an MCA run in which 300 data points were captured over a temperature range from 65˚C – 95˚C, we would choose a smoothing window made up of 30 data points in order to limit peak width to 3˚C.

I found experimentally that first applying a median filter helped to remove outliers and then applying a moving average filter smoothed the resulting data set. In addition, filtering the data before and after taking its first derivative was helpful to counteract the amplification of the noise as a result of the derivative operation (noise spikes had a much larger effect when one considered the difference between adjacent values).

I filtered the experimental data using a sequential application of median filter and a moving average filter with a window size calculated according to equation 5.6. This eliminated noise bumps in the MCA data while preserving important features of the MCA curve (i.e. peak position). Figure 5.5 shows the smoothed melt curve from the on-chip real time PCR experiment with ß2m genomic DNA. A melting peak at 78.6˚C was observed.

To study the variation in on-chip melting temperatures, 3 consecutive MCA experiments were performed with same PCR product. The uncertainty in melting temperature (Tm) was estimated as the standard deviation over 3 consecutive experiments. As shown in figure 5.6, melting temperatures of 78.6˚C, 79.9, and 79.2˚C were obtained, giving a standard deviation of 0.6˚C. As such, I concluded that the melting temperature of the on-chip ß2m genomic DNA PCR product was an average of 79.2 ± 0.6˚C.

5.2 Application: real time PCR with malaria plasmids

As in chapter 4, after establishing that the system could perform proof of principle MCA tests with ß2m genomic DNA, the more clinically-relevant *P.malariae* target was tested. The real time PCR recipe and conditions are as provided in section 4.3.3.

5.2.1 Off-chip real time PCR and MCA with *P.malariae*

First, I tested *P.malariae* products from the Lightcycler (conventional real time PCR machine). This was necessary to ensure that the samples of interest provide acceptable ampli-

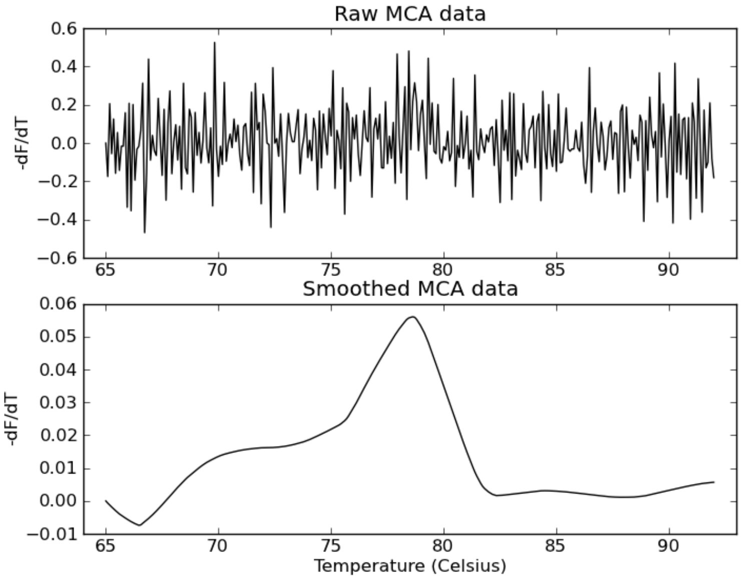

Figure 5.5: Raw data (top) from melting curve analysis of PCR product from on-chip amplification of 50 ng/μL of ß2m genomic DNA was smoothed by the application of a median filter and a moving average filter as described in section 5.1.3. A melting peak at 78.6˚C (temperature corresponding to maximum value of melt curve (Cho *et al.*, 2006)) was observed after smoothing the data set.

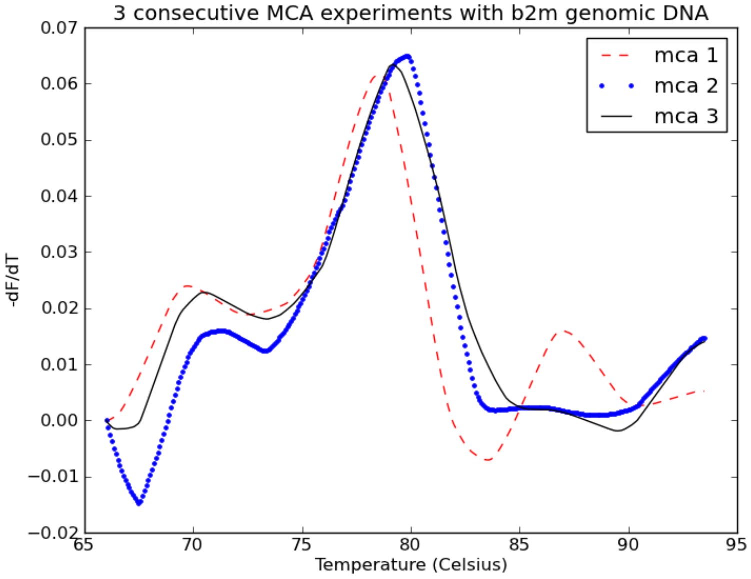

Figure 5.6: Three consecutive melt curves on ß2m genomic DNA prepared on-chip using PCR conditions provided in chapter 4.Tm values of 78.6˚C, 79.9˚C, and 79.2˚C were obtained for runs 1, 2, and 3 respectively. The average Tm value was 79.2˚C with a standard deviation of 0.6˚C over the 3 consecutive experiments.

fication on the conventional system prior to on-chip work. Initial tests on the Lightcycler by Dr. Taylor revealed that *P.malariae* provided strong melting curves as shown in figure 5.7.

Temperature endpoints of 65˚C and 95˚C were chosen as well as a ramp rate of 0.05˚C/s. Tm values of 76.08 ± 0.10˚C and 76.13 ± 0.10˚C were obtained for both samples – the uncertainties in the Tm values were estimated by determining the standard deviation in Tm over 3 consecutive MCA experiments with each sample on the Lightcycler. The Tm values obtained for Pmal PCR runs 1 and 2 agree within error.

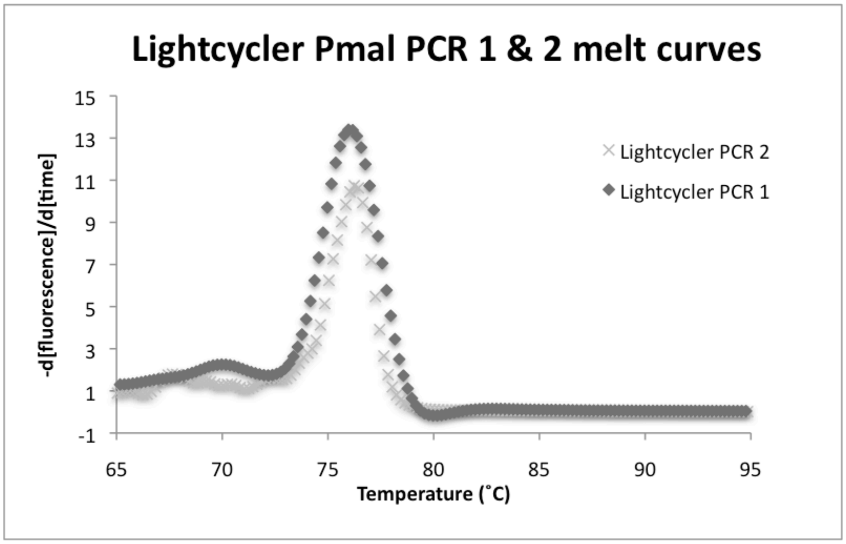

Figure 5.7: Lightcycler melt curves for two separate *P.malariae* PCR products prepared using the recipe in table 4.5. Tm values of 76.08 and 76.13 ± 0.10 ˚C were obtained indicating that the 2 values were in agreement. This experiment provided a prediction of the Tm value that should be expected during on-chip MCA with the same PCR product.

5.2.2 On-chip MCA with malaria samples

After characterizing the Pmal sample on the Lightcycler, on-chip MCA was performed using the same settings as on the Lightcycler as described in figure 5.7. Temperature endpoints of 65˚C and 95˚C as well as a ramp rate of 0.05˚C/s were chosen.The PCR input well was filled with 4 μL of Pmal PCR product from the Lightcycler and pumped into the PCR chamber as described in section 4.3. Two consecutive MCA experiments were performed with the same PCR product.

As shown in figure 5.8, a clear melting transition was observed at 70.0˚C in both MCA runs. However, the left side of the peak is cut off in the melting curve – this is because the Tm value on the TTK was measured as 70˚C instead of the 76˚C observed on the Lightcycler. I chose a temperature range of 65˚C to 95˚C because I expected that the on-chip Tm value would appear at the same temperature as on the Lightcycler. The 6˚C temperature offset between the TTK and the Lightcycler is discussed in section 5.3.4.

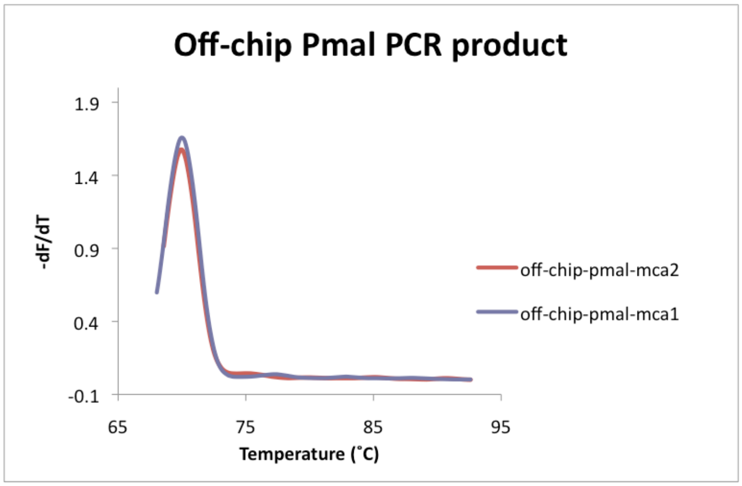

Figure 5.8: Two consecutive on-chip MCA runs with off-chip *P.malariae* PCR product. Both MCA runs had Tm values of 70.0 ± 0.1˚C with amplitudes of 1.66 ± 0.05 and 1.58 ± 0.05 units respectively. -dF/dT represents the negative first derivative of fluorescence with respect to temperature. The leading edge of the melting peak is cut off in the figure because the on-chip peak appeared at 70˚C instead of the expected peak at 76˚C obtained on the Lightcycler. The 6˚C offset between the TTK and the Lightcycler is discussed in section 5.3.4.

The melting curve was considered valid even though its leading edge was cut off because the Tm value (maximum value of the melting curve) was obtained reproducibly over 2 consecutive MCA experiments with the same off-chip PCR product. In addition, subsequent experiments with on-chip PCR products (see figure 5.9) also gave a melting peak at approximately the same temperature.

5.2.3 MCA with on-chip *P.malariae* PCR product

After demonstrating that *P.malariae* samples prepared on the Lightcycler could be detected by MCA on the TTK, PCR product from on-chip real time PCR was tested next. The PCR master mix and conditions were described in table 4.5. On-chip MCA was started immediately after completion of the real time PCR reaction without the need for any manual intervention steps other than to hit the start button.

As shown in figure 5.9, a clear melting peak was observed for the on-chip *P.malariae* PCR product. This makes sense given that a very strong amplification curve (with a Ct value of 19.2 ± 0.3 cycles) was observed for the on-chip PCR product as shown in figure 4.13.

I repeated the on-chip MCA with the PCR product 3 times to estimate the run-to-run variation in Tm values across consecutive MCA experiments. I obtained an average Tm value of 69.1 ± 0.3˚C for the *P.malariae* PCR product.

The Tm value for the on-chip PCR product (69.1 ± 0.3˚C) was very close to that of the Lightcycler product (70.0 ± 0.1˚C). This suggests that whether a sample is prepared on the

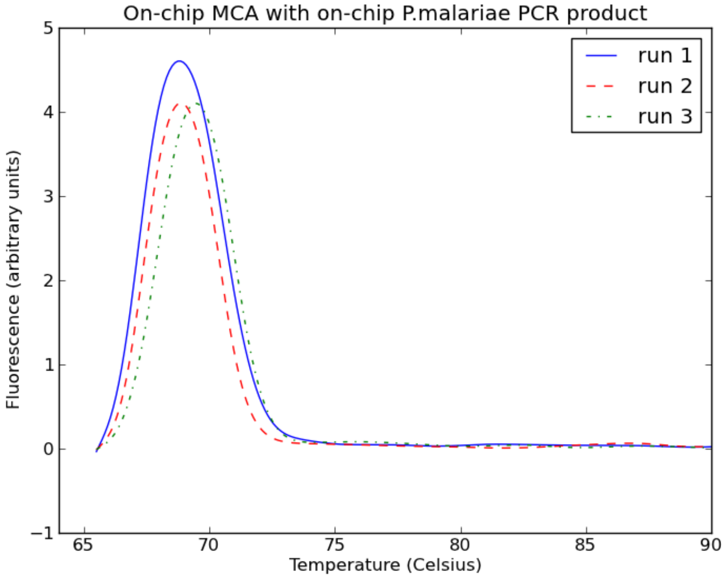

Figure 5.9: Three consecutive on-chip MCA runs with on-chip *P.malariae* PCR product. I obtained an average Tm value of 69.1 ± 0.3°C. As described in figure 5.8, the leading edge of the melting peak is cut off because the on-chip peak appeared at 70°C instead of the expected temperature of 76°C obtained on the Lightcycler. The 6°C offset between the TTK and the Lightcycler is discussed in section 5.3.4.

TTK or on the Lightcycler, roughly the same Tm value is measured by the TTK during on-chip MCA analysis.

5.2.4 Distinguishing multiple strains of malaria with on-chip MCA

Next, on-chip MCA was performed using a multiplexed sample containing all 4 malaria strains. Primers and templates for each of the four main malaria strains were added to the reaction mixture as described in Shokoples *et al.* (2009) and summarized in table 5.1. Primers and templates for each of the four main malaria strains were added to the reaction mixture. Individual forward primer sequences specific to each malaria species are used. Meanwhile the reverse primer sequence is specific to the genus and is used to amplify all of the malaria species. DNA from all four malaria strains were mixed in equal proportion in the same PCR reaction.

The multiplexed real time PCR reaction represents a significant advance in malaria diagnosis and improves upon the sensitivity and accuracy of optical microscopy (gold standard) and rapid diagnostic tests (Shokoples *et al.*, 2009). The multiplexed reaction could be helpful in the detection of mixed infections of different malaria strains present in the same clinical sample. On-chip MCA was performed with this multiplexed sample to test the TTK's ability to distinguish closely-spaced DNA peaks as preliminary work towards malaria diagnosis on a microfluidic platform. In addition, this experiment would provide additional data to study differences between Tm values measured on the TTK and on the Lightcycler.

Table 5.1: PCR recipe for multiplexed malaria PCR reaction obtained from Shokoples *et al.* (2009). On-chip MCA was performed with this multiplexed sample to test the TTK's ability to distinguish closely-spaced DNA peaks as preliminary work towards malaria diagnosis on a microfluidic platform.

Reagent	**Volume (μL)**
H_2O	5
Lightcycler fast-start DNA master mix	2.0
0.02% Bovine serum albumin (BSA)	0.6
1x LCGreen	2.0
50 nM Pm1 CCG ACT AGG TGT TGG ATG ATA GAG TAA A	1.4
50 nM Pov1 CCG ACT AGG TTT TGG ATG AAA GAT TTT T	0.8
50 nM Pv1 CCG ACT AGG CTT TGG ATG AAA GAT TTT A	0.8
200 nM Pfal-F CCG ACT AGG TGT TGG ATG AAA GTG TTA A	0.4
Plasmo 2 R primer AAC CCA AAG ACT TTG ATT TCT CAT AA	3.4
2 mM $MgCl_2$	1.6
$1\text{x}10^6$ copies 18 S rRNA gene from *P.falciparum*	0.4
$1\text{x}10^6$ copies 18 S rRNA gene from *P.ovale*	0.4
$1\text{x}10^6$ copies 18 S rRNA gene from *P.vivax*	0.4
$1\text{x}10^6$ copies 18 S rRNA gene from *P.malariae*	0.4
Total:	**20**

The Pmulti sample was first analyzed on the lightcycler as shown in figure 5.10(a). Four melting peaks corresponding to each of the malaria strains, *P.malariae, P.vivax, P.ovale* and *P.falciparum*, were clearly visible at melting temperatures of 75.4, 80.0, 83.1, and 87.4 ± 0.1˚C respectively.

When MCA was performed on the TTK, all 4 peaks were visible; however, the melting peaks appeared at temperatures of 68.6, 72.5, 75.4, and 78.9 ± 0.1˚C for the *P.malariae, P.vivax, P.ovale* and *P.falciparum* strains respectively as shown in figure 5.10(b). The leading edge of the melt curve is cut off because I chose the same temperature endpoints as on the Lightcycler since I expected the melting peaks to appear at the same temperatures on both platforms. However, the peaks appeared between 6 and 8˚C earlier than they did on the Lightcycler. The peak positions were repeatable across 2 consecutive MCA runs with a standard deviation in Tm of 0.1˚C. The discrepancy between TTK and Lightcycler melting temperatures is discussed in section 5.3.4.

5.3 Temperature offset between TTK and Lightcycler

On-chip MCA results (see table 5.2) show an average melting temperature difference (ΔTm) of 6.3˚C between the TTK and the lightcycler. Tm measurements on the TTK were 5.4 – 7.4˚C lower than those obtained on the lightcycler. This data suggested that the TTK was ~6˚C hotter than the desired temperature setting within the 60 – 90˚C temperature range for the malaria species tested.

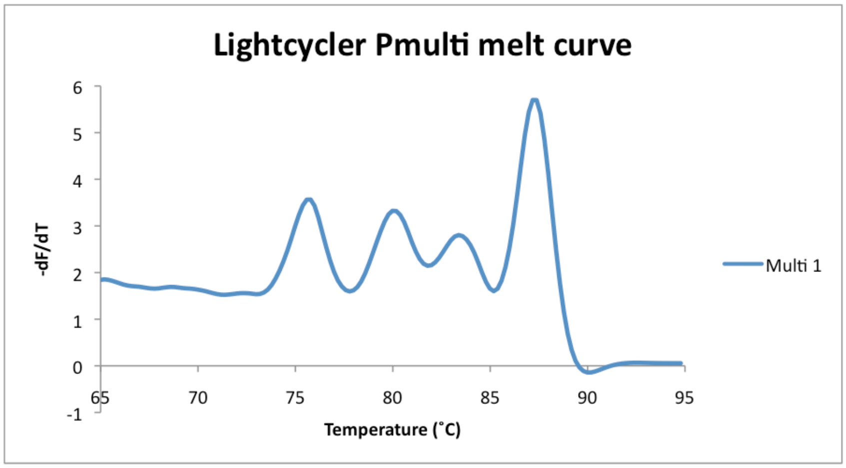

(a) Lightcycler melt curve for multiplexed malaria sample prepared according to the recipe in table 5.1. Tm values of 75.4, 80.0, 83.1, and 87.4 ± 0.1˚C were obtained for *P.malariae, P.vivax, P.ovale* and *P.falciparum* peaks respectively in agreement with results in Shokoples *et al.* (2009).

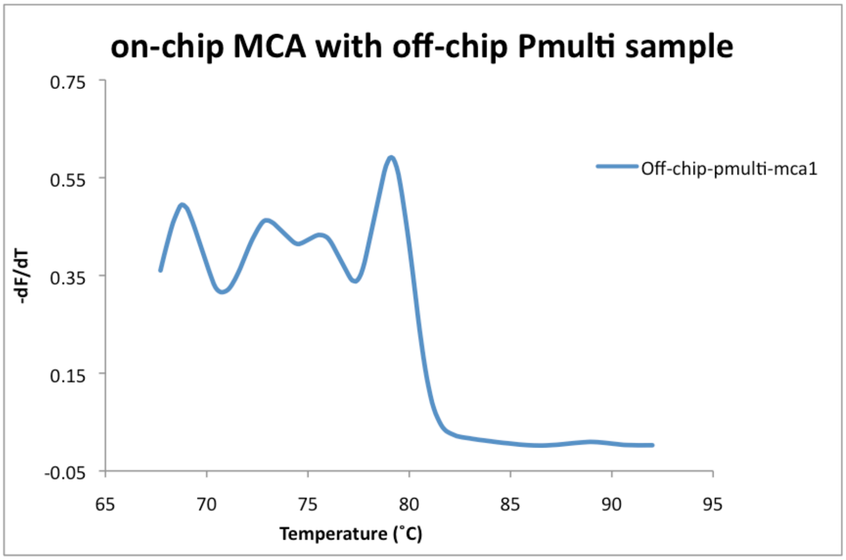

(b) On-chip melt curves with Lightcycler Pmulti PCR product prepared according to the recipe in table 5.1. Tm values of 68.6, 72.5, 75.4, and 78.9 ± 0.1˚C were obtained for *P.malariae, P.vivax, P.ovale* and *P.falciparum* respectively. These Tm measurements are between 6 – 8˚C less than values obtained on the Lightcycler (see figure 5.10(a).

Figure 5.10: Lightcycler (a) and TTK (b) melt curves for multiplexed malaria sample. The TTK Tm values are 6 – 8˚C lower than their Lightcycler counterparts. This temperature offset is discussed in section 5.3.4.

Table 5.2: Summary of melting temperatures measured on Angelina and the Lightcycler after the Festival of Calibrations. Samples were prepared on the lightcycler using 1x10^6 copies/μL of each template. The 2.2˚C variation in temperature offset for each sample agrees with our expected ± 1˚C run-to-run variation for on-chip MCA experiments.

Sample	TTK Tm (± 0.1˚C)	Lightcycler Tm (± 0.1˚C)	ΔTm (˚C)
P.falciparum	80.5	86.7	6.2
P.malariae	70.6	76.7	6.1
P.ovale	75.4	82.8	7.4
P.vivax	74.5	79.9	5.4
		Average	6.3

Identification of PCR products by MCA requires accurate knowledge of the Tm of each amplicon. For example, the melting temperature of each of the 4 main strains of malaria differs from its nearest neighbour by at least 3˚C (Mangold *et al.*, 2005). Consequently, an unexplained temperature shift of 6˚C in on-chip Tm values would strongly compromise the ability of our TTK to make strong and accurate statements about malarial samples. However, if the origin of the temperature offset could be reliably identified and its effects were eliminated, then acquired data could be corrected.

This section details the investigation and resolution of the 6˚C temperature offset in on-chip MCA data. I led this troubleshooting effort – I formulated hypotheses, and performed experiments to test them. I received plenty of insight and experimental assistance from Dr.M.Behnam, S.Groendahl, and S.Caverhill-Godskewitch in this effort.

On-chip Tm values calculated by the TTK depend on 4 main factors:

1. Biochemical processes: molecular biology protocols and phenomena
2. TTK Hardware: microchip and system calibrations
3. TTK Software: graphical user interface and data analysis algorithms
4. TTK Firmware: MCA temperature control algorithm and heater PI controller.

Consequently, a thorough examination of each of these modules should reveal the source of the anomaly in our system. Experiments ruled out biochemical processes, hardware, and software as likely sources of the temperature offset. Data gathered during detailed troubleshooting revealed that a firmware artifact was responsible for the temperature different between TTK and lightcycler results. I will now describe the approach for testing each factor that affects on-chip Tm values leading to the conclusion that the firmware was the origin of the offset.

5.3.1 Biochemical processes

Tm values obtained during MCA can be used as an indirect assay to distinguish PCR products according to their chemical composition, base sequence, and length (Espy *et al.*, 2006, Sundberg *et al.*, 2007). However, biochemical factors such as salinity and chemical nature of the intercalating dye also influence the measured melting temperature of a PCR product (Kubista *et al.*, 2006). I explored the effects of salinity and dye effects on TTK Tm values to determine if they were responsible for the measured temperature offset.

Variations in salt concentration

The salt concentration of a DNA sample significantly affects its chemical properties and melting temperature (Herrmann *et al.*, 2006). As such, variations in salt concentration of a PCR product could lead to shifts in its Tm value. There are several publications that provide theoretical models for the calculation of the melting temperature of DNA. For example, the DINAmelt web server[8] for predicting DNA melting temperatures is a robust platform that simulates DNA melting and equilibrium temperature profiles (Markham and Zuker, 2005). However, while the DINAmelt server estimates the effects of potassium and sodium ion concentrations on DNA melting temperature, it does not predict the effect of changing magnesium ion concentration on DNA melting temperature – limiting its applicability in experiments where magnesium ions are included in the PCR reaction von Ahsen *et al.* (1999). Calculations by Nakano *et al.* (1999) and von Ahsen *et al.* (1999) suggest that including 1.5 mM Mg^{2+} ions in a PCR mix raises the melting temperature by 5 – 8°C depending on the nature of the oligonucleotide (sequence differences influence Tm value).

1.5 mM Mg^{2+} was included in the real time PCR recipe that is used for both on-chip and off-chip ß2m and *P.malariae* reactions as shown in tables 4.5 and 4.3. One hypothesis that was considered as an explanation for the Tm difference between the TTK and the Lightcycler was that the microchip surface contributed to variations in the concentration of Mg^{2+} ions in on-chip real time PCR reactions, resulting in a measurable Tm difference between on-chip and off-chip reactions.

To investigate this hypothesis, Dr. G.Banting, Dr. M.Behnam, and I performed on-chip MCA experiments with 100% and 0% of the standard Mg^{2+} ion concentration in an on-chip MCA reaction. The objective of this experiment was to measure the effect of variations in Mg^{2+} concentration on the measured on-chip Tm values. This hypothesis considered an extreme scenario where there was a 100% change in the concentration of Mg^{2+} in the on-chip reaction.

To reduce variations associated with using complex genomic DNA samples, MCA was performed using double-stranded DNA formed by the hybridization of complementary 23-bp oligonucleotide primers. The primers used were COX11 F145I 5'-AGA ATT CGT ATC TCA ATC ACC AGT GAA GTA TCA-3' and its complement. The forward and reverse primers were mixed at room temperature and then hybridized them by heating to 95°C for 1 minute in the thermocycler (PTC-200, MJ Research, MA, USA). The mixture was removed from the thermocycler and allowed to cool at room temperature for 5 minutes. After preparing short double-stranded DNA from complementary primers, MCA was performed with a ramp rate of 0.05°C/s and temperature end-points of 50°C & 70°C. A 50-μL master

---

[8] Accessed online at http://www.bioinfo.rpi.edu/applications/hybrid/

mix with the standard (100%) salt concentration was prepared from 2 μL of COX11 F145I F primer, 2 μL of COX11 F145I R primer, 5 μL of 10X PCR buffer, 5 μL of 10X LCgreen, 50 mM of $MgCl_2$, and 34.5 μL of water. This made for a final concentration of 1.5 mM Mg^{2+} – the standard concentration in our on-chip MCA experiments. The master mix without salt (0%), contained 2 μL of COX11 F145I F primer, 2 μL of COX11 F145I R primer, 5 μL of 10X PCR buffer, 5 μL of 10X LCgreen, and 36.0 μL of water ($MgCl_2$ was replaced by increasing volume of water).

With 0% salt in the MCA reaction mix, the melting temperature of the oligonucleotide was measured on the TTK as 63.8 ± 0.2˚C. Meanwhile with 100% of the Mg^{2+} ions in the reaction, the Tm value was 66.6 ± 0.1˚C. These results suggest that a drastic 100% change in salt concentration in the on-chip MCA reaction only results in a Tm increase of 2.8˚C. This is only half of the observed 6˚C offset in on-chip Tm values. In addition, efforts were taken during on-chip MCA experiments to eliminate potential sources of variation in salt concentration. One plausible mechanism for changes in salt concentration on the microchip include increased salt concentration due to evaporation of samples when they are pipetted onto the microchip. However, when performing standalone on-chip MCA experiments, the sample was inspected prior to the run to ensure that no significant evaporation loss was observed. Tubes that contained less than 95% of the expected volume of PCR product were not used during on-chip MCA reactions. These procedures ensured that evaporation was ruled out during on-chip MCA experiments.

The empirical measurement of the effect of Mg^{2+} concentration on TTK Tm values, revealed that even a drastic 100% reduction in the amount of salt in the reaction only leads to a 3˚C increase in Tm. This measurement strongly suggests that variations in salt concentration alone do not account for the 6˚C offset between TTK and Lightcycler melting temperatures. In addition, there are no clear mechanisms for such a drastic shift in salt concentration of the master mix. Since on-chip MCA takes place in a closed chamber with a run-time of less than 10 minutes, a 100% change in salt concentration does not appear to be a plausible explanation for observed Tm offsets. This statement is made in light of efforts to prevent the use of samples with noticeable evaporation in tubes – while investigating the temperature offset, the volumes of PCR products were measured after amplification on the Lightcycler to ensure that there was no evaporation. As a result, variations in salt concentration were ruled out as a potential source of the Tm offset.

Dye effects

Another biochemical process that could account for the observed Tm offset is dye-induced temperature shifts. Adding LCgreen plus intercalating dye to a MCA reaction mix could potentially shift the measured melting temperature. The manufacturer's data sheet[9] for LCgreen plus specifies that the dye could move the Tm of PCR products by 1– 3˚C on conventional systems. It is recommended that users manually adjust their melting curve analysis parameters to account for observed temperature offsets.

---

[9] LCgreen plus Information Sheet, Idaho Tech, Salt Lake City, Utah, USA

To determine if the temperature offsets between TTK and Lightcycler Tm values were due to dye effects, on-chip and off-chip MCA results using LCgreen plus dye were compared. Much of the data analysis algorithms employed on the Lightcycler are proprietary; however, Wittwer *et al.* (2003) provide a general description of the normalization and superimposition of data from multiple experiments undertaken in the analysis of MCA data, but do not mention specific temperature corrections to account for the use of LCgreen in the instrument. In addition, Herrmann *et al.* (2006) describe a cross-platform MCA study comparing different instruments and dyes used for high resolution melting curve analysis. The authors used multiple dyes and instruments including the combination of LCgreen and the Lightcycler. Herrmann *et al.* (2006) state that all the operations carried out during data analysis were mathematical and did not involve any "manipulation of the data" with respect to the temperature axis. In addition, off-chip MCA experiments performed by Dr. B. Taylor on the Lightcycler did not have any special temperature corrections to account for dye effects. This strongly suggests that dye-induced temperature shifts do not account for the measured 6˚C Tm offset between the TTK and the Lightcycler – since the Lightcycler data analysis does not make corrections for properties of the LCgreen dye.

5.3.2 Hardware

TTK hardware, in particular electronic components for temperature sensing and control, contribute to on-chip Tm measurements during MCA reactions. Errors in the design and/or calibration of the TTK instrument and microchips are also potential sources of error in Tm measurement. The TTk and microchips were calibrated as described in chapter 4. When the temperature offset between the TTK and Lightcycler was recorded, measurements were carried out with thermochromic liquid crystals (TLCs) to ensure that the system's behaviour still agreed with theoretical expectations.

TLC measurements using MCA GUI

TLC chips used for TTK temperature testing were prepared during the Festival of Calibrations and tested as described in chapter 4. Thermal properties of the TLC-filled microchips were verified by heating them in a water bath (HAAKE Phoenix II PI circulator, Thermo Electron Corp., Waltham, MA, USA) and recording the temperature at which the temperature transition was observed. Data gathered from the TLC chips was corrected to account for differences between the thermal properties of water and TLCs, as well as the thickness of TLCs within the PCR chamber (which leaves an air gap in the PCR chamber) as summarized by J.Martinez-Quijada in his report titled "Effect of filling the PCR chamber in PCR-4 with water, oil, TLC, and air on TLC measurements" which is provided in the supplementary information CD.

J.Martinez-Quijada performed steady state analysis of a 3-dimensional finite element model of the PCR-CE-4 microchip. He estimated a 70-μm air gap in the PCR chamber based on measurements by Dr.M.Behnam. The simulation predicted a spatial non-uniformity in temperature with the top of the microchip (which is farthest from the heater being the coldest) while the bottom of the microchip (closest to the heater) being the hottest. The simulation estimated that there was an average temperature difference of 3.95°C between microchips with 70-μm air gaps and those filled entirely with TLCs. Correction factors derived from this simulation were applied to TLC measurements from the TTK as described in J.Martinez-Quijada's report.

The procedure for TLC tests with the MCA GUI is described below. The experiments were carried out in a dark room at the AML with all room lighting turned off to reduce noise effects. I designed and performed these experiments with assistance from S.Caverhill-Godskewitch and S.Groendahl.

1. Open MCA tab in TTK GUI. Enter start and stop temperatures and ramp rate. For 58°C TLC chip (#0811C20) T_{start} = 50°C and T_{stop} = 70°C, for 70°C TLC chip (#0811C8) T_{start} = 60°C and T_{stop} = 80°C, and for 94°C T_{start} = 85°C and T_{stop} = 95°C (#0904C3) with a ramp rate of 0.05°C/s in all three cases. I only tested a 10°C range for the 94°C TLC because of current safety limits on the TTK when the PCR chamber exceeds 95°C.
2. Capture images of the TLC chip's fluorescence spectrum every 20s using the OOIBase32 software that accompanied the Ocean optics spectrometer with LS-1 tungsten halogen light source (Ocean Optics, FL, USA). The TLC transition temperature was defined as the temperature at which the maximum value of red/green TLC spectral peaks was obtained as illustrated in figure 4.1.
3. After capturing the spectra, I examined each of the data sets captured (every 20s seconds) to determine at what time the TLC colour transition occurred. Then I determined the transition temperature by looking up the PCR chamber temperature in the MCA report file (automatically generated by the TTK GUI) corresponding to the transition time.

I estimated the uncertainty in these TLC measurements as ± 0.25°C. Errors from timing with a stop watch were small – the electronic stop watch used during these experiments had an accuracy of 0.1 s. However, act of capturing data from the spectrometer software screen required an operator reaction time of up to 5 s. I estimated this uncertainty in synchronizing data capture from the spectrometer with time intervals on the stopwatch as ± 5 seconds by measuring the average reaction time over 10 data capture events. When heating at 0.05°C/s, this corresponds to an uncertainty of ± 0.25°C in each measurement.

Using the procedure outlined above, I measured TLC transition temperatures of 59.2°C, 64.7°C, and 87.8°C from TLC chips which had provided earlier temperature measurements of 58.4°C, 70.4°C, and 93.6°C respectively on the water bath during the Festival of Calibrations. These results are summarized in table 5.3 and indicate that when the TTK was heated with the MCA graphical user interface, the 6°C temperature offset (also seen during on-chip MCA experiments) is observed. These TLC measurements confirm that the system is operating ~6°C warmer than conventional systems; however, they do not tell us if the problem arose from hardware anomalies, improper thermal calibration, erroneous data analysis, or firmware glitches.

Table 5.3: Summary of TLC transition temperatures on Angelina when heating with MCA firmware after festival of calibrations. I obtained temperature offsets of ΔT = -0.8˚C at 58˚C, ΔT = 5.7˚C at 70˚C, and ΔT = 5.8˚C at 94˚C

TLC chip	TTK with MCA ramp (± 0.25˚C)	Water bath (± 0.2˚C)	Temp offset ΔT (˚C)
0811C20	59.2	58.4	-0.8
0811C8	64.7	70.4	5.7
0904C3	87.8	93.6	5.8

TLC measurements with PCR GUI

To narrow down the range of plausible hypotheses, I repeated the TLC measurements but heated the PCR chamber with the PCR GUI. If PCR heating did not provide a temperature offset then I could narrow down the Tm shifts to a software or firmware issue specific to the MCA GUI. I used the same microchips employed in MCA tests described above. I also kept all other variables constant except for temperature control with the PCR GUI rather than the MCA GUI. The procedure for the TLC temperature measurements with the PCR was as follows:

1. For each TLC-filled chip, set desired PCR chamber temperature in 1˚C increments over the same 50 – 70˚C, 60 – 80˚C, and 85 – 95˚C temperature ranges that were used during MCA heating, holding for 60s at each step.
2. Record TLC spectra 45 s into each step of the PCR reaction to account for additional hold times built into PCR firmware and to ensure that the system's temperature was at equilibrium when the spectrum was acquired. I determined that this was sufficient time for the system to stabilize at its temperature set point based on visual observations of the TLC spectrum settling time (< 2s).
3. After capturing the spectra, I examined each of the data sets captured (in 1˚C increment) to determine the temperature at which the TLC colour transition occurred (i.e. maximum value of red/green spectral peaks).

I estimate a minimum error of ± 0.5˚C in TLC measurements with the PCR GUI. In this case, timing was not the primary source of error. Instead, the 0.5˚C error arises from the fact that the PCR GUI accepts temperature settings and then rounds them to the nearest degree. This limits PCR temperature accuracy to at least ± 0.5˚C. TLC temperature measurements with the PCR GUI did not show the 6˚C temperature offset (see table 5.4). For the 58˚C-rated TLC chip, the measured transition temperature was 59.2˚C compared with the expected 58.4˚C obtained on the water bath (only a different of 0.8˚C). Similarly, for the 70˚C- and 94˚C-rated TLCs, temperature differences of 1.6˚C and 0.1˚C were measured. This means

Table 5.4: Comparison of TLC transition temperature when heating was performed with the water bath, with the MCA ramp algorithm, and the PCR hold algorithm. I measured a 6°C temperature offset at 70°C and 94°C set-points with the MCA temperature ramp but not with the PCR heating algorithm.

Water bath (± 0.2°C)	TTK with MCA ramp (± 0.25 °C)	TTK with PCR hold (± 0.5°C)
58.4	59.2	58
70.4	64.7	72
93.6	87.8	93–94

that when heating was performed with the PCR GUI, an average temperature difference of 1.3 ± 0.5°C was observed between the TTK and conventional instruments.

This data strongly suggests that our thermal calibration procedures are adequate for PCR temperature control. In addition, since the same system hardware is used for both PCR and MCA, then TTK hardware can be eliminated as a potential source of the measured Tm offset since the system hardware has no way of distinguishing between PCR and MCA procedures. In fact, the same microchip and system calibration processes are employed prior to PCR and MCA work. Consequently, any difference between the results of PCR and MCA heating must be due to an anomaly specific to on-chip MCA and arising from either the software or the firmware.

5.3.3 Software

The TTK's software is comprised mostly of the graphical user interface that receives user commands and automatically generates run reports for on-chip processes. The user interface operates as a front-end for activities carried out by the TTK's microcontroller unit. The firmware receives user commands and passes them directly to the firmware. The software merely formats the user's commands to meet syntax requirements for firmware operation – and does not make other changes to the user's input. The PCR and MCA GUIs are separate tabs of the same graphical user interface (designed by A.Bidulock) to control TTK operations and automatically generate run reports. The GUI operates as a front end with text boxes for entry of the run parameters by the operator. The TTK GUI also automatically generates run reports to ensure that all experimental data is documented in a consistent and scientific manner. Both the PCR GUI and the MCA GUI send commands to the firmware to implement either PCR or MCA temperature control actions. The fundamental difference between the PCR and MCA graphical user interfaces is that they send different firmware commands to the TTK's microcontroller unit.

To determine if the software introduces errors that might account for the Tm offset during on-chip MCA, I by-passed the software entirely – sending commands directly to the firmware via a command line interface. I sent commands directly from the command line using the firmware command "TM(start-temp, stop-temp, ramp-rate)" as described in the command line specifications document in the supplementary information (see the file named "CLI v2.7.pdf"). However, even with a command line interface (i.e. no interaction with TTK software), I still obtained the temperature offset when performing MCA. This strongly suggested that the Tm offset was directly related to the MCA firmware.

5.3.4 Firmware

As described in the previous sections, I tested and eliminated biochemical processes, hardware, and software as potential explanations for the TTK temperature offset. Subsequently, I inspected the TTK firmware for errors that could explain the observed temperature difference between on-chip and off-chip systems. I examined the MCA firmware to check for logical or typographical errors that might explain the observed temperature offset. As described in figure 5.1, the firmware accepts the start and stop temperatures (T_{start} and T_{stop}) as well as the ramp rate from the user. Then using the chamber to heater temperature algorithm, the firmware calculates heater temperatures that correspond to T_{start} and T_{stop}. Then the heater temperature for the start temperature is passed to the PI controller. The system waits at T_{start} for 15s then enters a timed loop to increment temperature values steadily at the ramp rate from the MCA start temperature until the stop temperature. The entire source code for the MCA firmware is provided in the supplementary information CD that accompanies this thesis.

While inspecting the MCA firmware, I did not find a clear logical error or mechanism to account for the observed 6˚C temperature offset between the TTK and lightcycler. However, I found that data obtained in March 2010 (prior to the Festival of Calibrations) did not show a 6˚C temperature offset between TTK and Lightcycler. The data from an extensive MCA experiment with 15 samples and 3 runs per sample is summarized in table 5.5 and shows that TTK and Lightcycler results only differed by 1– 2˚C in March 2010.

Table 5.5: Summary of melting temperatures measured on Angelina and the Lightcycler prior to the Festival of Calibrations. Lightcycler Tm values were obtained using $1x10^6$ copies/μL of each sample on April 21 2010. Unlike experiments carried out in July – September 2010, the on-chip results presented here do not show a 6˚C difference from Lightcycler values – instead a maximum difference of 2˚C was measured. This suggests that a change to the system during or after the Festival of Calibrations is responsible for the measured Tm offset. Raw data is provided in a MS Excel® document tiled "Angelina malaria melt data March 2010" in the supplementary information CD.

Sample	Average TTK Tm (± 0.1˚C)	Average Lightcycler Tm (± 0.1˚C)	ΔTm (˚C)
P.falciparum	87.0	87.2	0.2
P.malariae	77.0	76.0	-1
P.ovale	84.0	83.2	-0.8
P.vivax	82.3	80.4	-1.9
		Average	-0.9

This differs significantly from more recent results obtained between July and September 2010 (after the Festival of Calibrations) that showed a 6 – 8˚C difference between TTK and Lightcycler temperatures (see table 5.2). The data set obtained prior to the Festival of Calibrations provided a clue to the origin of the temperature offset. In fact, it strongly suggested that a change to the system during or after the Festival of Calibrations was the source of the temperature offset. Having considered biochemical, hardware, and software mechanisms for the temperature offset, I explored the major changes made to do the TTK firmware during the Festival of Calibrations.

The main loop of the MCA firmware was not changed during the Festival of Calibrations. I compared the MCA firmware main loop ("tm.c" file) before and after the Festival of Calibrations (also available in the supplementary information) and there were no logical or typographical differences. This rules out the main loop of the MCA firmware as a plausible source of the temperature offset. However, I did find changes in the "heater.c" file, the major subroutine that the MCA firmware refers to when updating PCR chamber temperatures. The two significant changes made to the "heater.c" file during the Festival of Calibrations were:

1. **T_c - T_h - T_{hs} mapping function**: a new empirical relationship between the PCR chamber temperature, T_c, the heater temperature, T_h, and the heat sink temperature, T_{hs} was developed. As discussed in chapter 4.2.1, the switch to a new empirical relationship between T_c, T_h, and T_{hs} improved temperature accuracy by accounting for variations in heat sink temperature as well as differences between the thermal properties of TLCs and PCR reaction mix.

2. **PI controller redesign**: a faster PI controller was designed by Dr.R.Johnstone to reduce PCR run times from 1.75 hours to 1 hour (for a typical ß2m reaction). This was accomplished by tuning the P and I parameters used for closed-loop temperature control in the PI controller. Dr Johnstone's tuning appeared to increase the speed of operation of the PI controller by tracking setpoints within the feedback loop and anticipating the final value. A PI control algorithm is a feedback loop used to minimize the error between a measured value and a desired setpoint (Misir *et al.*, 1996). In this case, the measured value is the PCR chamber temperature while the desired set point is entered by the user and passed to the MCA firmware. The proportional gain, K_p, is the parameter of the controller that is related to the present error between the current measured value and the setpoint, while the integral gain, K_i, is the parameter related to accumulated errors during past iterations of the feedback loop. The proportional gain K_p is multiplied by the present error in the feedback loop, while the integral gain K_i is multiplied by the accumulated error (or error sum) in the feedback loop. Tuning the values of the K_p and K_i terms either manually by an experienced engineer or algorithmically allows the minimization of the error between the setpoint and the measured value, as well as the control of other variables such as system time constant (Misir *et al.*, 1996).

To determine which of these changes was responsible for the 6°C offset, I compared the old and new PI controllers by reprogramming the TTK with the old firmware (version 220) that was used before the Festival of Calibrations. The pre-festival versions (version 220) of the PI controller and the temperature mapping function are provided in the “heater.c” file found in the “Firmware version 220” folder in the supplementary information CD. On the other hand, the post-festival versions (version 300) of the PI controller and the temperature mapping function are provided in the “heater.c” file in the “Firmware version 300” folder in the supplementary information CD.

Reprogramming the TTK eliminated Tm offset

To compare old and new PI controllers, I re-programmed the TTK with its old firmware (version 220) from March 2010. To ensure that I was only testing one variable at a time, I replaced the old temperature mapping function with the new post-festival equation. I found that when firmware version 220 was reprogrammed onto the system, on-chip MCA results were in agreement with the data provided in table 5.5. This confirmed that a firmware error was responsible for the Tm offset.

As a follow-up test, I reprogrammed the system with firmware version 300 to reproduce the 6˚C offset and obtain new measurements for comparison with version 220. However, when the system was reprogrammed with firmware version 300, I no longer measured the 6˚C temperature offset. Instead, I recorded a TLC transition temperature of 69.8 ± 0.1˚C for the 70.4˚C-rated TLC chip (#0811C8), and 91.6˚C for the 93.6˚C-rated TLC chip (#0904C3). These measurements were the average temperature (± standard deviation) over 2 consecutive experiments with the same microchip. Both microchips had been used for on-chip MCA experiments before and gave the previous measurements of 64.7˚C and 87.8˚C prior to re-programming the TTK as summarized in table 5.2.

This was very puzzling as it suggested that the source of the temperature offset had been fixed. However, there was no noticeable difference in the system, other than the act of reprogramming it. I checked the firmware repository – a version control system on the “Kawaii” PC in the AML that contains all previous versions of the TTK firmware – and made sure that I was using the proper edition of the TTK firmware. I also made sure that there were no physical or protocol differences while carrying out my measurements. Nevertheless, I was unable to reproduce the 6˚C temperature offset even when all conditions were changed to reflect the experimental settings described in section 5.3.2. This suggested that I had eliminated the temperature offset by reprogramming the system with firmware version 300 while keeping all other variables the same (data from 2 different TLC measurements is provided in the following section).

There are only a few remaining logical explanations for the Tm offset based on the available data. First, it is plausible that there was an error in MCA firmware version 300 when it was originally loaded onto the TTK. Since re-programming the TTK with firmware version 300 eliminated the temperature offset, it is feasible that there was an error in the original version of the firmware when it was loaded onto the TTK. Firmware corruption is one mechanism that could potentially explain the elimination of the temperature offset by reloading the system with its firmware. Firmware corruption could explain anomalous behaviour – however, it seems an unlikely means for a consistent temperature offset. Nevertheless, reprogramming the TTK would get rid of any errors or corruption in the firmware so that reloading the TTK with version 300 (supposedly the same version that was on the system since July 2010) eliminated the temperature offset.

Another plausible explanation is a typographical error in the TTK firmware. However, when I checked the firmware repository, I did not find any errors. This suggests that if a firmware error was the source of the temperature offset, it must have been in a version of the firmware that was not saved in the firmware repository. This could arise as a result of unsaved error introduced during firmware testing (that was not properly saved in the repository) around the time of the Festival of Calibrations. I investigated this hypothesis to identify the time such a change could have occurred; however, complete instrument log books of changes were not kept until after the Festival of Calibrations – at which point the 6˚C offset was already in place.

This confusing situation could have been resolved earlier by quickly testing the firmware every time the system was reprogrammed. Nevertheless, the inability to reproduce the 6˚C offset after reloading the TTK with firmware strongly suggests that the problem was a one-time glitch associated with the firmware possibly due to a typographical error or corruption in the firmware. In addition, I am convinced that problem has been fixed because all experiments performed on the TTK after reprogramming the firmware (and keeping all other variables the same) have given temperature measurements that are within 1-2˚C of the target. As described earlier, measurements on the microchip #0811C8, which gave a TLC transition temperature of 70.4˚C on the water bath, gave a transition temperature of 69.8 ± 0.1˚C on the TTK. Raw data for this experiment is provided in the MS Excel® file titled "Dec 13 TLC test" in the "6C offset data" folder of the supplementary information CD.

5.4 Closing remarks

This chapter focused on the implementation of MCA on a portable and inexpensive lab on a chip platform. MCA is a post-PCR process that can be used as an indirect assay to distinguish PCR products according to their size and base sequence (Kubista *et al.*, 2006). MCA implementation on the TTK was designed to allow the transfer of existing molecular biology protocols from conventional systems directly to the TTK.

As described in chapter 4, the original optical detection hardware for MCA was designed by M.Behnam & G.Kaigala. My contributions to the engineering of the MCA subsystem were focused on:

- collaborating with Dr. R.Johnstone to write and test the MCA heating algorithm,
- performing initial proof of principle tests of MCA with ß2m genomic DNA,
- developing an algorithm for sorting, smoothing, and analyzing MCA data,

- and investigating the 6˚C difference between TTK and Lightcycler melting temperatures.

First, I performed on-chip MCA with the on-chip PCR product from amplification of ß2m genomic DNA. I obtained a clear melting peak with a Tm value of 79.2 ± 0.6˚C. I sorted MCA images according to the temperature at which they were acquired by identifying the images at the start and stop temperatures of MCA – where the LED turns on and off.

Next, I investigated the origin of noise in the MCA data. I found that noise spikes were present in fluorescence data even during the predenaturation step, when the LED is turned off and the CCD camera is sealed from background light. After investigating properties of the Meade DSI camera, I found that it is recommended that the camera be operated at room temperature with additional images acquired for noise correction. The manufacturer also mentioned that the noise level in the camera changes with temperature – and implemented a built-in temperature sensor into newer versions of the deep sky imager camera. These findings indicated that the noise spikes in MCA data were as a result of noise inherent in the CCD readout (especially at temperatures much higher than its recommended operating conditions).

I smoothed MCA data by applying a median filter to remove outliers then a moving average filter to smooth the signal. I set the width of the smoothing window to the number of data points that would corresponding to a width of 3˚C (depending on the number of data points acquired during the on-chip MCA experiment). I set this restriction so that smoothing the signal did not degrade melting curves to the point that adjacent melting peaks could not be distinguished[10].

After finalizing the MCA data analysis algorithm, I performed on-chip MCA with *P.malariae* samples from on-chip and off-chip amplification. At this stage, on-chip experiments were performed by Dr. Behnam & Dr. Taylor, while I worked primarily in a data analysis role. On-chip MCA gave melting temperature values that were in agreement for on-chip and off-chip samples i.e. approximately the same melting temperature was observed on the TTK whether a sample was prepared on the TTK or on the Lightcycler.

However, when I compared the melting temperatures from the TTK with melting temperatures from the Lightcycler, I found that there was an average 6˚C difference between temperature measurements on both platforms. This offset did not depend on the origin of the sample being tested – PCR products prepared on the TTK and Lightcycler showed the temperature offset.

I led a troubleshooting effort to identify and eliminate the temperature offset. I examined the subsystems that affect on-chip Tm calculations. I examined the biological processes, hardware specifications, software commands, and firmware source code that contribute to on-chip Tm values. I found that keeping all other variables the same, reloading the TTK with its firmware eliminated the observed 6˚C temperature offset. This was puzzling because it indicated that keeping all other variables the same, the act of reprogramming the

---

[10] For our application of choice (the detection of malaria strains), adjacent melting peaks are separated by at least 3˚C.

TTK with its firmware eliminated the temperature offset.

Eliminating the temperature offset by reloading the TTK with its (apparently unchanged) firmware suggests that the error was likely a one-time glitch, possibly introduced by typographical error or firmware corruption. I inspected the AML's firmware repository for noticeable typographical or logical errors in the firmware but I did not find anything to account for the 6˚C offset. I also perused the instrument logbook to identify the origin of the error that could potentially be linked to a change made to the instrument; however, this did not yield helpful information because a detailed logbook was not kept until after the Festival of Calibrations – at which time the 6˚C temperature offset was already present.

In summary, the 6˚C temperature offset could have been detected and resolved earlier by keeping an accurate system log and testing all system modules after each update. This would ensure that there was a record of all changes made to the system and allow rapid identification of potential errors as soon as they occur.

After performing on-chip real time PCR and MCA with ß2m genomic DNA and *P.malariae*, the next step towards a fully-integrated medical diagnostic for point of care applications was to combine the sample preparation capability of the TTK (chapter 3) with real time PCR (chapter 4), and MCA (this chapter). Chapter 6 describes the combination of the SP, real time PCR, and MCA modules to purify, amplify, and analyze ß2m DNA from human buccal cells.

CHAPTER 6

Integration of SP, Real Time PCR, and MCA

6.1 Introduction

To achieve the goal of a portable and inexpensive lab on a chip system for point of care analysis, the SP, real time PCR, and MCA modules of the TTK must be integrated to permit analysis of raw clinical samples. Chapters 3, 4, and 5 describe the design and testing of the SP, real time PCR, and MCA modules on a standalone basis. This chapter describes a proof of principle integration of all 3 modules to purify, amplify, and analyze ß2m DNA from human buccal cells.

6.2 On-chip SP-PCR-MCA results

As described in chapter 2, each of the TTK's subsystems was designed as a modular unit that can be combined with the other subsystems for rapid testing. Three integrated SP-PCR-MCA experiments were performed on the TTK. The protocol for on-chip SP-PCR-MCA is an amalgam of each of the individual protocols detailed in earlier chapters and is summarized in the "TTK SPPCRCE Protocol v1.02" document in the supplementary information. In addition, a no-template control was performed with an aliquot of the same SP and PCR reagents to ensure that there was no contamination. The real time PCR data was analyzed with the algorithm described in chapter 4.3.2 to give the amplification curves shown in figure 6.1.

I calculated Ct values of 24.8 ± 0.6 cycles, 31.3 ± 0.5 cycles, 32.6 ± 0.7 cycles, and 33.7 ± 0.6 cycles for SP-PCR run 1, run 2, run 3, and the no template control respectively. These results are summarized in table 6.1. I observed that the amplification curve for SP-PCR experiment 1 was much stronger than that of experiments 2 and 3. Similarly, the Ct value

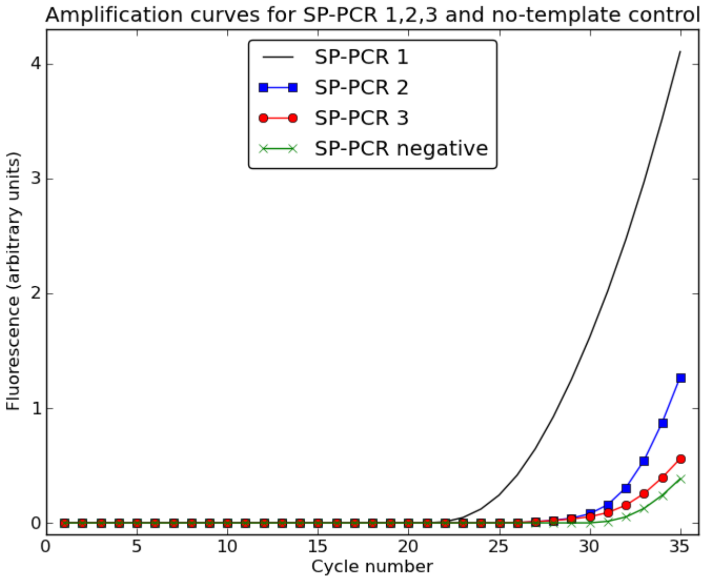

Figure 6.1: Amplification curves on-chip SP-PCR-MCA experiments with ß2m DNA from human buccal cells. Run 1 shows similar amplification as obtained with ß2m genomic DNA in chapter 5. Meanwhile runs 2 and 3 show very late amplification and are barely distinguishable from the no-template control.

obtained for run 1 (24.8 cycles) was much lower than that obtained for run 2 (31.3 cycles) and run 3 (32.6 cycles) which were barely distinguishable from the no-template control (33.7 cycles). Run 1 is in agreement with the amplification obtained with ß2m genomic DNA (Ct = 24.3 ± 0.9) in chapter 5. Meanwhile runs 2 and 3 show very late amplification and are barely distinguishable from the no-template control. A lower Ct value indicates greater amplification (Kubista *et al.*, 2006) suggesting that run 1 was more efficient that runs 2 and 3. I will provide a hypothesis for the difference in amplification between SP-PCR runs 1, 2, 3 in section 6.3.

Table 6.1: Summary of Ct values for on-chip SP-PCR experiments with ß2m DNA from human buccal cells. Ct values were calculated using the threshold method described by (Rutledge, 2004) and discussed in chapter 4.

Sample	**Ct (cycles)**
ß2m genomic DNA control (from chapter 4)	24.3 ± 0.9
SP-PCR-1	24.8 ± 0.6
SP-PCR-2	31.3 ± 0.5
SP-PCR-3	32.6 ± 0.7
No-template control	33.7 ± 0.6

6.2.1 Melt curves for on-chip SP-PCR-MCA experiments

Next, MCA was performed on the on-chip SP-PCR products to verify that there was PCR product available and that the DNA peaks appeared at the expected melting temperature for ß2m DNA. MCA was performed immediately after each on-chip SP-PCR experiment since MCA is carried out in the same reaction chamber as real time PCR. MCA data was analyzed and Tm values were calculated as described in chapter 5.

Melt curves for on-chip SP-PCR experiments 1, 2, 3 are shown in a combined graph in figure 6.2. As expected, SP-PCR run 1 showed a strong DNA melting peak with amplitude 0.20 ± 0.03 units at a Tm of 77.5 ± 0.2˚C. Similarly, SP-PCR run 2 had a melting peak amplitude of 0.06 ± 0.01 units at a melting temperature of 75.6 ± 0.2˚C, while run 3 had a melting peak amplitude of 0.03 ± 0.01 units at a temperature of 78.7 ± 0.3˚C. 3 consecutive MCA runs were performed each time to estimate the uncertainty in calculating the Tm value as the standard deviation in Tm.

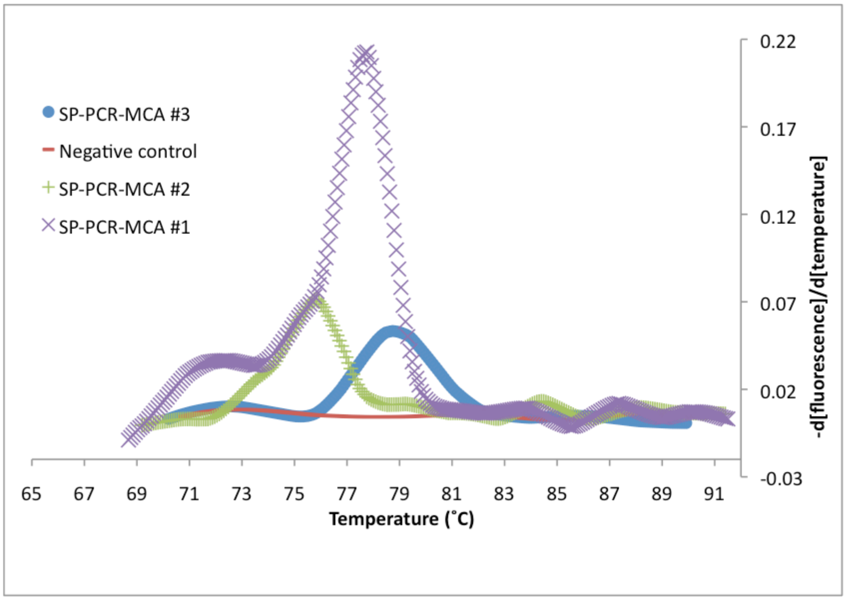

Figure 6.2: Melt curves for 3 on-chip SP-PCR-MCA experiments with ß2m DNA. Tm values of 77.5 ± 0.2˚C, 75.6 ± 0.2˚C, and 78.7 ± 0.3˚C were obtained for runs 1, 2 and 3 respectively. MCA analysis was repeated 3 times in a row for each sample and the uncertainty in Tm is estimated as the standard deviation of the Tm measurements over those 3 runs. SP-PCR run 1 shows the strongest peak intensity (in agreement with real time PCR amplification curves) and CE analysis. Hypotheses for the difference in PCR product strength are discussed in section 6.3.

On-chip Tm values are summarized in table 6.2. The SP-PCR no-template control did not show a melting peak suggesting that the PCR products observed in MCA analysis were not due to contamination. Although the MCA peak intensities for SP-PCR runs 2 and 3 are small, the PCR product peaks were reproducibly detected at the same Tm value over 3 consecutive MCA repetitions with standard deviations of 0.2˚C and 0.3˚C respectively.

Table 6.2: Summary of Tm values obtained for on-chip SP-PCR-MCA experiments with ß2m DNA from human buccal cells. Tm values were defined as the position of the maximum signal in the negative first derivative versus temperature graph. Uncertainty in temperature is defined as the standard deviation in Tm across 3 consecutive MCA runs.

Sample	Tm (°C)	Peak amplitude (arb.units)
SP-PCR run 1	77.5 ± 0.2	0.20 ± 0.03
SP-PCR run 2	75.6 ± 0.2	0.06 ± 0.01
SP-PCR run 3	78.7 ± 0.3	0.03 ± 0.01

6.2.2 Verification and quantitation of SP-PCR-MCA results with capillary electrophoresis

One of the objectives of real time amplification curves is to permit quantification of the initial DNA copy number in the test sample (Kubista *et al.*, 2006). This can provide useful diagnostic information such as the number of malaria parasites in a blood sample (de Monbrison *et al.*, 2003). Quantification of real time PCR data can be performed using either absolute or relative methods involving well-characterized DNA standards as described in chapter 1. During this proof of principle test, relative/absolute quantification was not performed. However, to provide an initial estimate of the amount of DNA present in the PCR product, CE analysis was performed on the μTK. This provided additional verification of the identity of the PCR products. This is discussed in detail in the following section.

To quantify how much PCR product was generated during each on-chip SP-PCR experiment, capillary electrophoresis was performed on a commercial microchip-based system (μTK, Micralyne, Edmonton, AB, Canada). This allows comparison of real time PCR amplification curves with PCR product detection by CE. This additional data will allow judgements about the strength of the on-chip PCR reaction (in terms of the amount of PCR product after on-chip real time PCR). In addition, performing CE will enable an initial estimate of the sensitivity of the on-chip real time PCR optical detection system. Dr.M.Behnam performed microchip CE on the μTK following the SP-PCR-CE protocol provided in the supplementary information. CE can be used to estimate the size (in base pairs) and the amount (in ng/μL) of PCR product provided the sensitivity and resolution of the instrument has been calibrated with DNA standards. The sensitivity and resolution of the μTK was estimated by our research group as described in Kaigala *et al.* (2010).

Electropherograms for on-chip SP-PCR experiments 1, 2, and 3 are provided in figures 6.3, 6.4, and 6.5 respectively. Also, the electropherogram for the no-template control is shown in figure 6.6. On-chip SP-PCR runs 1, 2, and 3 also show a PCR product during CE analysis – while the no template control does not show a peak (indicating the absence of contamination). The position of the ß2m peak agrees with the expected position of the ß2m PCR product peak based on CE experiments performed with DNA size standards (documented in Kaigala *et al.* (2008)). Consequently, although the amplification curves for runs 2 and 3 do not show significant fluorescence signals above the background signal level, the presence of PCR product (albeit in small amounts) was confirmed by CE analysis. I will discuss potential explanations for the difference in peak strengths between SP-PCR runs 1, 2, and 3 in section 6.3.

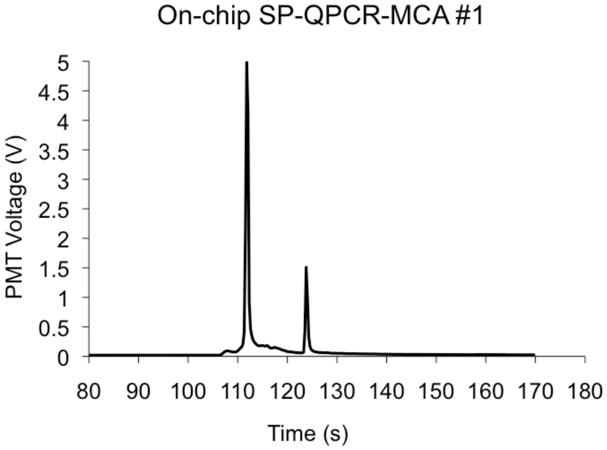

Figure 6.3: Electropherogram for on-chip SP-PCR run 1 with ß2m DNA from human buccal cells. CE was performed on the μTK by Dr.M.Behnam according to the SP-PCR-CE protocol provided in supplementary information. The amplification curve for this experiment showed strong fluorescence above background levels (see figure 6.1). As expected, a strong PCR product peak (amplitude 1.520 ± 0.030 V) was observed with a photomultiplier tube gain of 0.7 on the μTK

On-chip SP-PCR run 1 has a CE peak of amplitude 1.520 ± 0.030 V at a photomultiplier tube gain of 0.7, following the CE protocol laid out in SP-PCR-CE protocol in the supplementary information. The uncertainty in the peak height was estimated as the baseline signal level on the left side of the CE primer peak. SP-PCR runs 2 and 3 also showed PCR product peaks of amplitude 0.083 ± 0.030 V and 0.081 ± 0.030 V. The stronger CE peak observed for run 1 agrees with the results of the amplification curves shown in figure 6.1, where there is a clear fluorescence increase above the baseline in run 1, while runs 2 and 3 are barely distinguishable from the no-template control.

To check that the PCR product peaks observed for runs 2 and 3 were not due to contamination, CE analysis was also performed on the no-template control with identical run conditions.No PCR product peak was observed suggesting that there was no contamination during the SP-PCR experiments.

In Kaigala *et al.* (2010), our research group estimated the sensitivity of the μTK as approximately 14 ± 2 $\frac{mV-\mu L}{ng}$ for singly-labeled BK Virus PCR product (~250 bp in length) when the photomultiplier tube gain is set to 0.7. I used the sensitivity of the μTK determined using the BK virus to estimate since both the ß2m amplicon is nearly the same length (236 bp) and the primers were end-labeled with the same fluorophore (Alexa 647) that was used when analyzing BKV. Using the estimate for the sensitivity of the CE system provided in Kaigala *et al.* (2010), I calculated that SP-PCR run 1 with a peak amplitude of 1.52 ± 0.03 V had a PCR product concentration of approximately 108.9 ± 2.1 ng/μL. Similarly, I estimated the

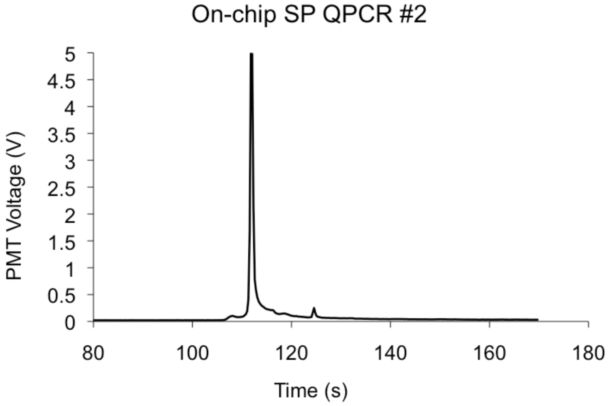

Figure 6.4: Electropherogram for on-chip SP-PCR run 2 with ß2m DNA from human buccal cells. The amplification curve for SP-PCR run 2 did not show significant fluorescence above background levels (see figure 6.1) and was barely distinguishable from the no-template control. A weak PCR product was observed (amplitude 0.083 ± 0.030 V) during CE on the μTK with a photomultiplier tube gain of 0.7. Although the CE peak was small, it still appeared in the same position as in run 1 where there is a clear ß2m PCR product. This suggests that SP-PCR run 2 produced the ß2m amplicon albeit in very small quantities. I will provide an estimate of the PCR product concentration later in section 6.2.2.

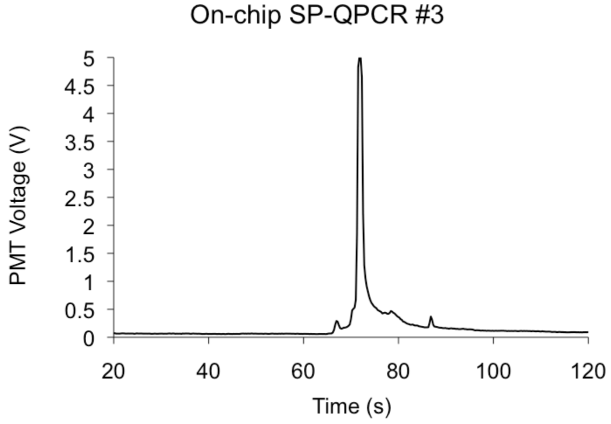

Figure 6.5: Electropherogram for on-chip SP-PCR run 3 with ß2m DNA from human buccal cells. CE was performed on the μTK according to SP-PCR-CE protocol provided in supplementary information. A primer peak and a PCR product peak (amplitude 0.083 ± 0.030 V) were observed with a photomultiplier tube gain of 0.7

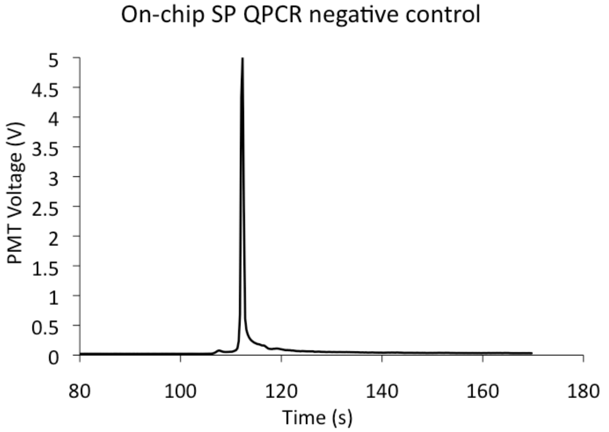

Figure 6.6: Electropherogram for SP-PCR no-template control. Only a primer peak was observed using the same CE run conditions as in SP-PCR runs 1, 2, and 3. This indicates that the peaks from the test samples in runs 1, 2, and 3 are not a result of contamination.

PCR product concentrations from the electropherograms of runs 2 and 3 as 5.9 ± 2.1 ng/μL and 5.8 ± 2.1 ng/μL respectively. Potential explanations for the variation in peak strengths of runs 1, 2, and 3 will be explored in section 6.3.

6.3 Discussion

6.3.1 Variations in PCR product peak intensity

Table 6.2 shows that the PCR product peak intensity as measured by MCA analysis follow the same pattern as the real time PCR amplification curves in figure 6.1 and the CE analysis in section 6.2.2. SP-PCR run 1 has a peak amplitude that is 3 times greater than the amplitude of run 2, and 6 times greater than the amplitude of run 3. These differences may be explained by variations during the on-chip SP process.

When preparing the SP lysate mix as described in chapter 3.3.2, buccal cells were collected with cotton swabs. As described in chapter 3, the current protocol for on-chip SP-PCR calls for the preparation of a fresh lysate for each experiment. Although the cells were collected from the same volunteer to reduce run to run variations, it was difficult to ensure that the same number of cells were extracted each time. For example, during on-chip SP-PCR runs 2 and 3, there was noticeable bead clumping while preparing the SP lysate mix. This was because cotton strands had floated into the SP mixture and clumped to magnetic beads, reducing the amount of beads available to bind DNA in solution. The SP lysate mixture for SP-PCR runs 2 and 3 (where clumping occurred) had a visibly lighter colour when compared to SP-PCR run 1. After on-chip SP, the size of the bead pellet recovered at the SP output well for runs 2 and 3 (and passed on to the PCR chamber) was about 3 times smaller (estimate based on observation by eye) than in run 1.

In retrospect, it is clear that the significant differences while preparing on-chip SP-PCR reactions 2 and 3 should have resulted in the institution of a clear protocol to prevent the use of such samples to reduce variations in on-chip SP-PCR results. A focus on improving the reproducibility of the SP step would significantly decrease the variation in the amount of DNA in the reaction, leading to greater consistency in MCA results. Approaches to improve the reproducibility of the SP protocol are described in chapter 7.2.

6.3.2 Variations in PCR product peak position

In addition, table 6.2 shows that there were variations in the Tm values of the on-chip SP-PCR-MCA experiments. Run 1 had a Tm value of 77.5 ± 0.2°C, run 2 had a Tm of 75.6 ± 0.2°C, while run 3 had a Tm of 78.7 ± 0.3°C. A plausible hypothesis for the difference between the Tm values of the on-chip SP-PCR experiments is variations in reaction salinity and pH as a result of incomplete removal of STW buffer from the magnetic beads during on-chip SP. The SP protocol (in chapter 3.3.3) calls for manual removal of "sucrose-tween-wash" (STW) buffer from the PCR input well with a micropipetter. This manual handling step is not 100% efficient and very often small volumes of STW buffer are left behind in the SP output well. Even if only 0.5 μL of STW is left in the 5 μL well, it could still contribute to a 10% by volume effect on the pH or salinity of the PCR mixture that is added to the SP output well. Such variations in salinity or pH could adversely affect the melting temperature of PCR products obtained.

With the current microchip design, manual removal of STW was necessary because the SP input and output wells were designed to be filled manually. Approaches to eliminate the need for this manual pipetting step are currently under investigation at the AML. A new microchip design might be required to permit automated and efficient separation of SP and PCR reagents.

6.4 Closing remarks

This chapter described the combination of SP, real time PCR, and MCA on the TTK to amplify ß2m DNA from human buccal cells. 3 proof of principle demonstrations of integrated SP-PCR-MCA and 1 no-template control were carried out on the TTK. Samples were analyzed by on-chip real time PCR and MCA. The results were verified and quantitated with CE in a commercial system (μTK).

Real time amplification curves showed that SP-PCR reaction 1 produced very similar amplification levels to the ß2m genomic DNA control described in chapter 4 suggesting successful integration of SP with real time PCR. However, SP-PCR reactions 2 and 3 showed weak amplification that was barely distinguishable from the no-template control.

This difference in amplification levels may be attributed to different starting amounts of buccal cells in the SP reaction. Noticeably smaller amounts of magnetic beads were present after completion of on-chip SP in experiments 2 and 3 because of beads clumping to loose fibres from the cotton swabs used to extract buccal cells. I propose remedies to eliminate this variation in starting DNA concentration in chapter 7.

The PCR products from all 3 SP-PCR experiments were analyzed by on-chip MCA. In addition, the PCR products were quantitated on the μTK, a commercial CE system that was previously characterized with DNA size standards to determine the length and concentration of the amplicons (Kaigala *et al.*, 2010). PCR product peaks were observed in both MCA and CE analyses of experiments 1, 2, and 3. As expected, run 1 showed the strongest signal strength in both CE and MCA. However, weak yet repeatable peaks were observed for SP-PCR experiments 2 and 3 respectively. Furthermore, CE and MCA analysis of the no-template control did not show any PCR product peak, suggesting that the positive results observed were not due to contamination.

Next, I estimated the PCR product concentrations from runs 1, 2, and 3 as 108.9 ± 2.1 ng/μL, 5.9 ± 2.1 ng/μL, and 5.8 ± 2.1 ng/μL by measuring the height of PCR product peaks in electropherograms obtained by Dr. Behnam on the μTK. I calculated these values using estimates of the sensitivity of the μTK derived in past work by our research group (Kaigala *et al.* (2010)).

In summary, the combination of sample preparation, real time PCR, and MCA on the TTK allowed the extraction of ß2m DNA from a raw clinical sample in a single microchip-based instrument. Using the knowledge gained from this initial demonstration, our laboratory will develop new protocols and microchip designs to eliminate variability in the SP-PCR-MCA process and permit fully-automated operation of the system. On-chip real time PCR and MCA were performed with *P.malariae* in chapters 4 and 5. Those efforts could provide ground work towards a demonstration of SP-PCR-MCA with a more clinically-relevant sample (malaria) starting from whole blood. In the following chapter, I will summarize the work described in this thesis and propose future work to improve the TTK.

CHAPTER 7

Future Work and Conclusions

This thesis describes my contributions to the development and testing of a modular and inexpensive SP-PCR-MCA instrument at the AML. In this chapter, I will explore areas for improving the SP, real time PCR, and MCA modules of the TTK based on findings from earlier chapters. I will also provide a summary of the projects embarked on and the results obtained.

7.1 Summary

In chapter 2, I provided an overview of the status of the TTK at the time I joined the AML as an undergraduate student. Although the TTK represented the state of the art in portable and inexpensive medical diagnostics at that time (Kaigala *et al.*, 2008), it was not yet ready for point of care applications because it could not process raw clinical samples.

To tackle this fundamental problem, I integrated an automated sample preparation (SP) module with the TTK to permit on-chip DNA purification followed by downstream amplification and analysis. The development of the SP module started while I was an undergraduate student, but it was not integrated with the TTK until I joined the research group as a Master's student.

Chapter 3 discussed the integration of the SP module with the TTK and the testing of on-chip SP on a standalone basis. The custom-designed X-Y stage was attached to a permanent magnet with micrometer-precision in the vertical and horizontal directions. The automated SP stage orchestrated the motion of Chargeswitch® magnetic beads which bind to DNA in low pH conditions and release DNA in high pH conditions. Initial testing of the SP module included failures due to degradation of the Proteinase K enzyme (required to lyse cells during SP) because of exposure to multiple freeze-thaw cycles. This was remedied by ordering a new batch of Proteinase K and implementing new protocols that required small, single-use aliquots of the enzyme to be stored at -30˚C.

In addition, no-template controls for on-chip SP regularly (42% of the time) showed PCR product peaks. These failed controls appeared not only in on-chip experiments but also in tube-based runs to test the purity of the reagents. The contaminating peak in the no-template control was most likely ß2m DNA since it had the same PCR product length as ß2m DNA when CE analysis was carried out on the μTK. The contamination problem was exacerbated by the fact that existing protocols in our laboratory did not call for a no-template controls along with every experiment. After overcoming reagent and contamination problems with strict protocol changes, standalone testing of the SP module was completed. 3 successive on-chip SP experiments were performed followed by off-chip amplification in a conventional thermal cycler and CE detection in the μTK. All three experiments showed strong PCR product peaks with no contamination in the accompanying no-template controls.

Chapter 4 described the characterization and testing of the real time PCR module. The original design of the optical detection hardware for real time PCR was laid out by Dr. Behnam & Dr .Kaigala. I characterized the system by measuring its optical power output at each stage of its detection system. Then I performed serial dilutions with fluorescein dye to estimate the limit of detection of the system. I found that there was a non-linear relationship between fluorophore concentration and the fluorescence intensity captured by the CCD camera. This non-linearity was traced to gamma encoding of JPEG images stored by the CCD camera which introduces an exponent when saving raw fluorescence images into a compressed 8-bit format (Poynton, 1996). After reversing the effect of gamma correction as described by Medberry *et al.* (2004), I estimated the limit of detection of the system to be 7.34 nM of fluorescein which corresponded to ~1.77 ng/μL of ß2m PCR product. This suggested that the TTK was capable of detecting medium and strong PCR products.

In addition, I developed a data analysis algorithm in Python to sort, smooth, subtract baselines, and calculate Ct values from raw real time PCR data. On-chip real time PCR with ß2m genomic DNA showed clear amplification with a Ct value of 24.3 ± 0.9 cycles. As a follow-up test, I performed on-chip real time PCR with *P.malariae* on the TTK. This was a more clinically-relevant test since *P.malariae* is one of the 4 main strains of malaria. I obtained strong amplification here as well with a Ct value of 18.9 ± 0.6 cycles.

After real time PCR, MCA was performed to determine the melting temperature of PCR products as an indirect assay to identify them since intercalating dyes like LCgreen plus measure the fluorescence from double-stranded DNA but do not provide information about the identity of the PCR product. On-chip MCA measures the melting temperature of PCR products and provides a way to distinguish samples based on their physical and chemical properties (such as length and base sequence).

Chapter 5 described my contributions to on-chip MCA. I helped to test the temperature control algorithm for MCA. In addition, I developed a data analysis script in Python to sort and smooth raw MCA data. I was also involved with testing of the MCA subsystem with on-chip and off-chip ß2m genomic DNA and *P.malariae* PCR products. At first, I performed on-chip MCA with an on-chip ß2m genomic DNA PCR product. There was a clear fluorescence dip corresponding to the melting of the double stranded PCR product.

However, noise spikes in the signal was amplified when the negative first derivative of fluorescence was taken to construct a melt curve. I identified the source of noise as inherent variations in the CCD readout – a problem that the manufacturer of the camera has addressed in newer models of the Meade® deep sky imager camera series by including a temperature sensor in the CCD camera to allow acquisition and correction of noise with dark images at higher temperatures. I smoothed the MCA data with a median filter to eliminate outliers and a moving average filter to provide a curved look. After filtering, I obtained a clear and reproducible melting peak for ß2m genomic DNA.

Next, I tested the MCA module with *P.malariae* PCR products from the Lightcycler and the TTK. I obtained strong melting peaks at for both on-chip and off-chip PCR products. However, I observed a 6˚C offset between Tm values on the TTK and Lightcycler. The reason for this temperature offset was investigated thoroughly – I examined the hardware, software, and firmware in the TTK that affect Tm calculations. The offset between TTK and Lightcycler Tm values was likely due to a firmware artifact. I demonstrated this by re-programming the TTK (with exactly the same firmware) and with all other variables (hardware, software, protocols) held constant. I found that after re-programming the TTK, the 6˚C offset was no longer observed, suggesting that it arose from an error or corruption in the firmware.

After testing each of the SP, PCR, and MCA modules individually, they were integrated to purify, amplify, and analyze ß2m DNA from human buccal cells. The first SP-PCR-MCA reaction showed strong amplification that was similar in strength to what was obtained with ß2m genomic DNA. However, the next two SP-PCR-MCA reactions showed much weaker peaks that were barley distinguishable from the negative control. MCA analysis on all 3 samples showed PCR product peaks with an average Tm of 77.3 ± 1.6˚C. As expected from the amplification curves, SP-PCR run 1 had a stronger PCR product peak than runs 2 and 3. To verify the results of on-chip SP-PCR-MCA, the PCR products were analyzed by CE in the μTK. CE results also showed a strong (~100ng/μL) PCR product peak for experiment 1, and weak (~6 ng/μL) PCR products for experiments 2 and 3. The difference in PCR product strengths between the on-chip SP-PCR-MCA experiments may be attributed to differences in the starting amount of buccal cells extracted during on-chip SP. During runs 2 and 3, a smaller amount of magnetic beads (and DNA) was added to the on-chip reaction because of beads clumping to cotton fibres from the swabs used for buccal cell collection.

The on-chip SP-PCR-MCA results presented in this thesis provide a proof of principle demonstration of the purification, amplification, and analysis of genetic material from raw clinical samples using a portable and inexpensive lab on a chip instrument. Future work in the AML will expand on this work to improve system sensitivity, reduce cost and complexity, and facilitate clinical testing for applications such as the detection of malaria parasites in whole blood.

7.2 Future work

7.2.1 Optical illumination

As described in chapter 4, a 340 mW LED light source was used for optical illumination. However, much of this power was lost when the LED was connected to a fiber optic cable. This was because light from the LED is not collimated and has a 140° viewing angle. To reduce simplicity and cost, the current design of the optical subsystem in the TTK does not make use of any collimation optics. The current approach described in chapter 4.2.2 involves using a custom-built plastic fitting to hold the LED and optical fiber together. This results in significant optical power loss after attaching the LED to a 1mm optical fiber since only a small portion of the light from the LED is captured. In fact, the optical power dropped to only 3 mW (~1% of the source) after attaching the fiber optic cable to the LED.

Light coupling from an LED to an optical fiber is a difficult task. There are commercial LED assemblies that transfer light from LEDs directly into optical fibers. However, these assemblies face the same limitations are as our in-house solution. For example, fiber-fitted LEDs such as the IF-E92B (Industrial fiber optics Inc., AZ, USA) has a "connector less" design so that a standard 1 mm optical fiber is screwed directly into the LED light source – but the company only provides a model with a maximum power output of 75 μW. In fact, the D168-588 fiber-pigtailed LED (Doric Lenses, QC, Canada) makes use of the same Luxeon® LED light source as in the TTK but its optical assembly provides an output power ranging from 0.023 mW to 28.4 mW as cost and complexity increase[1]. This suggests that while commercial LED-fiber assemblies might provide some improvement in the power output of the system, the improvements might not be very significant since the power loss appears to be a problem associated with choosing to link LEDs to optical fibers – which is by design an inefficient approach.

Another method for improving the optical sensitivity of the system would be to move to a different illumination scheme. For example, the lab on a chip system presented by Novak *et al.* (2007) makes use of an illumination system designed after a DVD-head. This permits collimated light output in a portable, manufacturable, and inexpensive housing. The design of the illumination optics contributed significantly to a limit of detection of 5 nM of fluorescein obtained by Novak *et al.* (2007) – roughly 2 orders of magnitude more sensitive than the TTK.

7.2.2 Reducing noise

In addition, the sensitivity of real time PCR and MCA can be improved by reducing noise in the optics subsystem. As described in chapter 5, the primary source of noise encountered was readout noise inherent in the CCD camera at high temperatures. CCD noise can be reduced by implementing noise reduction schemes such as the use of an active cooling

---

[1] Information about their product specifications were obtained from http://www.doriclenses.com/produits/168.html on May 26, 2011.

system (Karellas *et al.*, 1992) to keep the CCD close to its optimal operating conditions even when the system temperature rises as on-chip real time PCR and MCA are performed at high temperatures.

While a heat sink is included on the Meade® DSI camera used in this thesis, to reduce cost and complexity no additional active cooling components were included. The camera relies on user capture of dark images to reduce noise. However, the camera's noise correction capability is temperature-dependent and the user manual recommends repeating dark image measurements if the temperature changes significantly. The manufacturer addressed this limitation of the DSI camera by including an embedded temperature sensor in newer versions of the deep sky imager camera series. The DSII and DSIII cameras have a built-in temperature sensor so that dark images can be automatically captured and mapped to the temperature at which the image was acquired[2]. This temperature-dependent noise measurement permits more robust elimination of noise. As such, another approach to reduce noise in real time PCR and MCA data sets would be to use a newer model of the Meade deep sky imager camera (such as the DSIII) which includes a built in temperature sensor that allows temperature-dependent noise correction, be used to perform robust noise removal from CCD images.

7.2.3 Quantification of starting DNA concentration

Initial on-chip real time PCR with ß2m genomic DNA shows clear amplification above background levels. However, duplicate experiments are required to prove that changes in DNA concentration correspond to variations in Ct values detected by the TTK. The rationale behind performing real time PCR on the microchip was to permit quantification of the starting copy number of DNA in a sample.

As described in chapter 1, there are 2 main approaches to quantifying real time PCR data – absolute and relative quantification. Both methods require the synthesis of standard samples with known DNA concentrations. Absolute quantification involves generating a calibration curve with Ct vs concentration for several standard samples with known concentration. Meanwhile, the relative quantification method relies on assumptions of ideal efficiency to simplify the quantification process and compares 1 standard sample with 1 test sample. The TTK could employ relative quantification of PCR products by comparing test samples with a ß2m standard that is quantified on a Nanodrop spectrophotometer. Ct values of the test samples can be derived using the $2^{\Delta\Delta C_T}$ method as described in Kubista *et al.* (2006).

7.2.4 Reducing variation in SP protocol

One of the major sources of variation in the strength of on-chip SP-PCR-MCA amplicons was the variation in the amount of cells added to the SP reaction. Bead clumps formed be-

---

[2] Specifications for the newer models of the Meade deep sky imager camera series are available at: http://www.meade.com/dsi3/index.html, accessed March 19 2011.

cause of loose cotton fibres from the buccal cell extraction swabs reduced the size of the bead pellet extracted during on-chip PCR (visibly by ~50%). Bead-clumping can be reduced by changing the buccal cell applicator from a cotton-based swab to a hard-brush with plastic bristles. This way there is less likelihood of free-floating strands that will clump to magnetic beads and reduce the amount of DNA collected. In addition, it might be desirable to prepare 1 large lysate mix for each set of duplicate or triplicate on-chip SP-PCR experiments to reduce the uncertainty associated with collecting fresh buccal cells for each experiment. This way, all the on-chip SP-PCR experiments performed at the same time would have roughly the same starting DNA concentration, allowing direct comparison of amplification and melt curves. This would be compatible with the current protocol since each SP lysate mix has a total volume of ~650 μL, of which only 5 μL is used during an on-chip SP experiment.

Also, as discussed in chapter 6, we carried out cell lysis and mixing with a micropipetter in a tube prior to on-chip SP. In addition, during on-chip separation, we removed STW buffer with a handheld micropipetter. These manual handling steps were necessary while we optimized the protocol for on-chip nucleic acid purification. However, these manual steps contributed to the variabilities in SP-PCR-MCA results. In addition, human intervention increases the risk of sample contamination. For fully automated and integrated SP, these handling steps should be ported onto the microfluidic chip. To accomplish this, a chip re-design might be required. We would need extra wells and channels to store cell lysis and purification reagents and microvalves to mix SP reagents. However, since the XY stage already permits complex choreography in 2 dimensions, such a solution would not necessarily require extra electronic instrumentation.

In addition, expanding the sample preparation section of the microchip would allow us to take advantage of the pre-concentration capability of bead-based purification methods (Price *et al.*, 2009). Precise volume control would allow extraction of DNA in a large volume sample well, and elution with PCR mix in a smaller volume well. This would boost the sensitivity of downstream amplification and detection steps. A simple first pass at this on-chip pre-concentration would involve varying the sizes/volumes of sample preparation wells (e.g. large sample input wells feeding to smaller, valved output wells for concentrating analytes of interest). The re-design of the SP module for improved automation is currently in development at the AML.

7.2.5 Miniaturize SP subsystem

As a follow-up to the 2 dimensional X-Y stage sample preparation module, a simpler 1-dimensional system was developed to control magnet motion using a single servomotor (HS-55, Hitec, Poway, USA). This work was completed by & M.Nielsen at the AML with guidance on scripting magnet and motor motion from A.Olanrewaju and assistance with electronics development provided by Dr. Behnam.

The 2-D SP module was advantageous during the initial testing of the TTK as it allowed complex choreography that was helpful in determining the optimal protocol for on-chip SP as described in chapter 3. However, once a suitable magnet control scheme was chosen, the SP module could be simplified to reduce cost and complexity. The 1-D SP module was operated using pulse width modulated (PWM) control signals transferred directly from the central PIC microcontroller unit in the TTK to a single servomotor. With this simple setup, magnet motion could be controlled directly by the LOC toolkit microcontroller unit without the need for an additional microcontroller and supporting electronics as required for the 2-D SP module. This reduces the cost of the SP infrastructure from $500 ($200 in components) to ~$50. The differences between the 2-D and 1-D SP motion paradigms are illustrated in figure 7.1

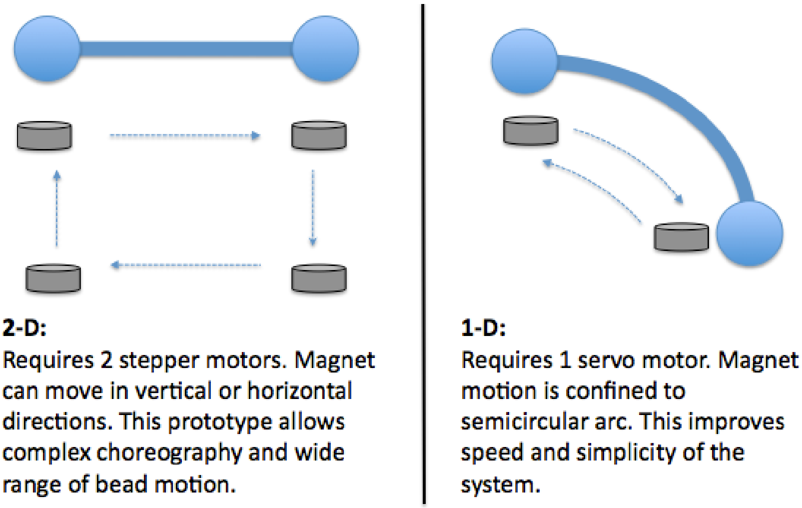

2-D:
Requires 2 stepper motors. Magnet can move in vertical or horizontal directions. This prototype allows complex choreography and wide range of bead motion.

1-D:
Requires 1 servo motor. Magnet motion is confined to semicircular arc. This improves speed and simplicity of the system.

Figure 7.1: Comparison of 2-D and 1-D SP modules. The 2-D approach focuses on a wide range of X-Y motion, while the 1-D implementation restricts motion to a single axis for reduced complexity and cost.

7.2.6 Clinical testing of the TTK with malaria samples from whole blood

The main aim for implementing SP, PCR, and MCA on the TTK is to apply to the system for point of care clinical analysis. Initial demonstrations of SP-PCR-MCA analysis of ß2m DNA from buccal cells (see chapter 6) and PCR-MCA analysis of *P.malariae* (see chapter 5) have been completed. However, the main goal is to perform SP-PCR-MCA to detect malarial DNA in whole blood. The experiments and results in this thesis allow the drafting of a proposed plan of action to implement SP-PCR-MCA with multiple malarial strains on the TTK. This plan was drafted in collaboration with Dr. Taylor and Dr. Yanow, our collaborators from the Provincial Laboratory for Public Health (Edmonton, AB).

First, off-chip SP-PCR-MCA controls would be performed with each of the *P.falciparum*, *P.malariae*, *P.ovale* and *P.vivax* assays as described in Shokoples *et al.* (2009). In addition, a multiplexed reaction with all the malaria strains would be performed to demonstrate malaria speciation. The first set of controls would make use of *Plasmodium* samples from purified genomic DNA, then the experiments would be repeated with frozen culture samples of each malaria strain. If these control experiments on conventional instruments proved successful, on-chip experiments would follow. Each on-chip experiment would be performed on a separate chip to minimize the risk of contamination. Sample preparation would be conducted according to the protocol described in chapter 3 but using the Invitrogen Chargeswitch gDNA Blood kit (Invitrogen, Carlsbad, CA, USA) instead since whole blood is the target instead of buccal cells.

The proposed on-chip experiments for clinical testing of SP-PCR-MCA with malaria samples are as follows:

1. On-chip SP-PCR MCA with serial dilution of *P.falciparum* parasites spiked into uninfected whole blood from a starting parasitemia of 10% to 0.01%. Four on-chip real time PCR experiments would be required for the serial dilutions and one no-template control would be included as well for a total of five on-chip experiments. This would allow the generation of a standard curve to allow quantitation of PCR efficiency and starting DNA concentrations in subsequent experiments.

2. Repeat serial dilutions for *P.malariae*, *P.ovale*, and *P.vivax* strains to generate standard curves and allow quantitation. However, if time or chips are in short supply, the experiments can focus on the *P.falciparum* strain since it is the most deadly malaria species in humans (Shokoples *et al.*, 2009).

3. Test a blinded panel of 20 clinical samples. For example: 4 negatives, and 4 four sets of each of the malaria species. Compare with off-chip results from the lightcycler, as well as gold standard methods of malaria detection such as microscopy and Taqman assays as described in past work by the Yanow group in Shokoples *et al.* (2009).

4. Test 1 sample with a mixed infection to see if both peaks can be detected during on-chip MCA.

If successful, these experiments would provide sufficient data for the preparation of a manuscript that could be submitted to a high impact journal. Furthermore, this demonstration could lead to collaborations with researchers and medical practitioners in the life sciences that would help to achieve the goal of a portable and inexpensive lab on a chip instrument for point of care analysis.

Bibliography

Abramoff, MD, Magelhaes, PJ, Ram, and SJ. Image processing with imagej. *Biophotonics International*, 11(7):36–42, 2004.

A. Atrazhev, D. P. Manage, A. J. Stickel, H. J. Crabtree, L. M. Pilarski, and J. P. Acker. In-gel technology for PCR genotyping and pathogen detection. *Anal Chem*, 82(19):8079–87, Oct 2010.

P.-A. Auroux, Y. Koc, A. deMello, A. Manz, and P. J. R. Day. Miniaturised nucleic acid analysis. *Lab Chip*, 4(6):534–46, Dec 2004.

S. M. Azimi, G. Nixon, J. Ahern, and W. Balachandran. A magnetic bead-based dna extraction and purification microfluidic device. *Microfluidics and Nanofluidics*, pages 1–9, Mar 2011.

M. M. Bahi, M.-N. Tsaloglou, M. Mowlem, and H. Morgan. Electroporation and lysis of marine microalga karenia brevis for rna extraction and amplification. *J R Soc Interface*, 8 (57):601–8, Apr 2011.

T. Baier, T. E. Hansen-Hagge, R. Gransee, A. Crombe, S. Schmahl, C. Paulus, K. S. Drese, H. Keegan, C. Martin, J. J. O'Leary, L. Furuberg, L. Solli, P. Gronn, I. M. Falang, A. Karlgard, A. Gulliksen, and F. Karlsen. Hands-free sample preparation platform for nucleic acid analysis. *Lab Chip*, 9(23):3399–3405, Jan 2009.

N. Bao and C. Lu. Microfluidics-based lysis of bacteria and spores for detection and analysis. In *Principles of bacterial detection: biosensors, recognition receptors, and microsystems*, chapter 30, pages 817–831. Springer Science + Business Media, LLC., New York, 2008.

L. Benesova-Minarikova, L. Fantova, and M. Minarik. Multicapillary electrophoresis of unlabeled dna fragments with high-sensitive laser-induced fluorescence detection by counter-current migration of intercalation dye. *Electrophoresis*, 26:4064–4069, Jan 2005.

R. Boom, C. Sol, M. Beld, J. Weel, J. Goudsmit, and P. W. van Dillen. Improved silica-guanidiniumthiocyanate dna isolation procedure based on selective binding of bovine alpha-casein to silica particles. *Journal of clinical microbiology*, 37(3):615–619, Jan 1999.

D. Brennan, J. Justice, B. Corbett, T. McCarthy, and P. Galvin. Emerging optofluidic technologies for point-of-care genetic analysis systems: a review. *Anal Bioanal Chem*, 395(3): 621–36, Oct 2009.

N. Cady, S. Stelick, M. Kunnavakkam, and C. Batt. Real-time PCR detection of listeria monocytogenes using an integrated microfluidics platform. *Sensors & Actuators: B*, 107: 332–341, Jan 2005.

W. Cao, C. Easley, J. Ferrance, and J. Landers. Chitosan as a polymer for pH-induced DNA capture in a totally aqueous system. *Anal. Chem*, 78:7222–7228, Jan 2006.

A. Chaudhari, T. Woudenberg, M. Albin, and K. Goodson. Transient liquid crystal thermometry of microfabricated PCR vessel arrays. *J Microelectromech S*, 7(4):345–355, Jan 1998.

D. Chen, M. Mauk, X. Qiu, C. Liu, J. Kim, S. Ramprasad, S. Ongagna, W. R. Abrams, D. Malamud, P. L. A. M. Corstjens, and H. H. Bau. An integrated, self-contained microfluidic cassette for isolation, amplification, and detection of nucleic acids. *Biomed Microdevices*, 12(4):705–719, Jan 2010.

L. Chen, A. Manz, and P. J. R. Day. Total nucleic acid analysis integrated on microfluidic devices. *Lab on a Chip*, 7(11):1413–1423, 2007a.

X.-W. Chen, Z.-R. Xu, B.-Y. Qu, Y.-F. Wu, J. Zhou, H.-D. Zhang, J. Fang, and J.-H. Wang. Dna purification on a lab-on-valve system incorporating a renewable microcolumn with in situ monitoring by laser-induced fluorescence. *Anal Bioanal Chem*, 388(1):157–63, May 2007b.

Y. Cho, J. Kim, Y. Lee, Y. Kim, K. Namkoong, H. Lim, K. Oh, S. Kim, J. Han, C. Park, Y. Pak, C. Ki, J. Choi, H. Myeong, and C. Ko. Clinical evaluation of micro-scale chip-based PCR system for rapid detection of hepatitis b virus. *Biosens Bioelectron*, 21(11):2161–2169, Jan 2006.

P. Chomczynski and N. Sacchi. The single-step method of RNA isolation by acid guanidinium thiocyanate–phenol–chloroform extraction: twenty-something years on. *Nature Protocols*, 1(2):581–585, June 2006.

L. Christel, K. Petersen, and W. McMillan. Rapid, automated nucleic acid probe assays using silicon microstructures for nucleic acid concentration. *Journal of biomechanical engineering*, 121(1):22–27, Jan 1999.

T. A. Crowley and V. Pizziconi. Isolation of plasma from whole blood using planar microfilters for lab-on-a-chip applications. *Lab Chip*, 5(9):922–9, Sep 2005.

A. B. Cubitt, R. Heim, S. R. Adams, A. E. Boyd, L. A. Gross, and R. Y. Tsien. Understanding, improving and using green fluorescent proteins. *Trends in Biochemical Sciences*, 20(11): 448–55, Nov 1995.

F. de Monbrison, C. Angei, A. Staal, K. Kaiser, and S. Picot. Simultaneous identification of the four human plasmodium species and quantification of plasmodium DNA load in human blood by real-time polymerase chain reaction. *T Roy Soc Trop Med H*, 97(4): 387–390, Jan 2003.

A. deMello and N. Beard. Focus. dealing with 'real'samples: sample pre-treatment in microfluidic systems. *Lab on a Chip*, 3:11N–19N, Jan 2003.

M. Dineva, L. Mahilum-Tapay, and H. Lee. Sample preparation: a challenge in the development of point-of-care nucleic acid-based assays for resource-limited settings. *The Analyst*, 132(12):1193–1199, 2007.

G. R. M. Duarte, C. W. Price, J. L. Littlewood, D. M. Haverstick, J. P. Ferrance, E. Carrilho, and J. P. Landers. Characterization of dynamic solid phase DNA extraction from blood with magnetically controlled silica beads. *The Analyst*, 135(3):531–7, Mar 2010.

C. J. Easley, J. M. Karlinsey, J. M. Bienvenue, L. A. Legendre, M. G. Roper, S. H. Feldman, M. A. Hughes, E. L. Hewlett, T. J. Merkel, J. P. Ferrance, and J. P. Landers. A fully integrated microfluidic genetic analysis system with sample-in–answer-out capability. *Proceedings of the National Academy of Sciences*, 103(51):19272–19277, 2006.

M. J. Espy, J. R. Uhl, L. M. Sloan, S. P. Buckwalter, M. F. Jones, E. A. Vetter, J. D. C. Yao, N. L. Wengenack, J. E. Rosenblatt, F. R. C. III, and T. F. Smith. Real-time PCR in clinical microbiology: applications for routine laboratory testing. *Clin Microbiol Rev*, Jan 2006.

R. Ganguly, T. Hahn, and S. Hardt. Magnetophoretic mixing for in situ immunochemical binding on magnetic beads in a microfluidic channel. *Microfluidics and Nanofluidics*, 8(6): 739–753, Jun 2010.

M. A. M. Gijs, F. Lacharme, and U. Lehmann. Microfluidic applications of magnetic particles for biological analysis and catalysis. *Chem Rev*, 110(3):1518–63, Mar 2010.

H. Gudnason, M. Dufva, D. D. Bang, and A. Wolff. Comparison of multiple DNA dyes for real-time PCR: effects of dye concentration and sequence composition on DNA amplification and melting temperature. *Nucleic Acids Research*, 35(19):e127, Jan 2007.

A. Gulliksen, L. Solli, F. Karlsen, H. Rogne, E. Hovig, T. Nordstrom, and R. Sirevag. Real-time nucleic acid sequence-based amplification in nanoliter volumes. *Analytical Chemistry*, 76(1):9–14, Jan 2004.

T. Hänscheid and M. Grobusch. How useful is PCR in the diagnosis of malaria? *Trends in Parasitology*, 18(9):395–398, Sep. 2002.

G. P. Hatch and R. E. Stelter. Magnetic design considerations for devices and particles used for biological high-gradient magnetic separation (HGMS) systems. *J Magn Magn Mater*, 225(1-2):262–276, Jan 2001.

S. I. Hay, C. A. Guerra, P. W. Gething, A. P. Patil, A. J. Tatem, A. M. Noor, C. W. Kabaria, B. H. Manh, I. R. F. Elyazar, S. Brooker, D. L. Smith, R. A. Moyeed, and R. W. Snow. A world malaria map: Plasmodium falciparum endemicity in 2007. *Plos Med*, 6(3):e1000048, Jan 2009.

M. Herrmann, J. Durtschi, L. Bromley, C. Wittwer, and K. Voelkerding. Amplicon DNA melting analysis for mutation scanning and genotyping: Cross-platform comparison of instruments and dyes. *Clinical Chemistry*, 52(3):494–503, Jan 2006.

V. N. Hoang. Thermal management strategies for microfluidic devices. Master's thesis, University of Alberta, Jan 2008.

V. N. Hoang, G. V. Kaigala, and C. J. Backhouse. Dynamic temperature measurement in microfluidic devices using thermochromic liquid crystals. *Lab on a Chip*, 8:484–487, Feb 2008.

A. J. Hopwood, C. Hurth, J. Yang, Z. Cai, N. Moran, J. G. Lee-Edghill, A. Nordquist, R. Lenigk, M. D. Estes, J. P. Haley, C. R. Mcalister, X. Chen, C. Brooks, S. Smith, K. Elliott, P. Koumi, F. Zenhausern, and G. Tully. Integrated microfluidic system for rapid forensic DNA analysis: sample collection to DNA profile. *Analytical Chemistry*, 82(16):6991–9, Aug 2010.

Y. Hu, Y. Li, Y. Zhang, G. Li, and Y. Chen. Development of sample preparation method for auxin analysis in plants by vacuum microwave-assisted extraction combined with molecularly imprinted clean-up procedure. *Anal Bioanal Chem*, 399(10):3367–74, Apr 2011.

C. Hurth, S. D. Smith, A. R. Nordquist, R. Lenigk, B. Duane, D. Nguyen, A. Surve, A. J. Hopwood, M. D. Estes, J. Yang, Z. Cai, X. Chen, J. G. Lee-Edghill, N. Moran, K. Elliott, G. Tully, and F. Zenhausern. An automated instrument for human STR identification: Design, characterization, and experimental validation. *Electrophoresis*, 31(21):3510–3517, Oct 2010.

K.-Y. Hwang, H.-K. Lim, S.-Y. Jung, K. Namkoong, J.-H. Kim, N. Huh, C. Ko, and J.-C. Park. Bacterial DNA sample preparation from whole blood using surface-modified si pillar arrays. *Analytical Chemistry*, 80(20):7786–91, Oct 2008. Bacterial SP with silica pillar array.

D. Irimia and M. Toner. Cell handling using microstructured membranes. *Lab Chip*, 6(3): 345–52, Mar 2006.

D. Issadore, H. Shao, J. Chung, A. Newton, M. Pittet, R. Weissleder, and H. Lee. Self-assembled magnetic filter for highly efficient immunomagnetic separation. *Lab Chip*, 11 (1):147–51, Jan 2011.

N. Ivanova, J. Dewaard, and P. Hebert. An inexpensive, automation-friendly protocol for recovering high-quality DNA. *Molecular Ecology Notes*, 6(4):998–1002, Mar. 2006.

C. Jegat, A. Bois, and M. Camps. Continuous phase viscosity influence on maximum diameters of poly(styrene-divinylbenzene) beads prepared by suspension polymerization. *J Polym Sci Pol Phys*, 39(3):201–210, Jan 2001.

D. Joseph. *Modelling and calibration of logarithmic* CMOS *image sensors*. PhD thesis, University of Oxford, Sep 2002.

G. Kaigala, M. Behnam, A. Bidulock, C. Bargen, R. Johnstone, D. Elliott, and C. Backhouse. A scalable and modular lab-on-a-chip genetic analysis instrument. *Analyst*, 135: 1606–1617, Mar 2010.

G. V. Kaigala. *Genetic Analysis Using Lab-on-a-Chip Technologies*. PhD thesis, University of Alberta, Feb 2009.

G. V. Kaigala, V. N. Hoang, A. Stickel, J. Lauzon, D. Manage, L. M. Pilarski, and C. J. Backhouse. An inexpensive and portable microchip-based platform for integrated RT-PCR and capillary electrophoresis. *The Analyst*, 133(3):331–338, March 2008.

A. Karellas, L. J. Harris, H. Liu, M. A. Davis, and C. J. D'Orsi. Charge-coupled device detector: performance considerations and potential for small-field mammographic imaging applications. *Med Phys*, 19(4):1015–23, Jan 1992.

M. Karle, J. Miwa, G. Czilwik, V. Auwärter, G. Roth, R. Zengerle, and F. von Stetten. Continuous microfluidic DNA extraction using phase-transfer magnetophoresis. *Lab Chip*, 10(23):3284–90, Dec 2010.

S. Karlin and S. F. Altschul. Applications and statistics for multiple high-scoring segments in molecular sequences. *Proc Natl Acad Sci USA*, 90(12):5873–7, Jun 1993.

J. Kim and B. K. Gale. Quantitative and qualitative analysis of a microfluidic DNA extraction system using a nanoporous AlO(x) membrane. *Lab on a Chip*, 8(9):1516–23, Sep 2008.

J. Kim, M. Johnson, P. Hill, and B. K. Gale. Microfluidic sample preparation: cell lysis and nucleic acid purification. *Integr Biol (Camb)*, 1(10):574–86, Oct 2009.

J. Kim, M. Mauk, D. Chen, X. Qiu, J. Kim, B. Gale, and H. H. Bau. A PCR reactor with an integrated alumina membrane for nucleic acid isolation. *The Analyst*, 135(9):2408–14, Sep 2010.

L. Kricka and P. Wilding. Microchip PCR. *Analytical and Bioanalytical Chemistry*, 377(5): 820–825, 2003.

M. Kubista, J. M. Andrade, M. Bengtsson, A. Forootan, J. Jonak, K. Lind, R. Sindelka, R. Sjoback, B. Sjogreen, L. Strombom, A. Stahlberg, and N. Zoric. The real-time polymerase chain reaction. *Molecular aspects of Medicine*, 27:95–125, Jan 2006.

D. Lee, P. Chen, and G. Lee. The evolution of real-time PCR machines to real-time PCR chips. *Biosensors and Bioelectronics*, 25:1820–1824, Jan 2010.

H.-J. Lee, B. C. Kim, K.-W. Kim, Y. K. Kim, J. Kim, and M.-K. Oh. A sensitive method to detect Escherichia coli based on immunomagnetic separation and real-time PCR amplification of aptamers. *Biosens Bioelectron*, 24(12):3550–5, Aug 2009.

U. Lehmann, C. Vandevyver, V. K. Parashar, and M. A. M. Gijs. Droplet-based DNA purification in a magnetic lab-on-a-chip. *Angew Chem Int Ed Engl*, 45(19):3062–7, May 2006.

J. Lichtenberg, N. F. de Rooij, and E. Verpoorte. Sample pretreatment on microfabricated devices. *Talanta*, 56(2):233–266, 2002.

K.-Y. Lien, C.-J. Liu, P.-L. Kuo, and G.-B. Lee. Microfluidic system for detection of alpha-thalassemia-1 deletion using saliva samples. *Analytical Chemistry*, 81(11):4502–9, Jun 2009.

C.-C. Lin, J.-L. Hsu, and G.-B. Lee. Sample preconcentration in microfluidic devices. *Microfluid Nanofluid*, 10(3):481–511, Mar 2011.

J. Liu, M. Enzelberger, and S. Quake. A nanoliter rotary device for polymerase chain reaction. *Electrophoresis*, 23(10):1531–1536, Jan 2002.

P. Liu, X. Li, S. A. Greenspoon, J. R. Scherer, and R. A. Mathies. Integrated DNA purification, PCR, sample cleanup, and capillary electrophoresis microchip for forensic human identification. *Lab Chip*, Feb 2011.

I. Mackay. Real-time PCR in the microbiology laboratory. *Clinical Microbiology and Infection*, 10:190–212, Jan 2004.

M. Mahalanabis, H. Al-Muayad, M. D. Kulinski, D. Altman, and C. M. Klapperich. Cell lysis and DNA extraction of gram-positive and gram-negative bacteria from whole blood in a disposable microfluidic chip. *Lab on a Chip*, 9(19):2811–7, Oct 2009.

M. Mahalanabis, J. Do, H. ALMuayad, J. Y. Zhang, and C. M. Klapperich. An integrated disposable device for DNA extraction and helicase dependent amplification. *Biomed Microdevices*, 12(2):353–9, Apr 2010.

K. Mangold, R. Manson, E. Koay, L. Stephens, M. Regner, R. Thomson, L. Peterson, and K. Kaul. Real-time PCR for detection and identification of plasmodium spp. *Journal of clinical microbiology*, 43(5):2435–2440, Jan 2005.

F. Mao, W.-Y. Leung, and X. Xin. Characterization of evagreen and the implication of its physicochemical properties for qpcr applications. *BMC Biotechnology*, 7(1):76, Nov 2007.

N. Markham and M. Zuker. DINAMelt web server for nucleic acid melting prediction. *Nucleic Acids Research*, 33:W577–W581, Jan 2005.

N. A. Martínez, R. J. Schneider, G. A. Messina, and J. Raba. Modified paramagnetic beads in a microfluidic system for the determination of ethinylestradiol (EE2) in river water samples. *Biosens Bioelectron*, 25(6):1376–81, Feb 2010.

S. Medberry, S. Gallagher, and B. Moomaw. Overview of digital electrophoresis analysis. In *Current Protocols in Molecular Biology*, chapter 10.5, pages 1–25. John Wiley & Sons, Inc., New York, Sep 2004. doi: 10.1002/0471140864.ps1012s41.

D. Misir, H. Malki, and G. Chen. Design and analysis of a fuzzy proportional-integral-derivative controller. *Fuzzy Set Syst*, 79(3):297–314, Jan 1996.

M. R. Mohamadi, Z. Svobodova, R. Verpillot, H. Esselmann, J. Wiltfang, M. Otto, M. Taverna, Z. Bilkova, and J.-L. Viovy. Microchip electrophoresis profiling of Aβ peptides in the cerebrospinal fluid of patients with Alzheimer's disease. *Analytical Chemistry*, 82(18): 7611–7, Sep 2010.

T. Nakagawa, T. Tanaka, D. Niwa, T. Osaka, H. Takeyama, and T. Matsunaga. Fabrication of amino silane-coated microchip for DNA extraction from whole blood. *J Biotechnol*, 116 (2):105–11, Mar 2005.

S. Nakano, M. Fujimoto, H. Hara, and N. Sugimoto. Nucleic acid duplex stability: influence of base composition on cation effects. *Nucleic Acids Research*, 27(14):2957–65, Jul 1999.

P. Neuzil, L. Novak, J. Pipper, S. Lee, L. F. P. Ng, and C. Zhang. Rapid detection of viral RNA by a pocket-size real-time PCR system. *Lab Chip*, 10(19):2632–4, Oct 2010.

B. T. T. Nguyen, G. Koh, H. S. Lim, A. J. S. Chua, M. M. L. Ng, and C.-S. Toh. Membrane-based electrochemical nanobiosensor for the detection of virus. *Analytical Chemistry*, 81 (17):7226–34, Sep 2009.

M. A. Northrup, B. Benett, D. Hadley, P. Landre, S. Lehew, J. Richards, and P. Stratton. A miniature analytical instrument for nucleic acids based on micromachined silicon reaction chambers. *Analytical Chemistry*, 70(5):918–922, 1998.

L. Novak, P. Neuzil, J. Pipper, Y. Zhang, and S. Lee. An integrated fluorescence detection system for lab-on-a-chip applications. *Lab on a Chip*, 7(1):27–29, Jan 2007.

S. Peeters, T. Stakenborg, F. Colle, C. Liu, L. Lagae, and M. V. Ranst. Real-time PCR to study the sequence specific magnetic purification of DNA. *Biotechnol Progress*, 26(6):1678–1684, Sep 2010.

J. Pipper, M. Inoue, L. F.-P. Ng, P. Neuzil, Y. Zhang, and L. Novak. Catching bird flu in a droplet. *Nature medicine*, 13(10):1259–1263, Jan 2007.

J. Pipper, Y. Zhang, P. Neuzil, and T.-M. Hsieh. Clockwork PCR including sample preparation. *Angew Chem Int Edit*, 47(21):3900–3904, Jan 2008.

C. Poynton. Gamma. In *A technical introduction to digital video*, chapter 6, pages 91–114. John Wiley & Sons Ltd., New York, 1996.

C. Price, D. Leslie, and J. Landers. Nucleic acid extraction techniques and application to the microchip. *Lab on a Chip*, 9:2484–2494, Jan 2009.

Q. Ramadan and M. A. M. Gijs. Simultaneous sample washing and concentration using a ”trapping-and-releasing” mechanism of magnetic beads on a microfluidic chip. *The Analyst*, 136(6):1157–66, Mar 2011.

C. R. Reedy, C. W. Price, J. Sniegowski, J. P. Ferrance, M. Begley, and J. P. Landers. Solid phase extraction of DNA from biological samples in a post-based, high surface area poly(methyl methacrylate) (PMMA) microdevice. *Lab on a Chip*, 11:1603–1611, Jan 2011.

K. Ririe, R. Rasmussen, and C. Wittwer. Product differentiation by analysis of DNA melting curves during the polymerase chain reaction. *Anal Biochem*, 245(2):154–160, Jan 1997.

R. Rutledge. Sigmoidal curve-fitting redefines quantitative real-time PCR with the prospective of developing automated high-throughput applications. *Nucleic Acids Research*, 32 (22):e178, Jan 2004.

A.-E. Saliba, L. Saias, E. Psychari, N. Minc, D. Simon, F.-C. Bidard, C. Mathiot, J.-Y. Pierga, V. Fraisier, J. Salamero, V. Saada, F. Farace, P. Vielh, L. Malaquin, and J.-L. Viovy. Microfluidic sorting and multimodal typing of cancer cells in self-assembled magnetic arrays. *Proc Natl Acad Sci USA*, 107(33):14524–9, Aug 2010.

R. Samy, T. Glawdel, and C. L. Ren. Method for microfluidic whole-chip temperature measurement using thin-film poly(dimethylsiloxane)/rhodamine b. *Analytical Chemistry*, 80 (2):369–375, Jan 2008.

M. Sandberg, L. Lundberg, M. Ferm, and I. Yman. Real time PCR for the detection and discrimination of cereal contamination in gluten free foods. *Eur Food Res Technol*, 217(4): 344–349, Jan 2003.

J. Schefe, K. Lehmann, and I. Buschmann. Quantitative real-time RT-PCR data analysis: current concepts and the novel "gene expresion's ct difference" formula. *Journal of Molecular Medicine*, 84:901–910, Jan 2006.

K. J. Shaw, D. A. Joyce, P. T. Docker, C. E. Dyer, G. M. Greenway, J. Greenman, and S. J. Haswell. Development of a real-world direct interface for integrated DNA extraction and amplification in a microfluidic device. *Lab Chip*, 11(3):443–8, Feb 2011.

S. E. Shokoples, M. Ndao, K. Kowalewska-Grochowska, and S. K. Yanow. Multiplexed real-time pcr assay for discrimination of plasmodium species with improved sensitivity for mixed infections. *Journal of clinical microbiology*, 47(4):975–80, Apr 2009.

V. J. Sieben. *Self-assembly on microfluidic platforms*. PhD thesis, University of Alberta, Feb 2009.

V. Sivagnanam, B. Song, C. Vandevyver, J.-C. G. Bünzli, and M. A. M. Gijs. Selective breast cancer cell capture, culture, and immunocytochemical analysis using self-assembled magnetic bead patterns in a microfluidic chip. *Langmuir : the ACS journal of surfaces and colloids*, 26(9):6091–6, May 2010.

K. Smistrup, O. Hansen, H. Bruus, and M. Hansen. Magnetic separation in microfluidic systems using microfabricated electromagnets—experiments and simulations. *J Magn Magn Mater*, 293(1):597–604, May 2005.

S. O. Sundberg, C. T. Wittwer, J. Greer, R. J. Pryor, O. Elenitoba-Johnson, and B. K. Gale. Solution-phase DNA mutation scanning and SNP genotyping by nanoliter melting analysis. *Biomed Microdevices*, 9(2):159–166, Jan 2007.

Y. H. Tennico and V. T. Remcho. In-line extraction employing functionalized magnetic particles for capillary and microchip electrophoresis. *Electrophoresis*, 31(15):2548–2557, Jul 2010.

S. van Pelt, R. Derks, M. Matteucci, M. F. Hansen, and A. Dietzel. Flow-orthogonal bead oscillation in a microfluidic chip with a magnetic anisotropic flux-guide array. *Biomed Microdevices*, 13(2):353–9, Apr 2011.

N. von Ahsen, M. Oellerich, V. W. Armstrong, and E. Schütz. Application of a thermodynamic nearest-neighbor model to estimate nucleic acid stability and optimize probe design: prediction of melting points of multiple mutations of apolipoprotein b-3500 and factor v with a hybridization probe genotyping assay on the lightcycler. *Clin Chem*, 45 (12):2094–101, Dec 1999.

P. S. Walsh, D. A. Metzger, and R. HIGUCHI. Chelex 100 as a medium for simple extraction of DNA for PCR-based typing from forensic material. *Biotechniques*, 10(4):506–13, Apr 1991.

C.-H. Wang, K.-Y. Lien, J.-J. Wu, and G.-B. Lee. A magnetic bead-based assay for the rapid detection of methicillin-resistant Staphylococcus aureus by using a microfluidic system with integrated loop-mediated isothermal amplification. *Lab Chip*, 11:1521–1531, Mar 2011.

J.-H. Wang, L.-J. Chien, T.-M. Hsieh, C.-H. Luo, W.-P. Chou, P.-H. Chen, P.-J. Chen, D.-S. Lee, and G.-B. Lee. A miniaturized quantitative polymerase chain reaction system for DNA amplification and detection. *Sensors and Actuators B: Chemical*, 141(1):329–337, 2009.

E. R. F. Welch, Y.-Y. Lin, A. Madison, and R. B. Fair. Picoliter DNA sequencing chemistry on an electrowetting-based digital microfluidic platform. *Biotechnol J*, 6(2):165–76, Feb 2011.

G. M. Whitesides. The origins and the future of microfluidics. *Nature*, 442(7101):368–373, July 2006.

J. Wilhelm and A. Pingoud. Real-time polymerase chain reaction. *Chembiochem*, 4:1120–1128, Jan 2003.

P. S. Williams, F. Carpino, and M. Zborowski. Theory for nanoparticle retention time in the helical channel of quadrupole magnetic field-flow fractionation. *J Magn Magn Mater*, 321 (10):1446–1451, May 2009.

M. Witek, S. Llopis, R. McCarley, and S. Soper. Purification of genomic DNA from whole cell lysates using photoactivated polycarbonate microfluidic devices. *Nucleic Acids Research*, 34(10):e74, Jan 2006.

C. Wittwer, G. Reed, C. Gundry, J. Vandersteen, and R. Pryor. High-resolution genotyping by amplicon melting analysis using lcgreen. *Clinical Chemistry*, 49(6):853–860, Jan 2003.

H.-W. Wu, R.-C. Hsu, C.-C. Lin, S.-M. Hwang, and G.-B. Lee. An integrated microfluidic system for isolation, counting, and sorting of hematopoietic stem cells. *Biomicrofluidics*, 4(2):024112, Jan 2010.

P. Yager, T. Edwards, E. Fu, K. Helton, K. Nelson, M. R. Tam, and B. H. Weigl. Microfluidic diagnostic technologies for global public health. *Nature*, 442(7101):412–418, 2006.

Y. Yamanishi, S. Sakuma, K. Onda, and F. Arai. Powerful actuation of magnetized microtools by focused magnetic field for particle sorting in a chip. *Biomed Microdevices*, 12(4): 745–52, Aug 2010.

S. Yeung and I. Hsing. Manipulation and extraction of genomic dna from cell lysate by functionalized magnetic particles for lab on a chip applications. *Biosensors and Bioelectronics*, 21(7):989–997, Jan 2006.

X. Yu, X. Feng, J. Hu, Z.-L. Zhang, and D.-W. Pang. Controlling the magnetic field distribution on the micrometer scale and generation of magnetic bead patterns for microfluidic applications. *Langmuir : the ACS journal of surfaces and colloids*, 27(8):5147–5156, Mar 2011.

C. Zhang, J. Xu, W. Ma, and W. Zheng. PCR microfluidic devices for DNA amplification. *Biotechnology advances*, 24:243–284, Jan 2006.

Y. Zhang, S. Park, S. Yang, and T.-H. Wang. An all-in-one microfluidic device for parallel DNA extraction and gene analysis. *Biomed Microdevices*, 12(6):1043–1049, Jan 2010.

H. Zipper, H. Brunner, J. Bernhagen, and F. Vitzthum. Investigations on DNA intercalation and surface binding by SYBR Green I, its structure determination and methodological implications. *Nucleic Acids Research*, 32(12):e103, Jan 2004.

Appendices

APPENDIX A

On-chip MCA and QPCR protocol and data analysis

This document provides procedures for QPCR and MCA runs on the TTK.

A.1 Preparing the TTK and chip

1. Place the PCRCE4 chip under a microscope and ensure all valve ports are neither stuck open nor closed by visual inspection (punch out PDMS if needed) and no holes are defects are present on the heater ring and contact pads. If valves appear closed, you may attempt to open them by blowing through the PCR input or output wells with the nitrogen gun. Chips that have sat longer than 2-3 weeks should always be inspected carefully, and any chips that have stuck valves cannot be used. Heater rings with defects must also not be used.
2. Open the AML GUI; enter in the general run details into the Information Panel (top left panel), and enter the MCA parameters into the MCA Panel.
3. Ensure air and vacuum are on, and connected to the TTK.
4. Wipe down the surface of the TTK gantry with ethanol and cleanroom wipes to get ride of any particles on the surface that may prevent proper chip-heatsink contact.
5. Place the chip on the stage, with the heater ring and chamber in the centre of the carved-out circle; adjust the chip holder as necessary. If the chamber is off center, it is more important for the heater ring to be centred relative to the heatsink.
6. Based on Jose's simulations, the chamber should be in the center of the heater and the heater should be in the center of the milled out region of the heat sink. For instance, a

chamber-heater misalignment of 400 μm would lead to a loss of 0.04°C in the chamber temperature (not very significant). However, a heater-heatsink misalignment of 400 μm would lead to a loss of 0.4°C in the chamber temperature (much more significant).

7. Clip the top into place, ensuring the pogo pins are in good contact without being fully depressed, and that the valve ports completely seal (no air is heard hissing from the stage). By rule of thumb, if the gantry merely rests over the chip without depressing the clips and no sound can be heard, the chip is in good alignment for the valves.

8. The pogo-pins are not designed to be fully depressed onto the heater and should not be fully screwed down onto the heater. The best method to ensure the pogo pins are in good contact is to screw them down until resistance is felt and then screw them half a turn up.

9. It is necessary to allow system's hardware and electronics to warm up to their run temperatures for at least 10 minutes prior to use to prevent inconsistent system behaviour during the run.

10. Open the lid on the system, and disconnect the banana clips from their jacks. Plug these banana clips into a well-charged, battery operated DMM (Fluke 179 or U1252a only, preferably U1252a). Measure the chip heater resistance, and enter this value and the DMM model being used into the GUI. Disconnect the banana clips from the DMM and re-connect them to the operating wires.

11. Zero the Wheatstone Bridge using the "Zero WB" button on the PCR Panel; adjust knob until the number is greater than 0 but less than 20; let it run for a bit to ensure the value is not drifting significantly. Press "Cancel" once this has been achieved.

12. Once these three things are done, enter in all the calibration data for the chip in the appropriate entry bars and press "Check Cal/DMM". This verifies the calibration data to the DMM data, and will determine if the resistances match within error.

13. If the chip does not match within error, you have three options:
    (a) begin again with a different chip (safest)
    (b) continue with the run, and request for the GUI to scale the slope with respect to the resistance offset
    (c) continue with the run, and tell the GUI to scale nothing (worst)

14. To begin again, return to step 4. To continue (no matter which choice), move on to loading the sample.

A.2 Loading the sample

1. Keeping the sample tube and pipette a safe distance from your person or behind a shield, carefully open the tube and pipette 4 μL of sample into the PCR input well of the chip. Do not fully depress all liquid out of the pipette tip as this both unsafe (aerosol generation) and can also leave a bubble of air on top of the well. Some of the mix may bleed into the SP portion of the PCRCE4 chip, but this will not affect your loading.

2. Go to the Valve/Pump tab on the GUI and click the "Suck In" button. This will check off three valves, and give three valve numbers into the pumping area. Click "Set Valves" to open the three checked valves. You must listen to ensure you hear the click of the relays. If you do not, you will need to power off and power on your system.

3. Pump for 3 cycles at 500 ms intervals, using the "Pump" button. Watch while pumping to ensure the chamber fills and the mix just reaches the PCR output well. If the mix does not reach, pump for an extra cycle or two as necessary for the mix to reach this well, and make sure to note this in the PCR run notes.

4. Choose the "Close All" button, and press "Set Valves". Remove any excess liquid from the PCR input well, and discard along with the pipette tip into a bio-safety bag.

5. Pipette 5 μL of autoclaved water into the sample well and depress and release the stopper without fully depressing the liquid into the well. This will wash the well of the PCR mix. Dispose of that tip and using a new tip, remove any excess liquid from the well. This is to prevent the any ions within the sample from sticking to the walls of the well and changing the concentration of ions in your flush-out buffer.

A.3 Checking the LED

1. Click "Toggle LED" on the MCA tab or type "TL (1)" into the terminal window to turn on the LED. Check that the LED light is on and is focused on the top layer of the chip. Ensure your eyes are level with the gantry.

2. The PCR chamber is on the top glass layer of PCR/CE-4 chips. As a result, one needs to make sure that LED light fully enters the top layer of chip as shown in the figure below. If the LED is not properly coupled into the top glass layer, adjust the dial on the brass LED holder using a screwdriver. It works like a seesaw, turning the screw downwards will raise the LED vertically, while turning the screw upwards will lower the LED.

3. After ensuring proper LED light coupling, click "Toggle LED" or type "TL (0)" into the terminal to turn off the LED.

4. Check to ensure all valves are closed and all parameters are entered into the GUI.

5. Close the lid on the TTK gantry and cover the TTK with the designated cardboard box (labelled “Angelina”). The cardboard box is necessary to completely seal the system off from background light.
6. Allow up to 5 minutes for the system’s temperature to stabilize (as a result of the cardboard cover). Select which thermocouples are connected to the system. (A thermocouple must be connected from TC1 to the heat sink). Click the “Get Temp” button. This will retrieve the heatsink temperature and add 0.5°C to it to account for the increased temperature in the system between idle and operational states.

A.4 Setup camera GUI

1. Open the “Autostar Envisage” program on the “TTK2 macbook” laptop.
2. In the top-left section of the GUI window, enter Exposure time = 0.7s. Press enter after entering the value otherwise it will not be stored in the GUI even though it shows up in the text box.
3. In the mid-left section of the window, set the Histogram sliders such that the black slider is set to 4500, and the white slider is set to 7000. Press enter after entering each value.
4. In the top-right section of the window, enter a descriptive name in the “Object name” textbox e.g. “MCA1-b2m-”. Press Enter. This name will appear on all the images during this MCA run.
5. In the top-mid section of the window, enter “1” in both the “minimum quality” and “evaluation count” windows. Press enter after entering each value.
6. Click on the “Settings” menu item, and click on the “Browse” button next to “Image directory” on the right hand side of the settings window. Select your work folder where images gathered will be saved. Make sure you remember and can easily access this folder as it will hold your experimental data.
7. Close the settings window but leave the main camera GUI window open as you will observe it during the MCA run.

A.5 Start MCA run

1. Go back to the MCA tab of the TTK GUI and Click “Run MCA”.
2. If your calibration data did not pass the verification step, you will now be prompted to continue with the entered calibration data or to modify the slope assuming the TCR of the chip has not changed. Choose the option you would prefer, and click OK.

3. Go to the camera GUI and click “Start” on the top right hand side of the window. Do this at most 20s after clicking “Run MCA” to ensure that you do not miss any MCA data. This is because the first 20s of the MCA run is warm up time during which the LED is not on – but afterwards, the LED is on and MCA data is being gathered.

4. Observe the main window of the camera GUI; you should see a bright image in the chamber at the start of the run. However, as the MCA run progresses the chamber should darken as the DNA is melted (see the image below for an illustration).

5. Wait for the MCA run to finish and when the TTK GUI signals Run complete, click stop on the camera GUI.

APPENDIX B

Total time for SP-PCR-MCA experiments

Table B.1: Run time for each step in on-chip SP-PCR-MCA reaction

Procedure	Duration	Notes
Obtaining clinical sample	30 min	15 min cell lysis, 10 min Proteinase K denaturation.
DNA extraction (SP)	2 min	1.7 min magnet motion, 0.3 min initialization
Polymerase Chain Reaction (PCR)	65 min	2 min pre-denaturation, 35 cycles of 0.5 min denaturation, 0.5 min annealing, 0.5 min extension, 2 min post-extension. Previous work showed that we can complete this step in 40 mins with protocol and system adaptations [a]
Melting Curve Analysis (MCA)	10 min	10 minute at 0.05°C/s ramp rate for excellent sensitivity
Total time	**107 min**	

---

[a] Hoang VN, Kaigala GV, Atrazhev A, Pilarski LM, Backhouse CJ, (2008) Strategies for enhancing the speed and integration of microchip genetic amplification. Electrophoresis, 29:4684–4694

APPENDIX C

Total system cost

Table C.1: This component cost (USD currency) listed here is of the instrument based on low volume ordering. We believe this cost will be significantly reduced with high volume purchase

Component	**Quantity**	**Cost**
Emission filter (D480/40m; Chroma Technology Corp., Bellow Falls, VT, USA)	1	$150
Excitation filter (D425/60x; Chroma Technology Corp., Bellow Falls, VT, USA)	1	$150
Luxeon III Star LED - Royal Blue Lambertian LED (LXHL-LR3C,Quadica developments Inc., Ontario, Canada)	1	$7
CCD camera (Meade deep sky imager pro monochrome; Meade Instruments Corporation, Irvine, CA, USA)	1	$299
Pneumatic valves (LHDA1233115H; The Lee, Company, Westbrook)	4	$140
Other electronics (ADC, DAC, Op-amps, regulators, other discrete components and PCBs)	-	$250
Stepper motor (Danaher Motion, 26DBM10D2U-L)	2	$125
Motor controller chip (STMicroelectronics L297)	2	$10
Motor driver (STMicroelectronics ULN2803A)	1	$1
Photo logic slotted optical sensors (Optek Technology OPB930W)	2	$15
Atmel Atmega32 AVR microcontroller	1	$5
	Total cost	~$1152